Experimentele analyse van roterende demping in hogesnelheidsmachines

Experimental Analysis of Rotating Damping in High Speed Machinery

Bram Vervisch

Promotoren: prof. dr. ir. M. Loccufier, prof. dr. ing. K. Stockman
Proefschrift ingediend tot het behalen van de graad van
Doctor in de ingenieurswetenschappen: werktuigkunde-elektrotechniek

Vakgroep Elektrische Energie, Systemen en Automatisering
Voorzitter: prof. dr. ir. J. Melkebeek
Faculteit Ingenieurswetenschappen en Architectuur
Academiejaar 2015 - 2016

UNIVERSITEIT
GENT

ISBN 978-90-8578-926-0
NUR 978
Wettelijk depot: D/2016/10.500/58

Universiteit Gent
Faculteit Ingenieurswetenschappen en Architectuur
Vakgroep Elektrische energie, Systemen en Automatisering

Promotoren:

Prof. dr. Ir. Mia Loccufier	(Universiteit Gent - EA08)
Prof. dr. Ing. Kurt Stockman	(Universiteit Gent - EA08)

Lees-en examencommissie:

Prof. dr. ir. Gert de Cooman	(Universiteit Gent - chairman)
Prof. dr. ir. Eric Chatelet	(INSA Lyon - France)
Prof. dr. ir. Patrick Guillaume	(Vrije Universiteit Brussel)
Prof. dr. ir. Alain Sarlette	(Universiteit Gent - EA06)
Prof. dr. Michael Monte	(Universiteit Gent - EA08)
Prof. dr. ir. Patrick De Baets	(Universiteit Gent - EA08)
Prof. dr. ir. Joris Degrieck	(Universiteit Gent - EA10)

Universiteit Gent
Faculteit Ingenieurswetenschappen en Architectuur

Vakgroep Elektrische energie, Systemen en Automatisering
Campus Kortrijk
Graaf Karel de Goedelaan 5, B-8500 Kortrijk, België

Tel.: +32 56 24 12 21

Proefschrift tot het behalen van de graad van
Doctor in de Ingenieurswetenschappen:
werktuigkunde-elektrotechniek
Academiejaar 2015-2016

Preface

Innovation is a human trait. It is one of the main differences between a human being and other species. Unlike many human traits, innovation is not the result of a single person's effort but of a vast network of people that combine their curiosity, creativity and persistence into stupendous results. As we are these people, we rely on thorough work of our colleagues and ancestors. Innovation only continues by adding small pieces of information into a massive stack. Solely a society that opens up for innovation and keeps inspiring people to make these small efforts will be able to sustain. Nowadays, the internet is an abundant source of information and communication which makes these times enormously interesting for researchers.

For this reason I started a PhD, six years ago. I've been blessed with curiosity since I was a child. I just needed to enhance my creativity and practise persistence. University gave me eduction and time to adopt these virtues gradually. Therefore, my first and most important acknowledgement goes to society. The society in which I grew up provided the framework for innovation. Low cost education, free libraries and research financed by the government are only a few examples of incentives that nourish innovation.

My second acknowledgement goes to my parents, who gave me a carefree youth and dedicated their life to the well-being of me and my siblings. Being the youngest of four I always had to catch up with my sister and brothers. This made me strong and resilient. Technology was definitely in our blood and was many times a subject for discussion.

Nonetheless, although tempting to keep on diverging, research is also about converging into relevant results. Especially in the broad area of rotordynamics, which was entirely new for me, I needed guidance. It was my promoter, prof. Kurt Stockman who initiated me in research. He provided a network of people, finances without much questions and room for failure as much as room for success.

My second promotor, prof. Mia Loccufier, introduced me into the abstract, yet very practical, world of systems. She guided me through the matrices, eigenvalues and eigenvectors with much patience. I very much enjoyed the discussions which got more interesting year after year. As much as my theoretical guide, she was also my mental guide and therefore I'm very grateful.

I would'nt have survived these six years if it wasn't for my colleagues. I definitely would like to thank my fellow-sufferers Stijn and Colin with whom I discussed about much more than PhDs alone. Also, the 'islanders' in Kortrijk played an important role: mr. Mechatronics Bart, music-master Simon, my travelling companion Michael and youngsters Florian, Michiel and Jasper who even were my students in the beginning. The 'energy efficiency team': Steve, Pieter, Elewijn and Heinz gave me a head-start in research. Furthermore, EMC-Bram and MCSA-Bram (loud discussions!), made my life easier. Bruno, 'the godfather of vibrations in Kortrijk' was a great mentor. Also my collegues in Gent: Frits, Raiko and the two Kevins were a great support.

Last but not least I want to thank my wife Silke and my sons Otto and Tijl both born during my PhD. I especially want to thank Silke for enduring me, supporting me, and learning me so much more then I ever could learn at any University. She taught me, and is still teaching me to put things in perspective, to enjoy life and get back up when I'm down. Otto and Tijl, little men, some day you will understand what daddy was doing all day behind his laptop. Whatever you do in the future, do not take anything for granted and contribute to society.

Ieper, april 2016
Bram Vervisch

Table of Contents

List of Figures

List of Tables

Nederlandse samenvatting

Machines die roteren aan een hoge snelheid, waarvan de aandrijfsnelheid hoger is dan de eerste kritische snelheid of de eerste resonantiefrequentie, zijn gevoelig aan instabiliteit. Hoewel instabiliteit of een zelf aanlopende trilling niet altijd worden vastgesteld als de hoofdoorzaak voor vroegtijdig falen, ligt dit fenomeen vaak aan de basis. Roterende demping, of inwendige rotor demping is één van de aanleidingen voor instabiliteit. Dit type demping is relatief ten opzichte van een roterend assenstelsel en is bijgevolg afhankelijk van de aandrijfsnelheid. De stabiliteitsgrens of de snelheid waarbij instabiliteit voorkomt hangt af van de verhouding tussen roterende demping en de niet-roterende demping. De roterende demping is de demping in de roterende onderdelen en de niet-roterende demping is voornamelijk de demping in de lagers. Dit onderzoek draagt bij aan drie onderdelen in de analyse van roterende machines: de eindige elementen analyse, experimentele identificatie van demping en de focus op industriële toepassingen.

Modelleren en identificeren van roterende demping in industriële toepassingen vereist een diepgaande kennis van het fysische gedrag van roterende demping. Instabiliteit is een fenomeen dat voorkomt bij vrije trillingen. Dit betekent dat er geen externe kracht aanwezig hoeft te zijn, enkel een storing. De roterende demping is afhankelijk van de aandrijfsnelheid en het specifieke gedrag wordt hoofdzakelijk veroorzaakt door het verschil tussen de spin en de werveling. Spin is de beweging veroorzaakt door de aandrijfsnelheid. Werveling is een circulaire beweging die overeenkomt met een kritische snelheid. Het effect van negatieve demping, dat instabiliteit teweegt brengt, wordt veroorzaak door het verband tussen spanning en rek in het materiaal van de as. Hierdoor ontstaat er een volgkracht boven de stabiliteitsgrens. In dit onderzoek wordt bestaande literatuur samengebracht om een duidelijk inzicht te krijgen in het ontstaan van deze volgkracht en de instabiliteit die hieraan gekoppeld wordt.

Door het begrijpen van roterende demping kan hieruit een lineair snelheidsafhankelijk model afgeleid worden. Hiervoor worden de Lagrange vergelijkingen gebruikt samen met een gedistribueerde eindige element methode. Er wordt gestart met het definiëren van kinetische, potentiële en dissipatie energie in het roterend systeem. Omwille van de rotatie, is er een inertiaalstelsel en een roterend coördinatenstelsel. Het roterende stelsel wordt afgeleid met Euler hoeken en een translatie in x, y en z. Deze transformatie veroorzaakt enkele abnormaliteiten in het model. Hiermee wordt voornamelijk het gyroscopisch effect en de roterende

demping bedoeld. Beide effecten resulteren in asymmetrische matrices. Om op basis hiervan modale analyse te gebruiken moeten zowel linkse als rechtse eigenvectoren gedefinieerd worden.

Experimentele validatie is een uiterst belangrijke doelstelling in dit onderzoek. Vandaar dat er twee experimentele opstellingen worden voorgesteld: de roterende demping opstelling en de torsieproefstand. De roterende demping opstelling is een experimenteel equivalent van een roterende dubbelzijdig ingeklemde as. Deze is speciaal ontworpen om roterende demping te onderscheiden van alle andere effecten zoals het gyroscopisch effect, onbalans en andere externe krachten. Om het systeem te exciteren wordt er een nieuw concept geïntroduceerd, namelijk een automatische impacthamer. Hiermee kan er een reproduceerbare kracht op de opstelling uitgeoefend worden onder veilige omstandigheden. De responsies worden opgemeten met nabijheidssensoren, een vaak gebruikte techniek in de rotordynamica. Enkele specifieke keuzes worden gemaakt om de fouten te minimaliseren.

De tweede opstelling is een torsieproefstand. Deze opstelling wordt gebruikt als een referentie voor een systeem met meerdere vrijheidsgraden. Het is een torsiesysteem met vier vrijheidsgraden en is speciaal ontworpen om eenvoudig gemodelleerd en gemeten te worden. Het theoretische model wordt gemaakt met discrete parameters en de demping is proportioneel met de stijfheidsmatrix. Extra demping wordt toegevoegd door middel van wrijving. De torsieproefstand wordt gebruikt om de voorgestelde dempingsmatrix identificatiemethodes te valideren.

Een belangrijke bijdrage van dit onderzoek is de beschrijving van het modaal model. De term modaal model wordt algemeen gebruikt en beschrijft het gedrag van een systeem in één mode. Doorgaans wordt, in de rotordynamica, de Jeffcott rotor gebruikt om dit gedrag te beschrijven. De Jeffcott rotor is echter een theoretisch concept waarbij de link met experimenten ontbreekt. Het modaal model dat gebruikt wordt in dit onderzoek wordt afgeleid van het algemene systeem met meerdere vrijheidsgraden. Hierin worden zowel het gyroscopisch effect als de roterende demping meegerekend. Het resulterende model bevat complexe parameters, maar door middel van perturbatie analyse, met de veronderstelling van lichte demping, kan dit vereenvoudigd worden in een combinatie van zuiver reële en zuiver imaginaire parameters. Deze vereenvoudiging resulteert in een uitdrukking voor het verval en de stabiliteitsgrens. De veronderstellingen worden gevalideerd op de proefopstelling.

Het nieuwe afgeleide model kan gebruikt worden voor de experimentele voorspelling van de stabiliteitsgrens. Er moet echter nog rekening gehouden worden met de imaginaire parameters in het modaal model. Daarenboven moet de opstelling gecontroleerd worden op lichte demping. Er wordt een procedure voorgesteld om deze lichte demping na te gaan met een minimum aantal metingen. De imaginaire parameters komen overeen met het gyroscopisch effect en de roterende demping. Door de energie te bestuderen die samen gaat met deze twee termen, wordt

een equivalent vervalmodel voorgesteld. Dit model is eenvoudig te gebruiken in experimenten en maakt het mogelijk om een procedure op te stellen waarin de stabiliteitsgrens voorspeld wordt. Deze procedure wordt gevalideerd op de roterende demping opstelling. Er wordt aangetoond dat de stabiliteitsgrens nauwkeurig kan voorspeld worden en dat er effectief instabiliteit optreedt boven deze grens.

De experimentele voorspelling van de stabiliteitsgrens is een belangrijke bijdrage maar voorziet geen manier om meer inzicht te krijgen in het dempingsmodel. Daarom worden dempingmatrix identificatiemethodes voorgesteld. In de literatuur zijn er twee groepen identificatiemethodes: modale methodes en matrix methodes. Om de matrix methodes te kunnen uitvoeren is er nood aan de volledige frequentieresponsiefunctie matrix. Dit betekent dat elk punt gemeten en geëxciteerd moet worden. Omwille van het tijdrovende karakter en het feit dat het niet altijd mogelijk is om alle gewenste meetlocaties te bereiken wordt er gekozen voor modale methodes. De modale methodes zijn gebaseerd op polen en eigenvectoren en hebben daarom enkel een rij of een kolom nodig van de frequentieresponsiefunctie matrix.

Twee van deze methodes worden voorgesteld: Lancasters methode en Adhikari's methode. In dit onderzoek wordt Lancasters methode uitgebreid met linker er rechter eigenvectoren. In combinatie met het equivalent vervalmodel dat afgeleid is uit het modaal model, wordt er een equivalent vervalmodel voor roterende systemen met meerdere vrijheidsgraden voorgesteld. Op dit systeem kan Adhikari's methode, die ontworpen is voor niet-roterende systemen, gebruikt worden. Een gesimuleerd voorbeeld wordt voorzien als validatie. In de praktijk hebben geïdentificeerde eigenvectoren vaak veel afwijkingen. De modale methoden hebben het nadeel dat ze heel gevoelig zijn aan deze afwijkingen. Daarom worden er drie optimalisatieprocedures voorgesteld. Voor iedere procedure worden de voor- en nadelen besproken.

Uiteindelijk worden de torsieproefstand en de roterende demping opstelling gebruikt om de dempingsmatrix identificatiemethodes en de optimalisatietechnieken te valideren. Omdat het model achter de torsieproefstand heel realistische resultaten oplevert worden hierop gedwongen responsies gesimuleerd. Deze simulaties hebben het voordeel om vrij te zijn van ruis en laten toe om een zuivere validatie uit te voeren op de identificatie- en optimalisatiemethodes. Het blijkt dat, in simulatie, de dempingsmatrices eenvoudig gereconstrueerd kunnen worden. In een werkelijke meting is er altijd ruis. De dempingsmatrices die uit de meting voortkomen zijn niet volledig fysisch relevant, maar zijn zeker in staat om de extra toegevoegde demping terug te vinden. In de roterende demping opstelling is er meer ruis. Bovendien is het aantal meetpunten gelimiteerd. Door deze te linken met de polen kan de fysische relevantie aangetoond worden.

Samengevat verschaft dit onderzoek praktisch inzicht in roterende demping en het effect op de stabiliteitsgrens. Een nieuw modaal model brengt theorie en ex-

periment dichter bij elkaar en een experimentele procedure om de stabiliteitsgrens te voorspellen wordt voorgesteld. Bovendien worden er dempingsmatrix identificatiemethodes besproken en uitgebreid naar roterende systemen. Een torsieproefstand en een roterende demping opstelling worden voorgesteld en gebruikt om de voorgestelde methodes te valideren.

English summary

High speed rotating machinery, with an operating speed above the first critical speed or the first resonance frequency, is sensitive to instability. Although instability or self-excited vibration may not always be diagnosed as the main cause for breakdown or failure, it is a root cause in many cases. Rotating damping, or rotor internal damping is one of the main sources of instability. This type of damping is relative towards the rotating frame and is therefore dependent on the operating speed. The stability threshold speed, at which instability occurs, depends on the ratio between rotating damping, or the damping in the rotating parts, and nonrotating damping, mainly the damping in the bearings. This research contributes in three main parts of the analysis of rotating machinery: the finite element analysis, experimental damping identification and the focus on industrial applications.

Modelling and identification of rotating damping in industrial applications requires thorough understanding of the physical behaviour of rotating damping. Instability is a free vibration phenomenon. This means that there is no need of an external force, only a disturbance. The rotating damping depends upon the operating speed and its specific behaviour is mainly caused by the difference between spin and whirl. Spin is the motion caused by the operating speed. Whirl is a circular motion corresponding to a critical speed. The negative damping effect, that causes instability, occurs because of the stress-strain relation in the shaft material which causes a follower force above the stability threshold speed. In this research, existing literature is combined in order to get a clear insight into the origin of the follower force and the corresponding instability.

The understanding of rotating damping can be used to derive a linear speed dependent model. This is performed with the Langrange equations combined with distributed finite element technique. It starts with the definition of kinetic, potential and dissipation energy in the rotating system. Because of the rotation, there is an inertial frame, and a rotating frame. The rotating frame is defined through Euler angles and a translation in x, y and z. This transformation causes some anomalies into the model, mainly the speed dependent gyroscopic effect and the rotating damping. Both effects result in asymmetric matrices. In order to use modal analysis both left and right eigenvectors have to be defined.

Experimental validation is of paramount importance in this research. Therefore, two practical setups are used: the rotating damping setup and a torsional

vibration setup. The rotating damping setup is an experimental equivalent of a rotating clamped beam. It is designed especially, through well-considered design choices, to separate the rotating damping effect from all other effects such as, gyroscopic effect, unbalance and other external forces. As an excitation, a new concept, namely an automated impact hammer, is designed in order to create a force that is easily implemented upon a rotating shaft but is still repeatable and safely operated. The responses are measured through eddy current probes, widely used in rotordynamics. Some specific choices are made towards the minimization of errors.

The second setup is a torsional vibration setup. This setup is used as a reference for multiple degree of freedom models. It is a four degree of freedom torsional system and is especially designed to be modelled and measured easily. The theoretical model is constructed with lumped parameters and the damping is chosen to be proportional to the stiffness matrix. An extra damping is added on the third disk by friction. The torsional vibration setup is used to validate the damping matrix identification methods.

A major contribution of this research is the description of the modal model. The term modal model is widely used and describes the behaviour of a system in a single mode. Generally, in rotordynamics, the principle of the Jeffcott rotor is used to explain this behaviour. However, the Jeffcott rotor is a theoretical principle and lacks a link towards experimentation. The modal model, used in in this research, is derived from the general multiple degree of freedom model with gyroscopic effect and rotating damping. The resulting model contains complex parameters but through perturbation analysis, with the assumption of light damping, this can be simplified in a combination of purely real and purely imaginary parameters. This simplification leads to a straightforward expression of the decay rate and the stability threshold speed. The assumptions are validated with an example of the test setup.

The newly derived modal model can be used for an experimental prediction of the stability threshold speed. However, there is still a hurdle, the appearance of the imaginary parameters in the modal model. Moreover, the device under test needs to be checked for light damping. A procedure to validate this light damping with a minimum of measurements is proposed. The imaginary parameters correspond to both the gyroscopic effect and the rotating damping. By taking a closer look at the energy that correlates to these effects an equivalent decay rate model is proposed. This model is experimentally friendly and paves the way for a measurement procedure that predicts the stability threshold speed. A validation on the rotating damping setup demonstrates that the procedure is able to predict the stability threshold speed accurately and instability occurs above this speed.

The experimental prediction of the stability threshold speed is an important contribution but it does not provide an expedient way of getting insight into the damping model. Therefore, damping matrix identification procedures are pro-

posed. In literature, there are two groups of identification methods: modal methods and matrix methods. The latter needs the measurement of the entire frequency response function matrix. This means that every point has to be measured and excited. Due to the time-consuming character and the fact that it is not always possible in industrial applications to access all measurement locations, modal methods are used. The modal methods are based upon poles and eigenvectors and therefore only need one row or column of the frequency response function matrix. Two of these methods are presented: Lancaster's method and Adhikari's method. Within this research, Lancaster's method is extended towards left and right eigenvectors. In combination with the equivalent decay rate model which is derived from the modal model, an equivalent decay rate model for multiple degree of freedom rotating systems is proposed. On this system, Adhikari's method, which is designed for nonrotating systems, can be used. A simulated example is provided as a validation. In practise, the identified eigenvectors are erroneous. The modal methods have a severe disadvantage because they are sensitive to these errors. Therefore, three optimization techniques are presented. For each procedure, the advantages and disadvantages are discussed.

Finally, the torsional vibration setup and the rotating damping setup are used to validate the damping estimation methods and the optimization techniques. Because the model behind the torsional vibration setup yields very realistic results, first, forced responses are simulated. These simulations have the advantage to be free of noise and allow a clear validation of the identification and optimization techniques. It is seen that, in simulation, the damping matrices are easily reconstructed. In an actual measurement, there is extra noise. The damping matrices are not entirely physically relevant but can definitely be used to find the extra added damping. In the rotating damping setup, there is more noise. Moreover, the number of measurement points is limited. By linking the results to the poles, the physical relevance is demonstrated.

To summarize, this research provides practical insight into rotating damping and its effect on the stability threshold speed. A newly derived modal model closes the gap between theory and experiment and an experimental procedure to predict the stability threshold speed is proposed. Moreover, damping identification methods and optimization techniques, are discussed and extended towards rotating systems. A torsional vibration setup and a rotating damping setup are presented and used to validate the proposed procedures.

List of Sybmols

Symbol	Units	Description
c	Ns/m	damping
c_r	depends	rotating damping
d	m	diameter
e	$-$	Euler's number
$\mathbf{f}$	N	force vector
f	N	force
f_r	N	restoring force
g	Ns/m	gyroscopic effect
h	m	impulse response
i	$-$	complex operator
k	N/m	stiffness
m	kg	mass
p	N	nonconservative force
$\mathbf{q}$	depends	generalized displacement
s	$-$	Laplace operator
t	s	time
u	m	translation
w	J	work
x	m	displacement in x-direction
y	m	displacement in y-direction
z	m	displacement in z-direction
A	m^2	area of cross section
$\mathbf{A}, \mathbf{B}$	$-$	state space matrices
B_r	Hz	bandwidth at resonance
$\mathbf{C}$	Ns/m	damping matrix
$\mathbf{C}_n$	Ns/m	non-rotating damping matrix
$\mathbf{C}_r$	depends	rotating damping matrix
D	J	dissipation energy
E	Pa	Young modulus
E_d	J	dissipated energy
E_{cyc}	J	cyclic energy
F_0	N	maximum force
G	Pa	shear modulus
$\hat{G}_{yx}$	depends	cross-spectral density

$\hat{G}_{xx}$	depends	auto-spectral density
$\mathbf{G}$	Ns/m	gyroscopic matrix
H	m/N	frequency response function
$\mathbf{H}$	m/N	frequency response function matrix
I	m^4	area moment of inertia
$\mathbf{I}$	$-$	identity matrix
J	kgm^2	mass moment of inertia
$\mathbf{K}$	N/m	stiffness matrix
L	m	length
$\mathbf{M}$	kg	mass matrix
N	$-$	deflection function
Q	N	sum of generalized forces
$\mathbf{R}$	$-$	tranformation matrix
T	J	kinetic energy
$\mathbf{T}$	Nm	vector of external torque
V	J	potential energy
X_0	m	maximum displacement
ϵ	m	strain
ζ	$-$	damping coefficient
θ	rad/s	cyclic pulsation
$\boldsymbol{\theta}$	rad	vector of angular displacements
λ	$-$	eigenvalue
μ	kg/m	mass per unith length
σ	Pa	stress
σ_i	$-$	decay rate for mode i
ρ	$\mathrm{kg/m}^3$	mass density
$\boldsymbol{\phi}$	$-$	left eigenvector
$\boldsymbol{\psi}$	$-$	right eigenvector
ω	rad/s	rotor spin
ω_n	rad/s	natural pulsation
Θ	rad	rotation
Λ	$-$	matrix of eigenvalues
$\mathbf{\Phi}$	$-$	matrix of left eigenvectors
$\mathbf{\Psi}$	$-$	matrix of right eigenvector
Ω	rad/s	whirl

1 Introduction

1.1 Problem statement

The study of rotating machinery is an important discipline in engineering. It involves a wide variety of industrial applications going from power generation to manufacturing and even home appliances. The sizes of the machinery extend from very small, precise drills to giant turbines used for power generation. The range of speeds goes from nearly standstill to more than hundred thousands rpm. As stated in the Proceedings of the IUTAM Symposium on Emerging Trends in Rotor Dynamics in 2009, the future research has to be directed towards development of intelligent/smart rotor systems which will be extremely robust and ultra-reliable [4]. Increasing reliability is accomplished through proactive maintenance, a strategy that is based upon root cause analysis. It is important to know that the root cause of failure is not always diagnosed as the main source of problems. Often, the root cause triggers other mechanisms that eventually initiate a breakdown or standstill. Forsthoffer claims, from own experience, that approximately 80% of machinery failure root causes are due to process variations that are not anticipated in the design phase [5].

Rotor internal damping or rotating damping is a property of rotating machinery that can yield self-excited vibrations or instabilities. It is not often diagnosed as the main cause for breakdown or failure, but the destabilizing mechanism may be a significant contributing factor in cases where other instabilities such as oil whip or steam whirl are diagnosed as the primary source of self-excited vibration [1].

The destabilizing mechanism of rotating damping is known for almost a century, but research on the modeling and the identification is still ongoing. Chiefly, the main obstacle is the dependency of the physical behaviour of the rotor to the operating speed. This is the reason why modeling and identifying such systems is not straightforward. A detailed understanding of the physical behaviour of the rotor at different operating speeds is of paramount importance. This research focusses on the modeling and the damping identification with respect to rotating damping and with a special focus on stability. Moreover, direct implementation of the proposed methods in industrial applications is an important requirement. Three important topics are highlighted: Finite element analysis as the main modeling principle, damping identification and the focus on industrial applications.

FEM Nowadays, finite element models are not only predominant in rotordynamics but in nearly all disciplines of applied engineering. The combination of computer aided design software with finite element solvers creates a user-friendly environment for different kinds of analysis. With the ever increasing computing capacity of current workstations, the power of these software packages is still enhancing. For finite elements, this briefly means that the number of elements is becoming less important, leading to increased accuracy. In rotordynamics, finite element models are very effective in predicting critical speeds, steady state analysis and visualization of the results. Stability analysis, or the prediction of the operating speed at which the rotor becomes unstable, is more complicated. This is mainly because the accuracy of the finite element method is not only defined by the computing capacity but even more by the quality of the underlying model. For systems with a linear behaviour, the modelling of mass and stiffness, generally derived from kinetic and potential energy, is straightforward. On the contrary, damping, derived from the dissipation energy, is more complicated.The stability threshold speed is highly sensitive to the damping model [6]. Experimental validation and model updating are possibilities to optimize the model, but this involves accurate measurement techniques usually based upon experimental modal analysis. Although the general rotordynamic models are available [7], experimentation is challenging. Not only because the system is rotating, but also due to the asymmetry in the matrices of the presumed model. Moreover, because the stability threshold is highly determined by the damping, techniques that allow accurate damping measurement are needed. It is an objective of this research to clarify the physical meaning of the damping mechanism behind rotating damping and to define a clear link with the finite element model.

Damping identification Accurate damping identification can be interpreted differently, depending on the application. When, for instance, the prediction of

the stability threshold speed is of interest, the focus is on the destabilizing pole. An accurate estimation of the poles is needed. When the interest is the mechanism behind the instability, the focus is rather the damping type, for instance, viscous or nonviscous damping. If the optimal locations to add or even remove damping are the primary purpose, the physical location and magnitude of the damping is needed. A good measurement procedure provides accurate results which preferably combine some of the different purposes. Although many different damping models are available [8], there is still a lack of a general damping model. It is however not the purpose of this research to find a general damping model, but to define procedures that are rather independent of the presumed model. Damping as a destabilizing mechanism in rotordynamics is a problem that is preferably studied through the pole location. Accurate estimation of the speed dependent poles is therefore an important part of this research. A more detailed approach is damping matrix identification. An estimation of the damping matrix has several advantages. It gives insight on the amount of damping, the damping location and sometimes even the damping mechanism. An identified damping matrix can also be used to predict the poles at several operating speeds or the steady state behaviour. A second important part in this thesis is consequently damping matrix identification.

Industrial applications In an industrial environment, straightforward and user-friendly methods are needed. As for the proposed methods, the applicability in industry depends upon these considerations. This particularly means that the number of measurements and the measurement time has to be low. Expensive sensors and actuators need to be avoided but still, accuracy is predominant. Accuracy and applicability are often contradictory. However, in this research, industrial application is the main priority. Well considered simplifications are made in the models and the measurement procedures are confined to the essentials.

1.2 The history of rotating damping instability

The research on the stability in rotating machinery has always been driven by industrial interest. An increasing operating speed results in an increased performance for lower dimensions. Lower dimensions generally lead to higher flexibility of the components and therefore vibrations are more likely to occur. The growing demand for higher operating speeds is what motivates the industry to optimize the design of rotors. Through the years, more advanced modelling and experimental technologies have facilitated engineers to breach through existing boundaries and push to the limits of physical possibilities. This rush for higher operating speeds

already started during the second industrial revolution (1840-1914) under the particular impulse of steam turbine manufacturers. The first problem that was encountered in these rotating machines was the *critical speed*. A speed at which, due to an excitation by unbalance, high vibration amplitudes occur. This critical speed corresponds to the first natural frequency of the rotor. The problem was discovered by William Rankine in 1869 [9]. Rankine concluded that it was impossible to rotate above the critical speed and proposed a design philosophy that limited operating speeds. In 1895, the Swedish engineer Gustaf De Laval showed experimentally that it was possible to cross the first critical speed (as stated by Adams in [1]). However, these supercritical speeds gave rise to new observations. By operating machines supercritically, manufacturers became aware of severe vibrations that were independent of the operating speed and unbalance but sometimes needed to be triggered by a small disturbance. General Electric engineers Newkirk and Kimball pioneered in the understanding of these unwanted vibrations. Newkirk [10] described a problem that occurred in blast furnace compressors and Kimball [11] created a theoretical framework based upon *internal friction in the rotor* that explains these supercritical vibrations. Not only observations but also experimental studies were described in these early publications together with some important physical insights. The description of these vibrations clearly correspond to unstable behaviour. The physical phenomenon of *rotating damping*, or the damping in the rotating parts of the rotor, was established as a potential source of instabilities. Smith [12] and Robertson [13] added important early contributions, but from then on, rotating damping lost its importance. This shift in interest was mainly caused by another, in those days more important source of instability: hydrodynamic bearings. Newkirk and Taylor conducted experiments on a rotor with minimal internal friction and showed that the instabilities where caused by the forces in the oil film of the bearings [14]. These instabilities are now widely known as oil whirl and whip [15]. In the 60s, the work of Newkirk and Kimball on rotating damping was picked up again, mainly under the influence of the aerospace industry, by Ehrich [16] and Gunter [17]. The focus lies upon the stability threshold speed that appears to be governed by the ratio between external and internal friction. Also in the 1960s, the *finite element method* was developed. The finite element method is a discretization technique designed to solve partial differential equations numerically. This allows engineers to predict the dynamic behaviour of complex mechanical structures. In 1977, Zorzi and Nelson [18] introduced rotating damping into a finite element formulation. The stability problems in Space Shuttle Main Engines [19] were a direct cause for a boost in the research efforts on rotating damping. In the 80s and early 90s Lund [20] and Walton [21] discussed the effect of micro-slip in internal joints as a major cause of rotating damping. In the last decennia, finite element models have been prominent in the modeling of rotating damping. More recent work is done by Forrai [22] [23] where it is

shown that within this mathematical formulation, it is impossible to rotate above the *stability threshold speed*, or the speed at which instability occurs. The research on rotating damping and the influence on the stability is still continuing. In 2004, Kandil provided an overview of theoretical background and experimental techniques to validate rotor internal damping [24]. In 2007, Jafri focused, on the potential of shrink fits as an internal damping component [25] and witnessed an actual breakdown during experimentation. At the same time, Chatelet and Montagnier [26] [27] elaborated on the shaft material, and in particular materials that are more dissipative than metallic materials. More recently, Chouksey investigated the influence of rotating damping on the frequency responses [28] [29]. In this research, important contributions are made towards the practical understanding of rotating damping in rotordynamic finite element models and towards its experimental validation.

1.3 Overview

Because rotating damping as a destabilizing phenomenon needs to be fully understood, *chapter 2* is entirely dedicated to the understanding and modeling of rotating damping. First, it is explained in detail how rotating damping causes a system to become unstable. Second, the linear speed dependent model and the discretization through finite elements is presented. Finally, the modal analysis and the derivation of the frequency responses and impulse responses is performed. The chapter is an important foundation to understand the remainder of the thesis.

In *chapter 3*, two experimental setups are described. The first is a rotating damping setup. This setup is designed explicitly for the experimental validation of rotating damping caused by shaft material. The different choices that are made in the design phase are clarified. The resulting setup is a rotating clamped flexible shaft that can be operated between 0 and 7000 rpm. The excitation source is an automated impact hammer to guarantee a reproducible, semi-contactless excitation signal. The displacement responses are measured by eddy current probes. The second setup is a torsional vibration setup. This setup is used because of the good accordance between the lumped mass model and the actual setup. The torsional vibration setup is mainly used to validate damping matrix identification methods.

Chapter 4 presents important theoretical insights in the linear speed dependent model. The modal model is described and the corresponding parameters such as modal mass, stiffness and damping are discussed in detail. They are complex valued, and dependent upon the scaling of the eigenvectors. By assuming lightly damped systems, perturbation analysis is used to approximate the modal mass, stiffness and damping as a combination of real and imaginary values. These in-

sights are important when simplified experimental procedures are needed.

In *chapter 5*, the first measurements are performed. The multiple degree of freedom system is approximated by a single degree of freedom equivalent by focussing on a single pole. Following the pole within a certain speed range gives rise to a decay rate plot. The approximation is justified by the modal model and the perturbation analysis. The rotating damping setup is used to perform the single degree of freedom approximation, and a decay rate plot is constructed. It is shown that the stability threshold speed can be predicted and an actual instability is achieved.

Chapter 4 and 5 focus on the rotating damping as a destabilizing mechanism. Also the estimation of the poles at different speeds is important, and therefore there is a focus on the damping matrix identification in chapter 6 and 7. In *chapter 6*, two modal methods are discussed. Modal methods reconstruct the damping matrix by using the eigenvalues and -vectors of the system. The methods are illustrated with a simulated example corresponding to the rotating damping setup. Subsequently it is described that the identification methods are highly sensitive to errors on the extracted eigenvectors. Therefore, some optimization procedures are presented.

In *chapter 7*, the damping matrix identification procedures and optimization methods that are described in chapter 6 are validated on both the torsional vibration setup and the rotating damping setup.

Chapter 8 summarizes all chapters in a main conclusion. The important contributions are emphasized and a vision on future work is provided.

2

Modeling of rotating damping

2.1 Stability in rotating machinery

2.1.1 Rotating machinery

Rotating machinery includes all machinery that is undergoing any kind of periodic angular displacement. In this broad range of applications, this research focusses on rotating damping and stability analysis. This is important for a specific class of rotating machinery, in particular, machines that are *flexible* in the *lateral direction* within the *operating speed*. These kind of rotors typically are steam turbines and high speed compressors but also helicopter driveshafts. However, all high speed rotating applications are potentially exposed to lateral vibrations. This research contributes to all manufacturers that are trying to design rotating machinery with an increased operating speed and lower dimensions. Because of the decoupling between lateral, axial and torsional vibrations (Figure 2.1), which is a common assumption [1] [30], specifically lateral vibrations are studied. High operating speeds generally means that the rotors are *isotropic* and *axisymmetric* leading to a minimized unbalance. Technically, this means that the principal axis coincides with the rotating axis. Unbalance and misalignment are a source of *forced vibration* and therefore do not influence stability which is a *free vibration* phenomenon. Although the actual instability is a transient phenomenon, the modelling and the measurements are performed at steady state.

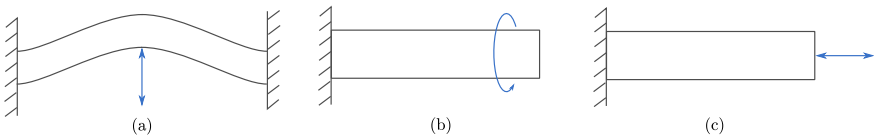

Figure 2.1: Schematic representation of different rotor vibrations (a) Lateral (b) Torsional (c) Axial

2.1.2 Free vibration, damping and self-excited vibration

The vibrations of a mechanical system, due to an initial disturbance, is a free vibration. The initial disturbance provides energy which is converted into an oscillatory motion. The frequencies at which this vibration occurs are inherent to the system and are therefore called *natural frequencies*. The oscillatory motion is a continuous conversion between kinetic and potential energy. When the energy is dissipated into another form of energy, *damping* occurs. Damping causes the oscillatory motion to *decay* as a function of time. A damped free vibration is therefore an example of a *stable system*. Whether a mechanical system is stable or not is defined for instance by Bently in [31]. A mechanical system is stable, if, when it is disturbed from its equilibrium condition, it eventually returns to that equilibrium condition. A mechanical system is unstable if, when it is disturbed, it tends to move away from that original equilibrium. A typical example to explain mechanical stability is a concave vessel filled with a viscous fluid. When there is a ball inside the vessel and a disturbance is given, the ball returns to its equilibrium (Figure 2.2a and b). The viscosity of the fluid influences the behaviour. A fluid with low viscosity causes the ball to oscillate along the equilibrium, and fluid with high viscosity causes the ball to go directly to the equilibrium without any overshoot. A flat surface is a peripheral phenomenon (Figure 2.2c). A disturbance causes the ball to move, but it neither goes back to the equilibrium, nor does it move away. This condition is sometimes called *marginal* or *neutral stability*. At last, a small disturbance on a convex surface causes the ball to move away from the equilibrium indicating an unstable situation (Figure 2.2d).

Mechanical instability causing vibrations is called *oscillatory instability* or *self-excited vibration* [1] [32]. Self-excitation means that there is a certain amount of the energy inherent to the system, causing an unwanted motion. This energy conversion acts as the opposite of damping. Figure 2.3a is an example of a free vibration with an exponential decay caused by damping. If, instead of decay there is a growth, the amplitude goes exponentially to infinity (Figure 2.3c). This phenomenon is called *negative damping* and is a form of self-excited vibration. As a consequence of positive and negative damping, there is also zero damping resulting in a marginal stable system (Figure 2.3b). An undamped free vibration is thus an example of a marginal stable system. An important remark is that a self-excited

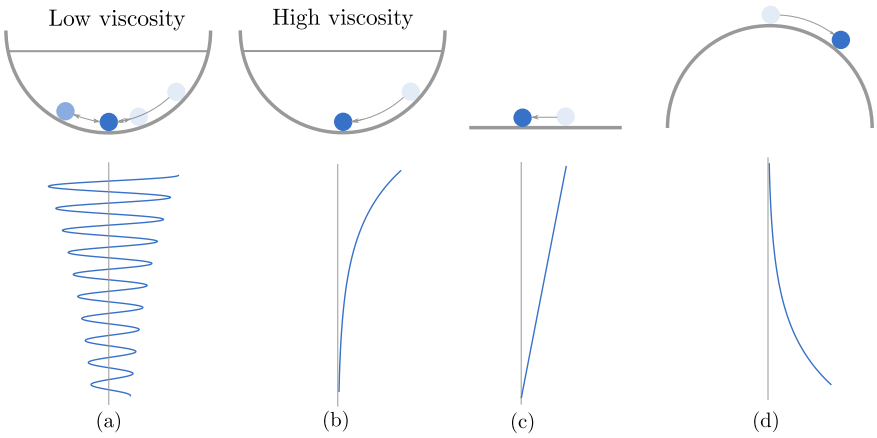

Figure 2.2: A typical explanation for mechanical stability

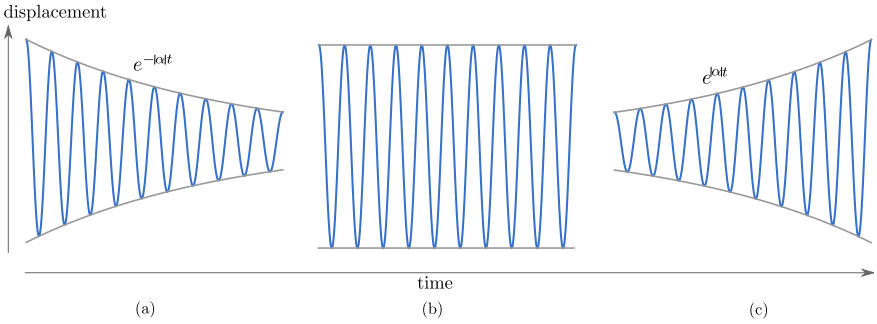

Figure 2.3: Exponential decay caused by positive damping (a), free vibration caused by zero damping (b) and exponential growth caused by negative damping (c)

vibration is a condition occurring at free vibration. The system does not need to be excited by an external force. A small initial disturbance in displacement or velocity is sufficient for the system to start vibrating at a natural frequency and for the amplitude to reach towards infinity. This is also the main difference between resonance and *instability*. Resonance is a forced vibration, steady state phenomenon and instability is a free vibration, transient phenomenon.

As positive damping removes energy from the system, negative damping adds energy to the system. This energy needs to be provided by an external source. For a rotating system, the energy distribution is shown schematically in Figure 2.4. Suppose that an actuator is causing a shaft to rotate. The actuator is an energy source that has limited power. The actuator causes the shaft to rotate, which corresponds to normal operation. The energy of the actuator is converted into rotating energy. Depending on the mechanical properties of the shaft, mainly mass,

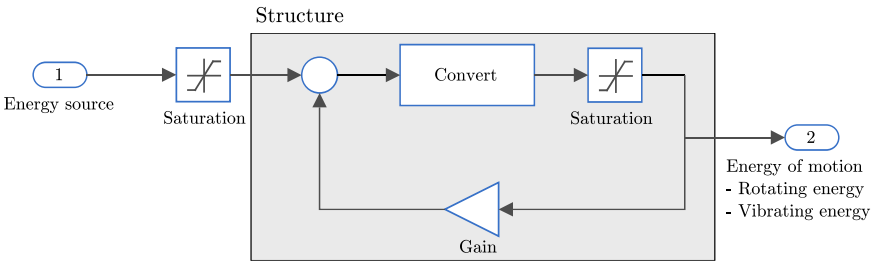

Figure 2.4: Energy distribution in a rotating machine

stiffness and damping, some of the energy is converted into unwanted motion or vibration. Negative damping causes a positive feedback of the unwanted motion resulting in a growth of the vibrating energy. An infinitely growing amplitude is therefore only a theoretical possibility. A growing amplitude is always limited. First of all, the available energy that is transformed into an unwanted vibrating motion needs to be sufficient to maintain the ever increasing amplitude. Second, when high amplitudes occur, nonlinear effects are more likely to occur. It is thus possible that an unstable system stabilizes around a new equilibrium. This can be due to nonlinear effects of the material, but also by elements that limit the movement. When both the energy in the system is sufficient, and no physical limitation occurs, an ever increasing amplitude results in a breakdown or failure.

2.2 The nature of rotating damping instability

2.2.1 Spin and free whirl

The motion of a flexible rotor operated at a certain rotating speed is a combination of *rotor spin* and *whirl*. The spin is the motion caused by the operating speed and the whirl is a circular motion corresponding to a critical speed or a natural frequency. Spin, denoted by Ω, is the wanted motion and whirl, denoted by ω, is an unwanted motion. In the absence of external forces whirl is a transient phenomenon depending upon an initial disturbance and is called free whirl. A forced excitation, such as unbalance, causes a forced whirl which is a steady state phenomenon. The frequency of the free whirling corresponds to a natural frequency of the rotor. Figure 2.5 shows a whirling shaft and Figure 2.6 depicts how a disturbance causes a shaft to whirl freely and how the whirling motion dies out in time. Because spin and whirl are independent motions the frequencies can differ. Synchronous whirl happens when the whirling frequency equals the spin frequency, otherwise it is asynchronous whirl. In Figure 2.7, a section of a whirling shaft is given, showing the difference between synchronous and asynchronous whirl. The

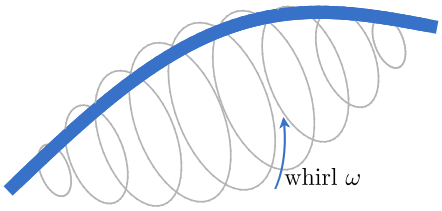

Figure 2.5: Circular whirling of a flexible rotor

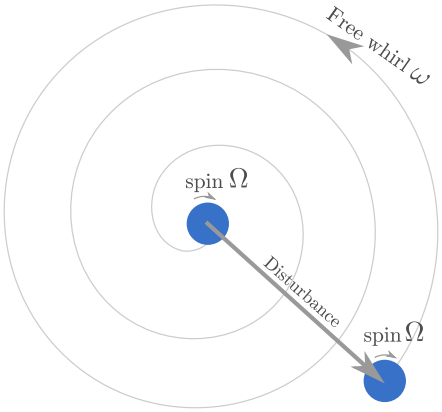

Figure 2.6: Free whirl with a negative decay

centre of mass executes an orbital motion and the blue marker indicates the spinning around the centre of mass. Whirling motion can also be *forward* or *backward*. A forward whirl means that the sign of both spin and whirl are the same and backward whirling is the opposite. The behaviour of forward and backward whirl on the stability is explained later on.

2.2.2 Rotating damping as a negative damping effect

Many authors provide an explanation for rotating damping as a destabilizing effect [11] [33] [24]. As this negative damping effect is not intuitive, it is sometimes difficult to interpret. In order to make reliable measurements it is of paramount importance to have a detailed understanding of this destabilizing effect. Therefore, the following paragraph is dedicated to the physical interpretation of rotating damping as a negative damping effect. In a rotating system, negative damping is caused by a *follower force*. A follower force is a force that tends to enhance an existing motion, and thus follows the motion. From an energy point of view, a follower force imparts energy to the system. A tailwind, when cycling for instance, is an example of a follower force. From the point of view of rotating systems,

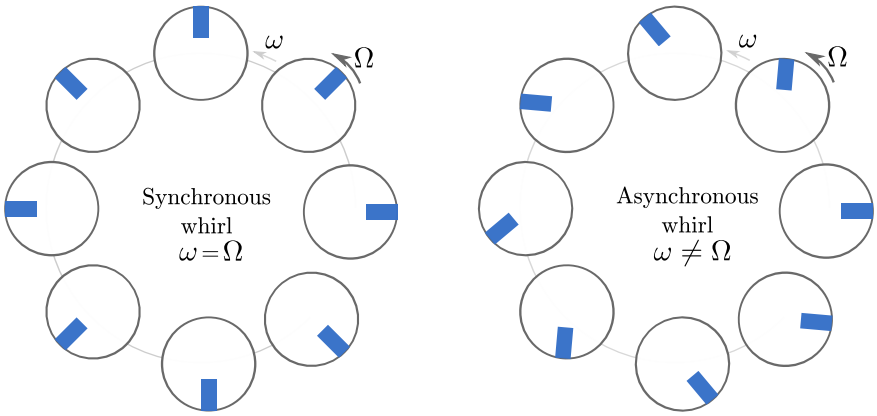

Figure 2.7: Difference between synchronous and asynchronous whirl

the rotating dashpot is a nice example of a follower force causing rotating instability [30]. Suppose that a simple pendulum is whirling freely at a certain angular speed ω as shown in Figure 2.8. The mass of the pendulum is damped by a viscous fluid in a dashpot. Depending upon the viscosity, the whirling motion dies out in time. The force that causes this decay is proportional to the absolute velocity difference between the mass and the fluid and is opposing the whirling motion. Now let the dashpot rotate at a certain angular speed Ω. The absolute velocity difference between the whirl and the fluid is proportional to $\omega - \Omega$. When $\Omega > \omega$, the whirling motion grows. This growth is due to the force between the mass and the fluid that is enhancing the whirling motion. The force is thus following the motion and acts as a follower force.

When a rotor is subjected to spin and whirl, and both speeds are different from each other, the forces that occur inside the rotor due to the stress-strain relation are also different. Suppose that the rotor is a slender shaft and has a linear visco-elastic stress-strain relation for which the behaviour is depicted in Figure 2.9. The stress, σ, is proportional to the force and the strain, ϵ, to the displacement. The force-displacement behaviour is represented by a spring-dashpot system. A material that is exposed to this stress-strain curve is dissipating energy and the dissipated energy is proportional to the area inside the curve. In the case of a slender shaft with a small curvature, it is reasonable to assume that point A is the point of maximum positive stress and strain and point D maximum negative stress and strain (or compression). If such a system is subjected to a harmonically varying force

$$f(t) = F_0 \mathrm{e}^{i\theta t} \tag{2.1}$$

where F_0 is the maximum force, and θ the cyclic frequency, the energy that is

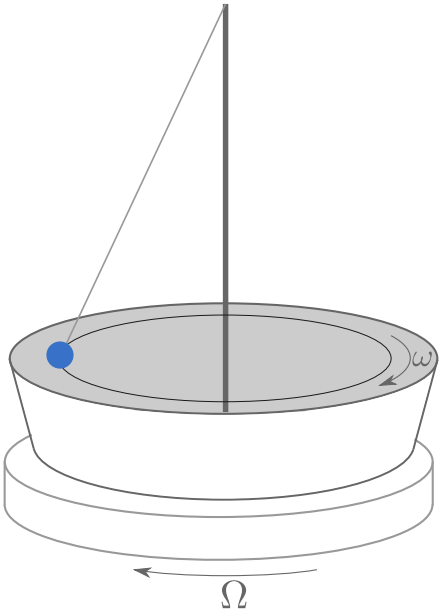

Figure 2.8: Rotating dashpot causing a follower force

dissipated equals

$$E_d = \pi c X_0^2 \theta \tag{2.2}$$

with X_0 the maximum amplitude of motion, c the damping and θ the cyclic pulsation. Suppose that a non-rotating shaft is bending, there exists a restoring force f_r (Figure 2.10). This restoring force is perpendicular to the line of neutral stress, or EB on the stress-strain curve or the hysteretic cycle (Figure 2.9). For the non-rotating bending shaft, this line coincides with the line of neutral strain. At the top of the shaft, the strain and stress is maximal and at the bottom, the compression and negative stress is maximal. By the restoring force, f_r the shaft is pushed back to an equilibrium.

For a spinning and whirling shaft, the restoring force is different. Three different situations are depicted in Figure 2.11-2.13, accompanied by a hysteric cycle of the stress-strain relation in Figure 2.14. It is recommended for the reader to read this text together with the schematic representation of the shaft section and the stress-strain relation that is depicted. The purpose is to find *the restoring force* in these situations. This implies finding the line of neutral stress as stated above. The whirl is causing the shaft to bend. Therefore it is always possible to locate the points A and D. The line of neutral strain is also easy to locate, as this is in between strain and compression. However, in the initial situation (1 on the Figure

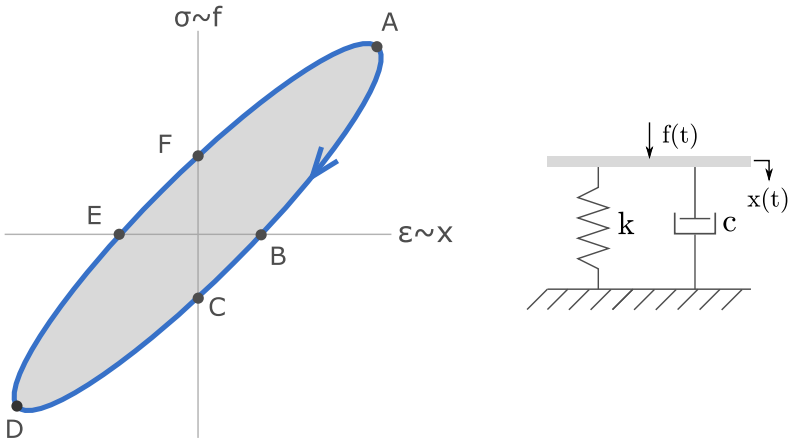

Figure 2.9: Stress-strain, or force displacement relation of a material with linear visco-elastic behaviour represented as a spring-dashpot system

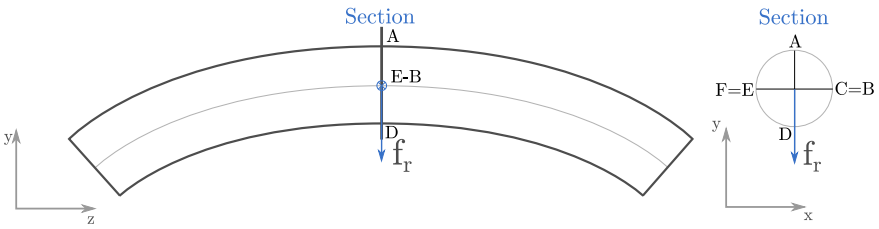

Figure 2.10: Restoring force of a non-rotating bending shaft

2.11-2.13), F and C can be located at both sides of this line of neutral strain. It is only until the shaft starts moving, that the exact locations can be found. When the whirl speed is higher than the spin speed or $\omega > \Omega$ (Figure 2.11), the spinning motion lags the whirling motion. The shaft, going from 1 to 2, causes the material to go through the hysteretic cycle, A to A' and D to D'. When the shaft is moving further, at a certain point A' and D' will coincide with the line of neutral strain. This happens at 3. By following the hysteretic cycle, it can be seen that A' went from A to C, and that D' went from D to F. Now the exact line of neutral strain is known. Because the material traveled from being strained in 1, point A, to neutral strain in 3, point C, according to the stress-strain relation, it had to pass neutral stress, point B. It is now possible to locate point B, which is somewhere between A and C. The same can be said for point D. The material traveled from being compressed in 1, point D, to neutral strain in 3, point F. Therefore it had to pass neutral stress, point E. The line of neutral stress, BE is found. Now that this line is located, the restoring force f_r is found, as shown in 4. This force has two components, one facing the centre and a second opposing the whirling motion. Consequently, when $\omega > \Omega$, damping occurs. In contrast, when $\omega < \Omega$ (Figure 2.12) the opposite happens. When the shaft is going from 1 to 2, the spinning motion is leading the whirling motion. In the situation, at 3 where $A' = C$ and $D' = A$, the line of neutral stress can again be found. However, the orientation of this line is now mirrored compared to the previous one. This means that the perpendicular restoring force, shown in 4, again has two components, but one of the components is enforcing the whirling motion. The latter is thus a follower force. To summarize, when passing a whirling speed, a sign change occurs in the damping and instability occurs if no other damping forces are present. In between the positive and negative damping, there is also the situation of zero damping. This happens when $\omega = \Omega$ and is shown as a third case in Figure 2.13. This material is not going through the hysteretic at all and the only restoring force that exists is facing towards the centre.
It is important to notice that rotating damping is not limited towards internal damping in the rotor material. Whenever there is energy dissipation toward the rotating frame, this phenomenon can occur. Also, the linear stress-strain relation of Figure 2.9 not necessary. The only necessary factor is that there is a phase difference between stress and strain or that a hysteretic cycle exists. Rotating damping is thus not only caused by internal damping in the rotor, but also, and more pronounced by friction between different components of the rotor. One example are shrink fits that are a potential source of rotating damping [25].

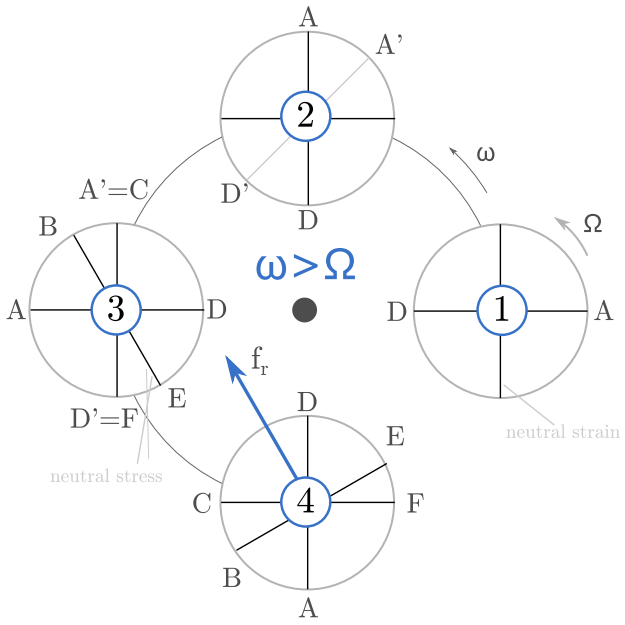

Figure 2.11: Restoring force of a bending beam when $\omega > \Omega$

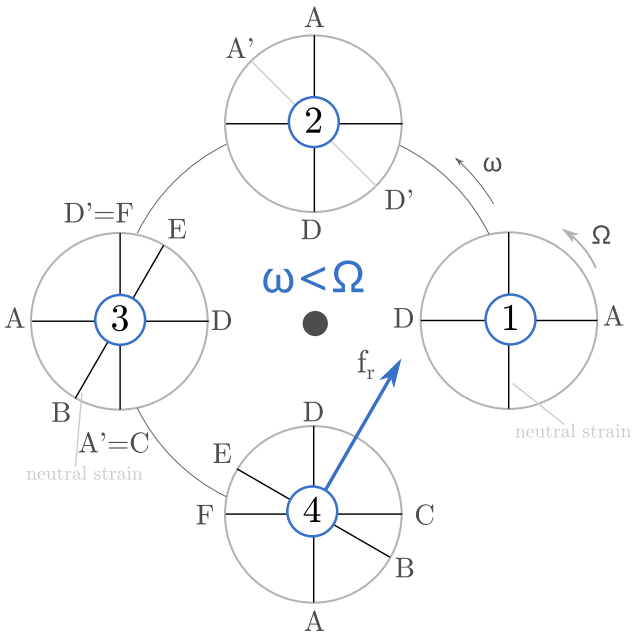

Figure 2.12: Restoring force of a bending beam when $\omega < \Omega$

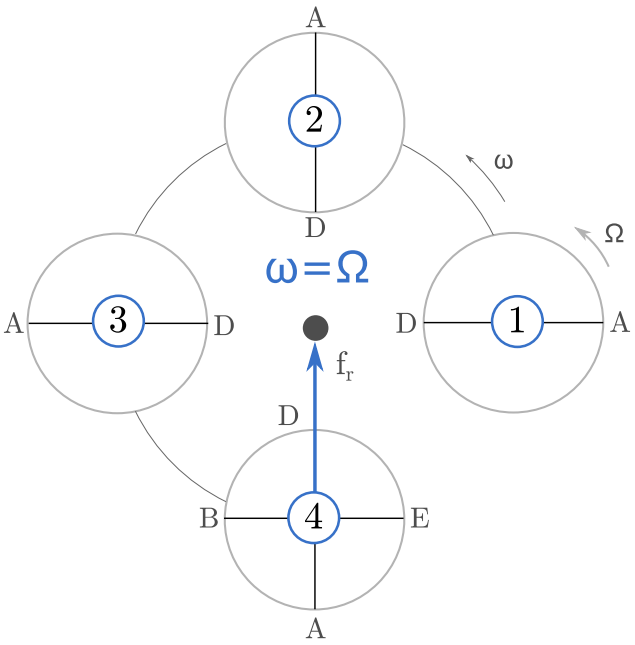

Figure 2.13: Restoring force of a bending beam when $\omega = \Omega$

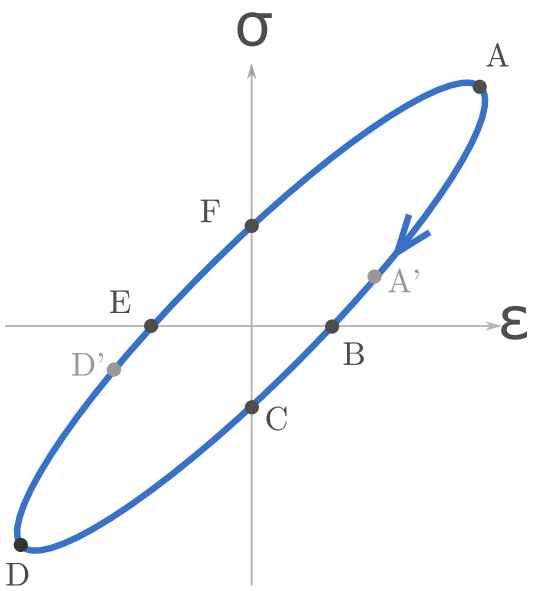

Figure 2.14: Hysteretic cycle of the stress-strain relation. This figure accompanies Figure 2.11-2.13

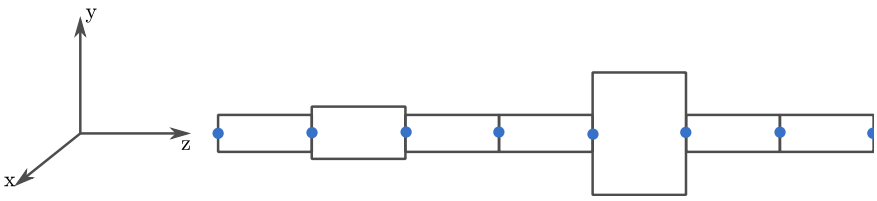

Figure 2.15: Example of a discrete division of a rotor into finite elements

2.3 The linear speed dependent model

In order to investigate the behaviour of rotating damping in an actual rotating system, the rotor is modelled as in a linear speed dependent model. First, the discritization is discussed and the mass, stiffness and damping matrices are derived. Second, modal analysis is used, which allows the system to be studied in single modes.

2.3.1 The discrete multiple degree of freedom rotor

The dynamic behaviour of rotating machinery is generally described by a discrete multiple degree of freedom model. A common method of discritization is the finite element technique. The rotor is divided into finite elements from which the number of degrees of freedom depends on the application and the presumed results. A representation of such a division in finite elements is shown in Figure 2.15. Every element has its own material and geometric properties linked to the actual rotor. The elements are connected through nodes, the blue dots on the figure. At each node, extra mass, stiffness or damping can be added.

Each element has four degrees of freedom: two translations (u_{xi},u_{yi}), and two rotations (θ_{yi},θ_{xi}) (Figure 2.16). The generalized coordinates are ordered such that the u_x and θ_y coordinates are followed by the u_y and θ_x coordinates.

$$\mathbf{q}_x = \begin{bmatrix} u_{xi} & \theta_{yi} & u_{xi+1} & \theta_{yi+1} & \dots \end{bmatrix}^T \tag{2.3}$$

$$\mathbf{q}_y = \begin{bmatrix} u_{yi} & \theta_{xi} & u_{yi+1} & \theta_{xi+1} & \dots \end{bmatrix}^T \tag{2.4}$$

$$\mathbf{q} = \begin{bmatrix} \mathbf{q}_x \\ \mathbf{q}_y \end{bmatrix} \tag{2.5}$$

The equations of motion of the rotor are derived with the Lagrange equations

$$\frac{d}{dt}\left(\frac{\partial T}{\partial \dot{q}_i}\right) - \frac{\partial T}{\partial q_i} + \frac{\partial D}{\partial \dot{q}_i} + \frac{\partial V}{\partial q_i} = Q_i \quad i = 1, 2, \dots, n \tag{2.6}$$

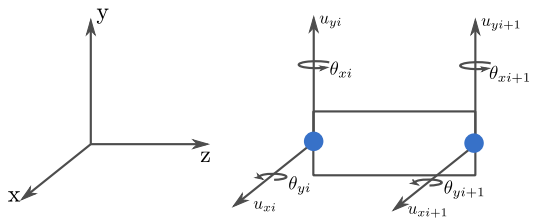

Figure 2.16: Schematic representation of one element with four degrees of freedom per node

where q_i and $\dot{q}_i$ are the generalized coordinates and velocities. T is the kinetic energy, V the potential energy, and D the dissipation energy. Q_i is the sum of generalized forces and n the number of degrees of freedom. A first approximation of the system can be that mass, stiffness and damping are divided equally or *lumped* along the nodes. A more accurate approximation is a distributed technique. In this technique, the kinetic, potential and dissipation energy are defined per unit of length and then integrated over the whole length of the element. The actual displacement and velocity are a function of the generalized coordinates

$$u_x = u_{xi}N_1(z) + \theta_{yi}N_2(z) + u_{xi+1}N_3(z) + \theta_{yi+1}N_4(z) \tag{2.7}$$
$$u_y = u_{yi}N_1(z) + \theta_{xi}N_2(z) + u_{yi+1}N_3(z) + \theta_{xi+1}N_4(z) \tag{2.8}$$

where $N_{1,2,3,4}(z)$ are deflection shape functions. Generally, the deflection shape functions are chosen as cubic expressions. Details can be found in [1].

$$\begin{aligned} N_1(z) &= 1 - 3\left(\frac{z}{L}\right)^2 + 2\left(\frac{z}{L}\right)^3 & N_3(z) &= 3\left(\frac{z}{L}\right)^2 - 2\left(\frac{z}{L}\right)^3 \\ N_2(z) &= z - 2\frac{z^2}{L} + \frac{z^3}{L^2} & N_4(z) &= \frac{z^2}{L}\left(\frac{z}{L} - 1\right) \end{aligned} \tag{2.9}$$

With L the length of one element. In the following sections, the kinetic, potential and dissipation energy are derived for a rotor. First, the Euler angles are explained.

2.3.1.1 Euler angles

The kinematic concepts of a rotor can be explained considering a rigid body on a massless compliant shaft (Figure 2.17). The disk is symmetric, isotropic and the principal axis of the shaft crosses the center of mass. The inertial frame is defined as $(\mathbf{x}_0\mathbf{y}_0\mathbf{z}_0)$. It is first translated to the disk's center of mass in $(\mathbf{xyz})$. The rotating frame $(\mathbf{x}'\mathbf{y}'\mathbf{z}')$ is fixed to the rotor and rotating at an angular spin speed Ω. The relation between the inertial frame and the rotating frame is defined through

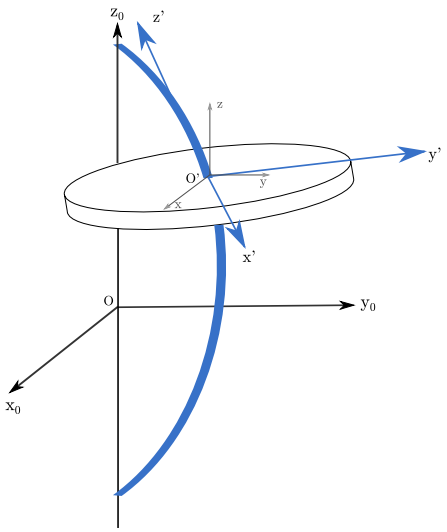

Figure 2.17: A rigid body disk on a massless compliant shaft

a translation, from the origin to the center of mass, and three rotations. These rotations are typically defined by Euler angles as shown in Figure 2.18 [1] [30]. The three rotations are occurring at the different planes. The first rotation is θ_x around the x-axis in plane 1. This gives rise to a new frame (**uvw**), where $\mathbf{u} = \mathbf{x}$. The relation between the two frames is

$$\begin{bmatrix} \mathbf{u} \\ \mathbf{v} \\ \mathbf{w} \end{bmatrix} = \mathbf{R}_1 \begin{bmatrix} \mathbf{x} \\ \mathbf{y} \\ \mathbf{z} \end{bmatrix} = \begin{bmatrix} 1 & 0 & 0 \\ 0 & \cos(\theta_x) & \sin(\theta_x) \\ 0 & -\sin(\theta_x) & \cos(\theta_x) \end{bmatrix} \begin{bmatrix} \mathbf{x} \\ \mathbf{y} \\ \mathbf{z} \end{bmatrix} \tag{2.10}$$

The second rotation is θ_v around the v-axis and in plane 2

$$\begin{bmatrix} \mathbf{i} \\ \mathbf{j} \\ \mathbf{k} \end{bmatrix} = \mathbf{R}_2 \begin{bmatrix} \mathbf{u} \\ \mathbf{v} \\ \mathbf{w} \end{bmatrix} = \begin{bmatrix} \cos(\theta_v) & 0 & -\sin(\theta_v) \\ 0 & 1 & 0 \\ \sin(\theta_v) & 0 & \cos(\theta_v) \end{bmatrix} \begin{bmatrix} \mathbf{u} \\ \mathbf{v} \\ \mathbf{w} \end{bmatrix} \tag{2.11}$$

The third rotation is θ_k about the k-axis is plane 3

$$\begin{bmatrix} \mathbf{x}' \\ \mathbf{y}' \\ \mathbf{z}' \end{bmatrix} = \mathbf{R}_3 \begin{bmatrix} \mathbf{i} \\ \mathbf{j} \\ \mathbf{k} \end{bmatrix} = \begin{bmatrix} \cos(\theta_k) & \sin(\theta_k) & 0 \\ -\sin(\theta_k) & \cos(\theta_k) & 0 \\ 0 & 0 & 1 \end{bmatrix} \begin{bmatrix} \mathbf{i} \\ \mathbf{j} \\ \mathbf{k} \end{bmatrix} \tag{2.12}$$

Note that angular speed of the third rotation around the k-axis, $\dot{\theta}_k$ coincides with the rotation of the disk about the shaft. Therefore, this is equal to the angular speed Ω of the rotor.

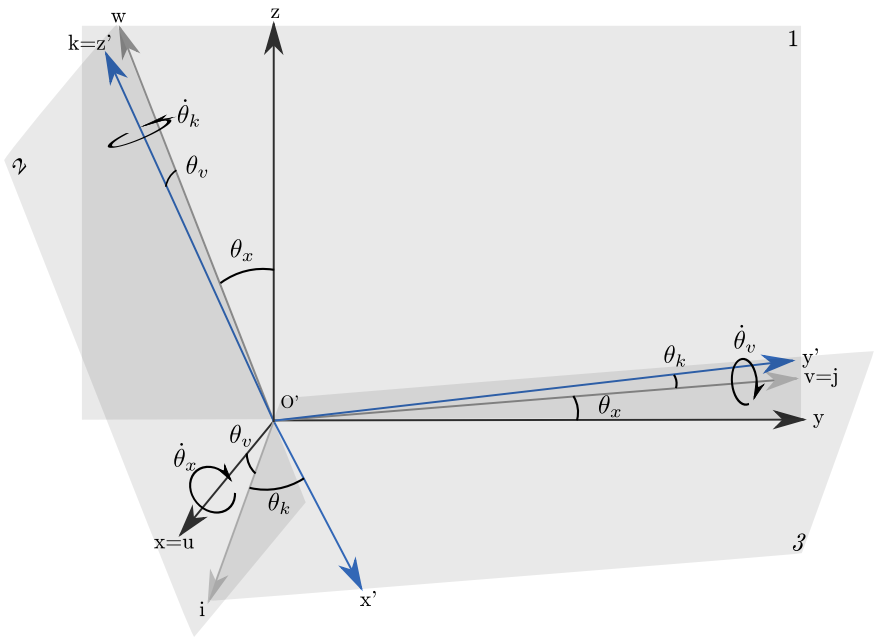

Figure 2.18: Euler angles explained

2.3.1.2 Kinetic energy of a rotor

The kinetic energy, T, of this system is a combination of the translational and the rotational energy:

$$T = T_t + T_r = \frac{1}{2} m \mathbf{V}_p^T \mathbf{V}_p + \frac{1}{2} \boldsymbol{\Omega}^T \mathbf{J} \boldsymbol{\Omega} \tag{2.13}$$

where T_t and T_r are respectively the translational and rotational kinetic energy, m is the mass, $\mathbf{V}_p = [\dot{x}\ \dot{y}\ \dot{z}]^T$ is the absolute velocity of the center of mass, $\boldsymbol{\Omega}$ is the angular velocity vector and $\mathbf{J}$ the inertia tensor of the rotor.

$$\mathbf{J} = \begin{bmatrix} J_x & 0 & 0 \\ 0 & J_y & 0 \\ 0 & 0 & J_z \end{bmatrix} \tag{2.14}$$

for the axisymmetrical rotor, $J_x = J_y = J_t$ or the transverse moment of inertia and $J_z = J_p$ or the polar moment of inertia. The angular velocity vector is the sum of the three velocity vectors $\dot{\boldsymbol{\theta}}_x, \dot{\boldsymbol{\theta}}_v, \dot{\boldsymbol{\theta}}_k$ with respect to the principal axes of inertia of the rotor

$$\boldsymbol{\Omega} = \mathbf{R}_3 \left(\mathbf{R}_2 \begin{bmatrix} \dot{\boldsymbol{\theta}}_x \\ 0 \\ 0 \end{bmatrix} + \begin{bmatrix} 0 \\ \dot{\boldsymbol{\theta}}_v \\ 0 \end{bmatrix} \right) + \begin{bmatrix} 0 \\ 0 \\ \dot{\boldsymbol{\theta}}_k \end{bmatrix} \tag{2.15}$$

or

$$\boldsymbol{\Omega} = \begin{bmatrix} \dot{\theta}_v \sin(\theta_k) + \dot{\theta}_x \cos(\theta_k) \cos(\theta_v) \\ \dot{\theta}_v \cos(\theta_k) - \dot{\theta}_x \cos(\theta_v) \sin(\theta_k) \\ \dot{\theta}_k + \dot{\theta}_x \sin(\theta_v) \end{bmatrix} \tag{2.16}$$

In reality, for a rotor, θ_x and θ_v are small angles. This means that the approximation of $\sin(\theta_x) \approx \theta_x$ and $\cos(\theta_v) \approx 1$ can be made. As mentioned before $\dot{\theta}_k = \Omega$

$$\boldsymbol{\Omega} = \begin{bmatrix} \dot{\theta}_v \sin(\Omega) + \dot{\theta}_x \cos(\Omega) \\ \dot{\theta}_v \cos(\Omega) - \dot{\theta}_x \sin(\Omega) \\ \Omega + \dot{\theta}_x \theta_v \end{bmatrix} \tag{2.17}$$

By using equation (2.13), and neglecting the small terms, the combined kinetic energy is

$$T = \frac{m}{2} \left(\dot{x}^2 + \dot{y}^2 + \dot{z}^2 \right) + \frac{J_t}{2} \left(\dot{\theta}_x^2 + \dot{\theta}_v^2 \right) + \frac{J_z}{2} \left(\Omega^2 + 2\Omega\theta_v \dot{\theta}_x \right) \tag{2.18}$$

The kinetic energy not only depends on the velocities, as common in non-rotating systems, but also on the angular displacement θ_v. Moreover, the kinetic energy varies as a function of the spin speed Ω.

2.3.1.3 Dissipation energy of a rotor

A straightforward way to describe the dissipation energy of a rotor is difficult. A mathematical convenient way is to use the Rayleigh dissipation function [30]. The Rayleigh dissipation function is a function similar to the kinetic energy. The energy of the disk in Figure 2.17 is

$$D = \frac{1}{2} c_r \left(\dot{x}'^2 + \dot{y}'^2 + \dot{z}'^2 \right) \tag{2.19}$$

where c_r is the rotating damping and

$$\begin{bmatrix} x' \\ y' \\ z' \end{bmatrix} = \mathbf{R} \begin{bmatrix} x \\ y \\ z \end{bmatrix} \tag{2.20}$$

with $\mathbf{R} = \mathbf{R}_1\mathbf{R}_2\mathbf{R}_3$, thus

$$\begin{bmatrix} \dot{x}' \\ \dot{y}' \\ \dot{z}' \end{bmatrix} = \mathbf{R} \begin{bmatrix} \dot{x} \\ \dot{y} \\ \dot{z} \end{bmatrix} + \dot{\mathbf{R}} \begin{bmatrix} x \\ y \\ z \end{bmatrix} \tag{2.21}$$

The dissipation energy can be written as

$$D = \frac{1}{2} c_r \left(\begin{bmatrix} \dot{x} \\ \dot{y} \\ \dot{z} \end{bmatrix} \mathbf{R}^T + \begin{bmatrix} x \\ y \\ z \end{bmatrix} \dot{\mathbf{R}}^T \right) \left(\mathbf{R} \begin{bmatrix} \dot{x} \\ \dot{y} \\ \dot{z} \end{bmatrix} + \dot{\mathbf{R}} \begin{bmatrix} x \\ y \\ z \end{bmatrix} \right) \tag{2.22}$$

or

$$D = \frac{1}{2} c_r \left(\dot{x}^2 + \dot{y}^2 + \dot{z}^2 \right) + \frac{1}{2} c_r \Omega^2 \left(x^2 + y^2 \right) + c_r \Omega \left(\dot{x}y - \dot{y}x \right) \tag{2.23}$$

The dissipation energy thus depends on both velocities and displacements, which also differs from non-rotating systems. Moreover, it is a function of the spin speed Ω. The Rayleigh dissipation function is certainly not the only way of representing damping. However, it is important to notice that the purpose of this research is to find experimental procedures that both validate and update the model, and that help in de prediction of the stability threshold speed. The choice of the Rayleigh dissipation function is therefore the best as it will lead to an experimentally friendly model, described in chapter 5.

2.3.1.4 Mass, stiffness and damping matrices of a single element

The potential energy for the element bending, with a length L, in x- and y-direction is written as

$$V_x = \frac{1}{2} E I_x \int_0^L \left(\frac{\partial^2 u_x}{\partial z^2} \right)^2 dz \quad \text{and} \quad V_y = \frac{1}{2} E I_y \int_0^L \left(\frac{\partial^2 u_y}{\partial z^2} \right)^2 dz \tag{2.24}$$

where E is the Young modulus and I_x and I_y are the area moments of inertia in x- and y-direction. This can also be written by using the generalized coordinates $\mathbf{q}$

$$V_x = \frac{1}{2} \mathbf{q}_x^T \mathbf{K}_x \mathbf{q}_x dz \quad \text{and} \quad V_y = \frac{1}{2} \mathbf{q}_y^T \mathbf{K}_y \mathbf{q}_y dz \tag{2.25}$$

where $\mathbf{K}_x$ and $\mathbf{K}_y$ are the stiffness matrices in x- and y-direction. By combining (2.8) and (2.24) and rearranging it to (2.25), such a stiffness matrix becomes

$$\mathbf{K} = \frac{EI}{L^3}\begin{bmatrix} 12 & 6L & -12 & 6L \\ & 4L^2 & -6L & 2L^2 \\ & & 12 & -6L \\ & symm & & 4L^2 \end{bmatrix} \tag{2.26}$$

which is the stiffness matrix of a single in a single direction. For the kinetic energy, (2.18) is used. As z remains constant in time, when lateral vibrations are concerned, the kinetic energy is computed as

$$T = \frac{1}{2}\rho A \int_0^L \left(\dot{u}_x^2 + \dot{u}_y^2\right) dz + \frac{1}{2}\rho J_t \int_0^L \left(\dot{\theta}_x^2 + \dot{\theta}_v^2\right) dz + \rho J_p \int_0^L \left(\Omega^2 + 2\Omega\theta_v\dot{\theta}_x\right) dz \tag{2.27}$$

where ρ is the density, A the cross section, and I the area moment of inertia. The angles are

$$\theta_x = \frac{\partial u_x}{\partial z} \quad \text{and} \quad \theta_y = \frac{\partial u_y}{\partial z} \tag{2.28}$$

thus (2.27) can be written in generalized coordinates

$$T = \frac{1}{2}\dot{\mathbf{q}}_x^T\mathbf{M}_T\dot{\mathbf{q}}_x + \frac{1}{2}\dot{\mathbf{q}}_y^T\mathbf{M}_T\dot{\mathbf{q}}_y + \frac{1}{2}\dot{\mathbf{q}}_x^T\mathbf{M}_R\dot{\mathbf{q}}_x + \frac{1}{2}\dot{\mathbf{q}}_y^T\mathbf{M}_R\dot{\mathbf{q}}_y + \rho J_p l\Omega^2 + 2\Omega\dot{\mathbf{q}}_y^T\mathbf{M}_R\mathbf{q}_x \tag{2.29}$$

$$\mathbf{M}_T = \frac{\rho AL}{420}\begin{bmatrix} 156 & 22L & 54 & -13L \\ & 4L^2 & 13L & -3L^2 \\ & & 156 & -22L \\ & symm & & 4L^2 \end{bmatrix} \tag{2.30}$$

$$\mathbf{M}_R = \frac{\rho J_t}{30L}\begin{bmatrix} 36 & 3l & 36 & -3L \\ & 4L^2 & 3L & -1L^2 \\ & & 36 & -3L \\ & symm & & 4L^2 \end{bmatrix} \tag{2.31}$$

and

$$\mathbf{M} = \mathbf{M}_T + \mathbf{M}_R, \quad \mathbf{G} = 2\mathbf{M}_R \tag{2.32}$$

M is called the consistent mass matrix and **G** the gyroscopic matrix. From the Rayleigh dissipation function

$$D = \frac{1}{2}\frac{c_r}{L}\int_0^L (\dot{u}_x^2 + \dot{u}_y^2)dz + \frac{1}{2}\frac{c_r}{L}\Omega^2\int_0^L (u_x^2 + u_y^2)dz + \frac{1}{2}\frac{c_r}{L}\Omega\int_0^L (\dot{u}_x u_y - \dot{u}_y u_x)dz \tag{2.33}$$

$$D = \frac{1}{2}\dot{\mathbf{q}}_x^T\mathbf{C}_r\dot{\mathbf{q}}_x + \frac{1}{2}\dot{\mathbf{q}}_y^T\mathbf{C}_r\dot{\mathbf{q}}_y + \frac{1}{2}\mathbf{q}_x^T\mathbf{A}\mathbf{q}_x + \frac{1}{2}\mathbf{q}_y^T\mathbf{A}\mathbf{q}_y + 2\Omega\dot{\mathbf{q}}_y^T\mathbf{C}_r\mathbf{q}_x \tag{2.34}$$

$$\mathbf{C}_R = \frac{c_r}{420}\begin{bmatrix} 156 & 22l & 54 & -13L \\ & 4L^2 & 13L & -3L^2 \\ & & 156 & -22L \\ & symm & & 4L^2 \end{bmatrix} \tag{2.35}$$

The terms in q_x and q_y disappear in the Lagrange equations. This means that **A** is not relevant in equation (2.34).

2.3.1.5 Combining the elements to a model

By combining the elements and using the Langrange equations, the equations of motion are obtained

$$\begin{bmatrix}\mathbf{M} & \mathbf{0}\\ \mathbf{0} & \mathbf{M}\end{bmatrix}\begin{bmatrix}\ddot{\mathbf{q}}_x\\ \ddot{\mathbf{q}}_y\end{bmatrix} + \left(\begin{bmatrix}\mathbf{C}_n + \mathbf{C}_r & \mathbf{0}\\ \mathbf{0} & \mathbf{C}_n + \mathbf{C}_r\end{bmatrix} + \Omega\begin{bmatrix}\mathbf{0} & \mathbf{G}\\ -\mathbf{G} & \mathbf{0}\end{bmatrix}\right)\begin{bmatrix}\dot{\mathbf{q}}_x\\ \dot{\mathbf{q}}_y\end{bmatrix} + \tag{2.36}$$
$$\left(\begin{bmatrix}\mathbf{K} & \mathbf{0}\\ \mathbf{0} & \mathbf{K}\end{bmatrix} + \Omega\begin{bmatrix}\mathbf{0} & \mathbf{C}_r\\ -\mathbf{C}_r & \mathbf{0}\end{bmatrix}\right)\begin{bmatrix}\mathbf{q}_x\\ \mathbf{q}_y\end{bmatrix} = \begin{bmatrix}\mathbf{f}_x\\ \mathbf{f}_y\end{bmatrix} \quad \text{with} \quad \begin{bmatrix}\mathbf{q}_x\\ \mathbf{q}_y\end{bmatrix}, \begin{bmatrix}\mathbf{f}_x\\ \mathbf{f}_y\end{bmatrix} \in \mathbb{R}^{n\times 1}$$

Where $\mathbf{C}_n$ is the non-rotating damping matrix. This non-rotating damping matrix is generally not distributed. The damping in a bearing for instance is has a specific location and can be added to one node of the finite element model. This means that it is added to a diagonal element in the matrix corresponding to the physical location. The same can be done for disks, that add mass and gyroscopic effect. The stiffness matrix is also affected by boundary conditions such as bearings. A first important remark on these equations of motion is the speed dependency. Both gyroscopic and rotating damping matrix introduce a speed dependency. The model is changing as a function of speed, so the resulting poles are also speed dependent. Second, the gyroscopic effect and the rotating damping cause a skew-symmetric coupling. This has an impact on both the dynamic analysis and the possible experimental techniques which is explained later on. The equations of motion can also be written as

$$\mathbf{M}\ddot{\mathbf{q}} + (\mathbf{C}_n + \mathbf{C}_{rs} + \Omega\mathbf{G})\,\dot{\mathbf{q}} + (\mathbf{K} + \Omega\mathbf{C}_{rss})\,\mathbf{q} = \mathbf{f} \quad \text{with} \quad \mathbf{q}, \mathbf{f} \in \mathbb{R}^{n\times 1} \tag{2.37}$$

where $\mathbf{C}_{rs}$ is the symmetric part of the rotating damping and $\mathbf{C}_{rss}$ is the skew-symmetric part

2.3.2 Modal analysis

Modal analysis is the study of the dynamical properties of mechanical systems by subdividing the motion into *modes*. Each mode is linked to a natural frequency, *relative damping* and a *modeshape*. The dynamic behaviour of the mechanical system is a linear combination of several modes. The key to modal analysis is the decoupling of a multiple degree of freedom model into several single degree of freedom models. The resulting decoupled equations each have a single mass, damping and stiffness generally called the modal parameters. From a theoretical point of view, modal analysis is a straightforward technique to gain insight into the system and for the calculation of time and frequency responses. From an experimental point of view, modal analysis is widely spread as a technique to extract the dynamic properties of a mechanical system. The latter is generally called experimental modal analysis or modal testing. Experimental modal analysis is generally based upon the frequency response function between an input or excitation force and an output displacement, velocity or acceleration. The frequency response functions between force and displacement, velocity and acceleration are respectively called *receptance*, *mobility* and *accelerance*. The techniques are widely spread and described in almost every textbook on mechanical vibrations. [2] [34] [35] [36]

However, classic modal analysis is generally based upon the assumption that the system matrices are symmetric and time invariant. The equations of motion (2.37) are neither. Nevertheless, at a constant speed, the model is linear time invariant and can be treated as such. The spin speed Ω is generally known or easy to measure and therefore of minor concern. More important is the skew-symmetry introduced by both the gyroscopic effect and the rotating damping. In fact, (2.37) is a general dynamic system as described by Meirovitch in [7]. By letting $\mathbf{f} = \mathbf{0}$, free vibration is studied. The equations of motion can be rewritten in *state space* as

$$\mathbf{A}\dot{\mathbf{z}} + \mathbf{B}\mathbf{z} = \mathbf{0} \quad \text{with} \quad \mathbf{z}, \mathbf{0} \in \mathbb{R}^{2n\times 1} \tag{2.38}$$

with

$$\mathbf{A} = \begin{bmatrix} \mathbf{C}_n + \mathbf{C}_{rs} + \Omega\mathbf{G} & \mathbf{M} \\ \mathbf{M} & \mathbf{0} \end{bmatrix} \quad ; \quad \mathbf{B} = \begin{bmatrix} \mathbf{K} + \Omega\mathbf{C}_{rss} & \mathbf{0} \\ \mathbf{0} & -\mathbf{M} \end{bmatrix} \quad ; \quad \mathbf{z} = \begin{bmatrix} \mathbf{q} \\ \dot{\mathbf{q}} \end{bmatrix} \tag{2.39}$$

The Laplace transform, when the initial conditions are 0, of (2.38) is

$$(\mathbf{A}s + \mathbf{B})\,\mathbf{Z}(s) = \mathbf{0} \tag{2.40}$$

This can be transformed into a general eigenvalue problem

$$(\mathbf{A}\lambda + \mathbf{B})\,\tilde{\boldsymbol{\psi}} = 0 \tag{2.41}$$

where λ is an *eigenvalue* and $\tilde{\boldsymbol{\psi}}$ an *eigenvector* of the form

$$\tilde{\boldsymbol{\psi}} = \begin{bmatrix} \boldsymbol{\psi} \\ \boldsymbol{\psi}\lambda \end{bmatrix} \tag{2.42}$$

It is assumed that all eigenvalues are distinct. If n is the number of degrees of freedom of the original system, then there are $2n$ eigenvalues that come in complex conjugate pairs [37]. The matrices **A** and **B** are not symmetric nor skew-symmetric. In this case, another eigenvalue problem is defined

$$(\mathbf{A}\lambda + \mathbf{B})^T\,\tilde{\boldsymbol{\phi}} = \mathbf{0} \tag{2.43}$$

where $\tilde{\boldsymbol{\phi}}$ is an eigenvector. The eigenvalues of (2.41) and (2.43) are the same, but the eigenvectors are different. The transpose of (2.43) is

$$\tilde{\boldsymbol{\phi}}^T\,(\mathbf{A}\lambda + \mathbf{B}) = \mathbf{0} \tag{2.44}$$

and therefore, $\tilde{\boldsymbol{\phi}}$ is called a *left eigenvector* of the system and correspondingly $\tilde{\boldsymbol{\psi}}$ is called a *right eigenvector*. $\tilde{\boldsymbol{\phi}}$ is of the form

$$\tilde{\boldsymbol{\phi}} = \begin{bmatrix} \boldsymbol{\phi} \\ \boldsymbol{\phi}\lambda \end{bmatrix} \tag{2.45}$$

Assume that λ_i is a solution of (2.41) and λ_j of (2.43). $\tilde{\boldsymbol{\phi}}_i$ and $\tilde{\boldsymbol{\psi}}_j$ are the corresponding left and right eigenvectors. Then

$$(\mathbf{A}\lambda_i + \mathbf{B})\,\tilde{\boldsymbol{\psi}}_i = \mathbf{0} \tag{2.46}$$

and

$$\tilde{\boldsymbol{\phi}}_j^T\,(\mathbf{A}\lambda_j + \mathbf{B}) = \mathbf{0} \tag{2.47}$$

Now premultiply (2.46) with $\tilde{\boldsymbol{\phi}}_j^T$, postmultiply (2.47) with $\tilde{\boldsymbol{\psi}}_i$ and subtract both equations. This results in

$$(\lambda_i - \lambda_j)\, \tilde{\boldsymbol{\phi}}_j^T \mathbf{A} \tilde{\boldsymbol{\psi}}_i = 0 \tag{2.48}$$

For two distinct eigenvalues, this means that

$$\tilde{\boldsymbol{\phi}}_j^T \mathbf{A} \tilde{\boldsymbol{\psi}}_i = 0 \quad ; \quad \lambda_i \neq \lambda_j \tag{2.49}$$

Because the eigenvectors are arbitrarily scaled, the scaling can be chosen such that

$$\tilde{\boldsymbol{\phi}}_i^T \mathbf{A} \tilde{\boldsymbol{\psi}}_i = 1 \tag{2.50}$$

By following the definition in [2] this type of scaling is called *unity modal A scaling*. Now combine the eigenvectors in matrices

$$\tilde{\boldsymbol{\Phi}} = \begin{bmatrix} \tilde{\boldsymbol{\phi}}_1 & \tilde{\boldsymbol{\phi}}_2 & \dots & \tilde{\boldsymbol{\phi}}_n \end{bmatrix} \quad ; \quad \tilde{\boldsymbol{\Psi}} = \begin{bmatrix} \tilde{\boldsymbol{\psi}}_1 & \tilde{\boldsymbol{\psi}}_2 & \dots & \tilde{\boldsymbol{\psi}}_n \end{bmatrix} \tag{2.51}$$

From (2.50) it follows that

$$\tilde{\boldsymbol{\Phi}}^T \mathbf{A} \tilde{\boldsymbol{\Psi}} = \mathbf{I} \tag{2.52}$$

where $\mathbf{I}$ is the identity matrix, and consequently

$$\tilde{\boldsymbol{\Phi}}^T = \tilde{\boldsymbol{\Psi}}^{-1} \mathbf{A}^{-1} \tag{2.53}$$

By combining (2.51) and (2.46) a matrix expression is made

$$\left(\mathbf{A} \tilde{\boldsymbol{\Lambda}} + \mathbf{B} \right) \tilde{\boldsymbol{\Psi}} = 0 \tag{2.54}$$

Where $\tilde{\boldsymbol{\Lambda}}$ is a diagonal matrix containing the eigenvalues. Now premultiply (2.54) with $\tilde{\boldsymbol{\Phi}}^T$

$$\tilde{\boldsymbol{\Phi}}^T \left(\mathbf{A} \tilde{\boldsymbol{\Lambda}} + \mathbf{B} \right) \tilde{\boldsymbol{\Psi}} = 0 \tag{2.55}$$

and consider (2.52)

$$\tilde{\mathbf{\Phi}}^T \mathbf{B} \tilde{\mathbf{\Psi}} = -\tilde{\mathbf{\Lambda}} \tag{2.56}$$

This means that the equations of motion (2.38) can be diagonalized which will be used later on. Although classic modal analysis, with symmetric matrices, is not valid for these kind of systems, this decoupling is very convenient to find similarities between this rotating system and a classic symmetric system.

2.3.3 Frequency response and impulse response

The frequency response of a dynamical system is the transfer function where the Laplace operator $s = j\omega$. The state space representation of (2.37) is

$$\mathbf{A}\dot{\mathbf{z}} + \mathbf{B}\mathbf{z} = \hat{\mathbf{f}} \tag{2.57}$$

where

$$\hat{\mathbf{f}} = \begin{bmatrix} \mathbf{f} \\ \mathbf{0} \end{bmatrix} \tag{2.58}$$

In the Laplace domain

$$(\mathbf{A}s + \mathbf{B})\,\mathbf{Z}(s) = \hat{\mathbf{F}}(s) \tag{2.59}$$

The inverse of the transfer function matrix of this system is defined as

$$\mathbf{A}s + \mathbf{B} = \mathbf{H}^{-1} \tag{2.60}$$

Premultiply this expression by $\tilde{\mathbf{\Phi}}^T$ and postmultiply by $\tilde{\mathbf{\Psi}}$

$$\mathbf{I}s - \tilde{\mathbf{\Lambda}} = \tilde{\mathbf{\Phi}}^T \mathbf{H}^{-1} \tilde{\mathbf{\Psi}} \tag{2.61}$$

and take the inverse of both sides

$$\left(\mathbf{I}s - \tilde{\mathbf{\Lambda}}\right)^{-1} = \tilde{\mathbf{\Psi}}^{-1} \mathbf{H} \left(\tilde{\mathbf{\Phi}}^T\right)^{-1} \tag{2.62}$$

premultiply both sides by $\tilde{\mathbf{\Psi}}$ and postmultiply by $\tilde{\mathbf{\Phi}}^T$ and an expression for $\mathbf{H}$ is formed

$$\mathbf{H} = \tilde{\mathbf{\Psi}} \left(\mathbf{I}s - \tilde{\mathbf{\Lambda}} \right)^{-1} \tilde{\mathbf{\Phi}}^T \tag{2.63}$$

$\mathbf{I}$ is the identity matrix and $\tilde{\mathbf{\Lambda}}$ a diagonal matrix containing the eigenvalues. $\left(\mathbf{I}s - \tilde{\mathbf{\Lambda}} \right)^{-1}$ is thus a diagonal matrix, and the inverse of a diagonal matrix is the reciprocal of each value on the diagonal or

$$\mathbf{H} = \tilde{\mathbf{\Psi}} \begin{bmatrix} \frac{1}{s-\lambda_1} & & & \\ & \frac{1}{s-\lambda_1} & & \\ & & \ddots & \\ & & & \frac{1}{s-\lambda_{2n}} \end{bmatrix} \tilde{\mathbf{\Phi}}^T \tag{2.64}$$

One element of this matrix is thus

$$H_{ij}(i\omega) = \sum_{r=1}^{2n} \frac{\tilde{\psi}_{ir} \tilde{\phi}_{jr}}{i\omega - \lambda_r} \tag{2.65}$$

Where s is replaced by $j\omega$. The eigenvalues of the system come in conjugate pairs. Within this research, the interest lies in the frequency response between force and displacement or the receptance. Because of (2.42) and (2.45) the frequency response for a rotating system between a force at location p and a displacement at location q is [38]

$$H_{pq}(i\omega) = \sum_{r=1}^{N} \frac{\psi_{pr}\phi_{qr}}{i\omega - \lambda_r} + \frac{\overline{\psi}_{pr}\overline{\phi}_{qr}}{i\omega - \overline{\lambda}_r} \tag{2.66}$$

and the impulse response

$$h_{pq}(t) = \sum_{r=1}^{N} \psi_{pr}\phi_{qr} e^{-\lambda_r t} + \overline{\psi}_{pr}\overline{\phi}_{qr} e^{-\overline{\lambda_r} t} \tag{2.67}$$

When the eigenvalues, and both left and right eigenvectors of the system are known, the frequency response and the impulse response can be calculated. Vice versa, the frequency response and the impulse response contain information about the eigenvalues and the left and right eigenvectors. Although solving the left and right eigenvalue problem is easy to overcome, there are some practical limitations, especially for experimental validation. Because the frequency response (2.66) contains both left and right eigenvectors, the frequency response matrix is not symmetric. This means that Maxwell's reciprocity does not hold and can not be used

for validation purposes. Also, in order to extract left and right eigenvectors from (2.66), minimum one row and one column of the frequency response function matrix have to be known [38].

2.4 Conclusion

This introductory chapter provides some important fundamentals to understand instability of rotating systems caused by rotating damping. Existing literature is combined into a clear overview of rotating damping, how it behaves and how it is implemented in a finite element model. The focus is on lateral vibrations and the fact that instability is a free vibration phenomenon. This has an important impact on measurements that are made for validation purposes. Terms as rotor spin and free whirl are explained and will later on be used in both simulations and measurements. A special effort is made towards the understanding of the nature of rotating damping, and the follower force caused by the stress-strain relation in the material. There are other phenomena that cause rotating damping such as friction in shrink fits, couplings and even magnetic forces but all can be interpreted similarly. The linear speed dependent model that is proposed in this chapter will be used later on for simulation purposes. The real behaviour of a rotating system is not linear which is one of the main reasons for differences between simulations and actual measurements. However, under the assumption of small vibrations, the similarities are acceptable. In the section on modal analysis it is seen that the dynamics of the system are captured in the eigenvalues and in both left and right eigenvectors. The existence of left eigenvectors is the major difficulty in the study of rotating systems. In the following chapters, procedures to overcome this difficulty are proposed.

3 Experimental setups

3.1 Introduction

Experimental validation of theoretical foundings is an important contribution of this research. Therefore, within this research, two practical setups that are specifically designed for this purpose are presented. One of them is the rotating damping setup. This test bench has a design dedicated towards the development of an experimental procedure to predict the stability threshold speed. It is characterized by its simplicity, an approximation of a rotating clamped beam and the ability of a controlled excitation technique by means of an automated impact hammer. The gyroscopic effect is small, but a disk can be added to control this. It is also discussed how the errors on the measurements can be minimized. The second setup is a four degree of freedom torsional vibration setup. It contains a long thin shaft with a negligible mass compared to the four disks that are attached. Therefore, it is easily modelled as a lumped parameter system and the model has a high correspondence to the actual behaviour. The main purpose of the torsional vibration setup is to validate the damping matrix estimation methods that are presented in the chapter 6 and 7.

3.2 The rotating damping setup

A schematic representation of the rotating damping setup is shown in Figure 3.1. This representation shows the mechanical and electrical details of the test bench.

A picture is shown in Figure 3.2. This section is meant to clarify the components that are chosen in the design of this test bench.

3.2.1 The rotating clamped beam effect

The aim is to construct a setup on which experimental modal analysis is applied to validate rotating damping and the stability of the rotor. By combining a finite element model with measurements, a linear model of the rotor is extracted and updated. Because of the focus on the rotating damping, other effects caused by rotation are minimized through well-considered design choices. As already stated in chapter 1, instability caused by rotating damping is a free vibration phenomenon. Therefore, external forces are avoided. The gyroscopic effect is kept low such that only the rotating damping changes as a function of the spin speed. Also, unwanted dynamic effects of the motor are minimized by choosing a proper alignment and coupling. The theoretical concept of a rotating clamped beam in Figure 3.3 is an optimal design for this purpose. In the case of ideal clamping, the behaviour of the beam is decoupled from foundation, the motor and the coupling. The dynamic behaviour of the rotor is only determined by the part of the rotor in between the clamping. Also, because there is no motion in the clamped part of the rotor, there is also no damping present. This means that for ideal clamping, nonrotating damping disappears. Because it is a plain shaft, the only damping present in the rotor is due to the internal friction in the material.

Another major advantage of a clamped rotating beam is that the undamped natural frequencies and mode shapes are easily calculated from beam theory [39]. The shaft is a linear elastic continuum and the undamped natural frequencies are calculated as

$$\omega_n = A\sqrt{\frac{EI}{\mu L^4}} \tag{3.1}$$

With ω_n a natural pulsation in rad/s, E the Young modulus of the material, I the area moment of inertia of the cross section, μ the mass per unit length and l the length. A is a constant that depends on the boundary conditions. For a beam clamped at both sides, the values of A for the first five natural frequencies are shown in Table 3.1 [40]. A comparison is made with the factors for pinned at both sides, because perfect clamping is practically impossible. Because the shaft is a continuum, the number of natural frequencies is infinite. The corresponding undamped mode shapes are shown in Figure 3.4.

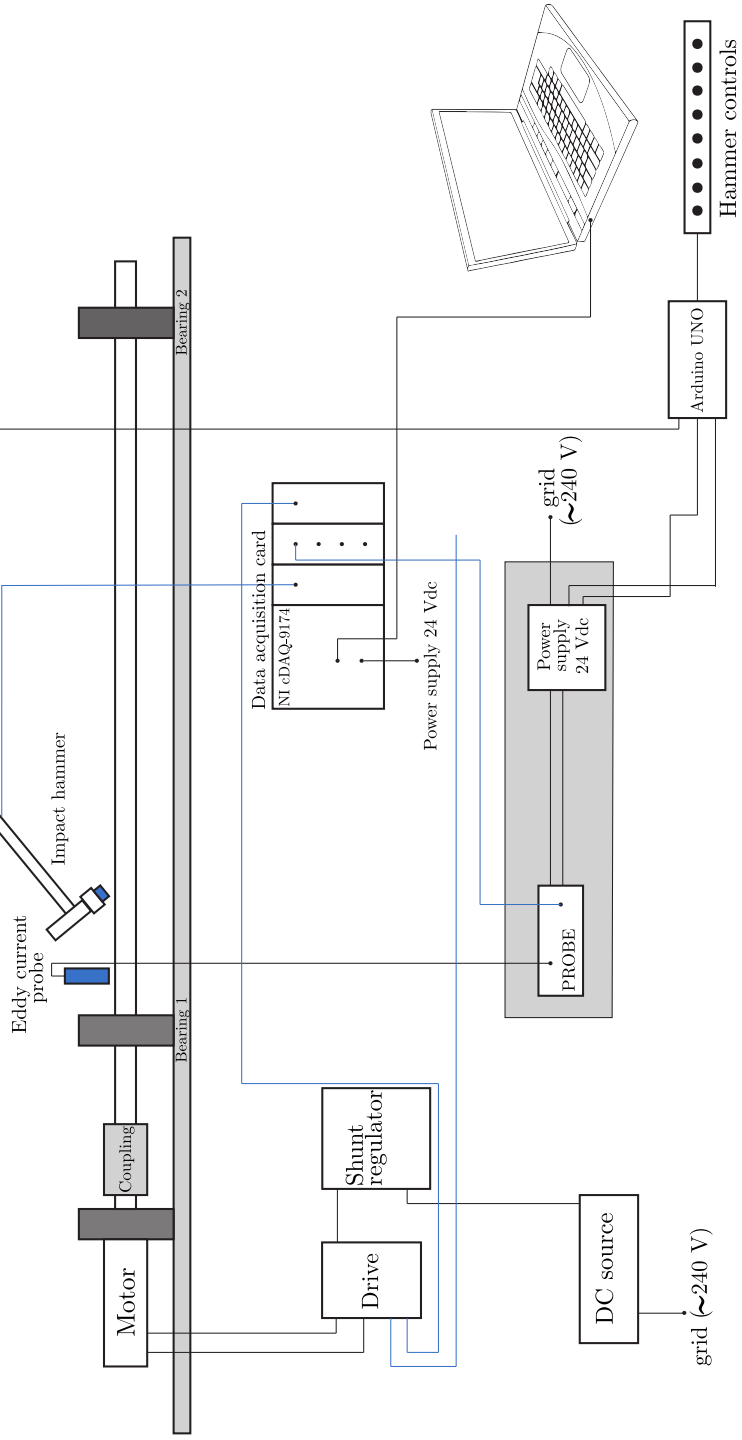

Figure 3.1: Schematic representation of the rotating damping setup including both mechanics and electrical controls

Figure 3.2: Picture of the rotating damping setup

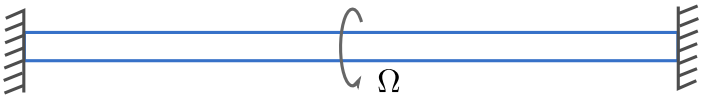

Figure 3.3: A rotating clamped beam

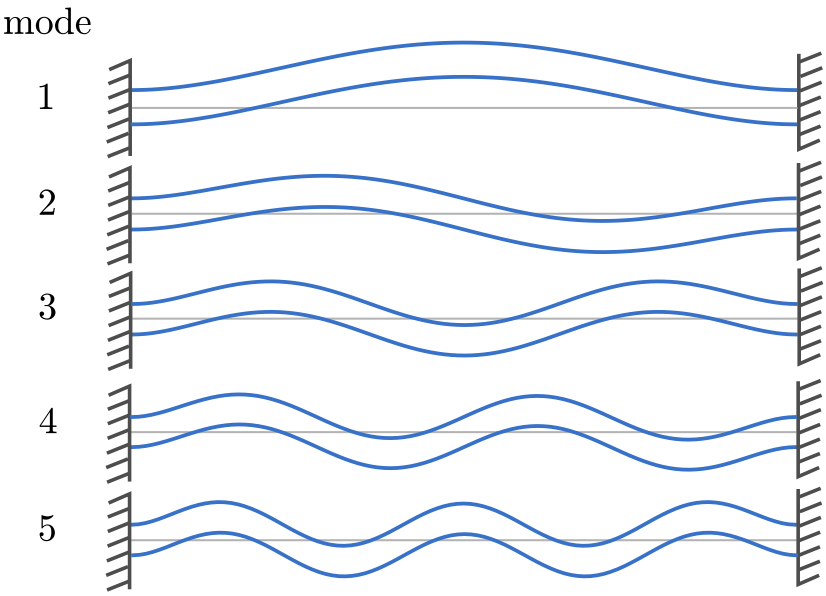

Figure 3.4: First five mode shapes of a clamped beam

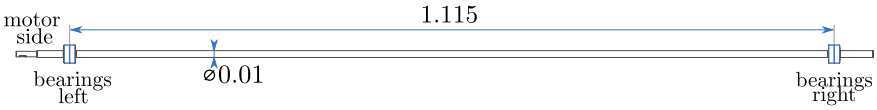

Figure 3.5: The shaft

clamped	22.4	61.7	121	200	289
pinned	9.87	39.5	88.9	158	247

Table 3.1: Values of the constant A for a beam clamped and pinned at both sides in equation (3.1)

3.2.2 Design of the rotating damping setup

3.2.2.1 The rotor, bearings, coupling and disk

A solid CF53 steel shaft is chosen as a rotor. The shaft is induction hardened and precision ground. This type of shafts is generally used for linear motion (inner race for ball bushing bearings) and are therefore manufactured to extremely close tolerances for surface finish, roundness, hardness and straightness. The hardness is HRC 60-64 (Rockwell scale) and the diameter tolerance is h6 (ISO 286). Because of this high precision, the residual unbalance of the shaft is low, when mounted with care. The only unavoidable factor is shaft bow, due to gravity. The shaft has a diameter of 0.01 m and the length between the middle of the bearings is 1.115 m (Figure 3.5).

The bearings in this setup serve as boundary conditions. For clamping, this means that the bearings still have to allow axial rotation but neither translation, nor tilting. This boundary condition is hard to accomplish by bearings, but by using high precision angular contact spindle bearings, the result is optimized. The bearings used in this setup are FAG B7000-E-2RSD-T-P4S-UL bearings with a contact angle of 25°. They are mounted back-to-back to maximize the lateral rotational stiffness. The housing is made of massive blocks and the outer rings are tightened together as seen in Figure 3.6. The resulting boundary conditions are in between clamping and pinning as it will be shown in the measurements later on. The theoretical first five frequencies are calculated by using equation (3.1) and Table 3.1 and Table 3.2 report the results.

Because the boundary conditions are not ideal, the coupling with the motor also plays an important role in the dynamic behaviour. It serves as a coupling of the wanted motion (rotor spin) and decoupling of the motor vibrations and the rotor itself. The Rotex GS14 is used for this purpose (Figure 3.7). This is a jaw-type coupling which is backlash-free. The flexible material in between the two steel

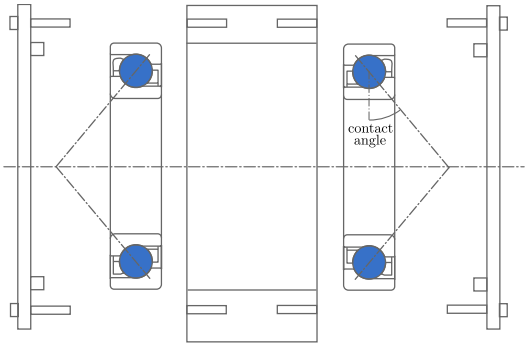

Figure 3.6: Mounting of the bearings in the housing

	pinned			clamped		
mode	rad/s	Hz	rpm	rad/s	Hz	rpm
1	102.7	16.4	980.9	233.1	37.1	2226.2
2	411.1	65.4	3925.6	642.1	102.2	6131.9
3	925.2	147.3	8835.2	1259.2	200.4	12025.3
4	1644.4	261.7	15702.6	2081.5	331.3	19876.6
5	2570.6	409.1	24547.7	3101.4	493.6	29616.2

Table 3.2: Comparison between the undamped natural frequency of the clamped rotor and the pinned rotor

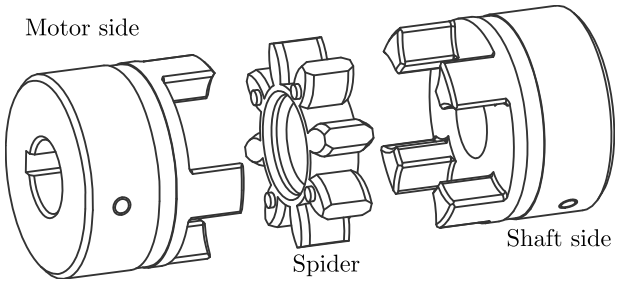

Figure 3.7: Drawing of used coupling Rotex GS14

parts is called the spider and is both vibration-reducing and electrically insulating. A disk can also be attached to the shaft. The aluminium disk that is used, has a thickness of 0.015m and a diameter of 0.15 m both enhances the kinetic energy and influences the gyroscopic effect.

3.2.2.2 Alignment

In order to minimize external forces, the alignment between both bearing housings needs to be accurate. This is mainly because the clamping is in practice not ideal. A first strategy is to design a setup which is easy to align accurately. This is for instance accomplished by a moveable base plate where the displacement is adjustable by a bolt-nut arrangement. This strategy is used by Patel in [41] or by Nakhaeinejad in [42]. The initial alignment is done with laserequipment or with a dial indicator on a bracket. An advantage of this strategy is that the alignment is variable between different measurements, but a disadvantage is that an accurate alignment procedure is needed for every measurement which is time consuming. A second strategy is to mount motor and bearings on a foundation with a high precision. High precision foundations are typically used in length measuring equipment. For the purpose of the rotating damping setup, a chassis of a Carl Zeiss Jena length measuring bench is used. By doing this, the alignment is optimal from the beginning but not variable. The small residual misalignment that is present remains constant for every measurement.

3.2.2.3 The motor

The dimensioning of the motor is mainly based upon the speed range. As is already mentioned in chapter 1, instability due to rotating damping appears at operating speed higher than the first critical speed. By taking Table 3.2 into account the speed range is determined. In worst case, with ideal clamping, the first critical speed is 2226 rpm and the second critical speed is 6131 rpm. With a motor within a speed range of 7000 rpm it is possible to go through these two critical speeds.

Figure 3.8: The EC 60 60 mm, brushless, 400 Watt motor with Hall sensors

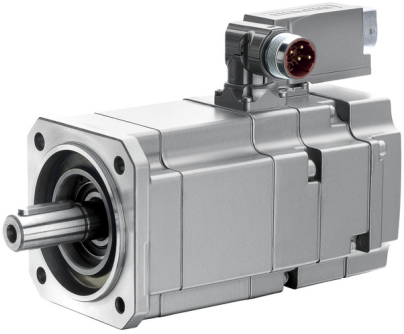

Figure 3.9: Siemens 1FK7042-5AK71-1UG0 permanent magnet synchronous motor

The torque of the motor is of minor importance as the only torque that has to be overcome is the friction in the bearings and the acceleration of the shaft. The latter is even of minor importance because the measurements are done at constant speed. The first motor that is chosen is a Maxon Motor EC 60 60 mm, brushless DC motor, 400 Watt, with Hall sensors and is especially chosen for the high speed range with a maximum speed of 7000 rpm. The motor is compact and easy to control. The main disadvantage of the Hall sensors is that the speed range only starts from 1000 rpm. As drive, the DEC 70/10 is used This light motor has a minimal influence on the measurements. When the disk is added, the Maxon Motor is not sufficient. Therefore, the measurements with the disk are done with a Siemens 1FK7042-5AK71-1UG0. This is a permanent magnet synchronous motor with encoder feedback. The main drawback of this motor is the larger coupling resulting in higher influence on the measurements.

3.2.3 Excitation and response measurement

3.2.3.1 Excitation of a rotating shaft

Experimental modal analysis relies on the measurement of the frequency response functions. This means that the structure has to be excited by means of a force. Two commonly used techniques are hammer impacts and electrodynamic shakers [2] [34]. Although there are several advantages of electrodynamic shakers, e.g. the force range and type of excitation signals, this technique is difficult to apply on a rotating shaft. For the proper installation of a shaker, there are several difficulties to account for [43] and some experience is advised. Because a shaker needs contact for excitation, an auxiliary bearing is needed on the rotor [38]. This auxiliary bearing adds mass, stiffness and damping to the rotor, which should be excluded in this setup. There exist some noncontact techniques that are studied in the literature: laser [44], pressurized air [45] [46], acoustics [47], and active magnetic bearings [48]. Generally, these techniques are still unreliable or require a considerable amount of knowledge to operate. The excitation techniques are compared in Table 3.4.

Excitation technique	Contact/noncontact	Force range [N]	Excitation signal	Repeatability
Electrodynamic shaker	contact	8-1800	arbitrary	fair
Hammer	contact	5-45000	impact	poor
Laser	noncontact	$< 5 \times 10^{-4}$	arbitrary	fair
Pressurized air	noncontact	$< 0{,}6$	impact	fair
Acoustics	noncontact	$< 5 \times 10^{-2}$	arbitrary	fair
Magnetic bearings	noncontact	0-7000	arbitrary	fair

Table 3.4: Comparison of state-of-the-art excitation techniques

Within the context of this thesis, the hammer impact is chosen as an excitation technique due to it's simplicity. Although being a contact method, the impact time is very low and thus this technique is applicable on a rotating shaft. The disadvantages of hammer impacts are mainly the repeatability (of both force and excitation point), the high crest factor of the excitation signal and the low signal to noise ratio of the decaying response. These last two disadvantages are dealt with trough proper signal processing [2]. The repeatability of the hammer is improved by automating the hammer impact. The principle is seen in Figure 3.10. A regular impact hammer, the Dytran 5800B2T, is connected to a stepping motor. The angle θ is proportional to the impact force. The stepping motor can control the initial angle. By doing this, both force and impact location are controlled.

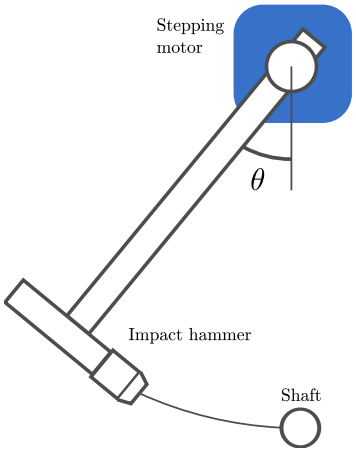

Figure 3.10: Automated impact hammer principle

3.2.3.2 Response measurement of a rotating shaft

The response is measured by proximity probes or eddy current probes. This type of transducer measures displacement by electromagnetic inductance. This is a robust and reliable sensor that is widely used in rotordynamics [15]. The working principle is shown in Figure 3.11. The probe itself is a coil which is driven with an alternating current of 1 up to 1.5 MHz. When the gap is small, some of the magnetic energy in the probe is absorbed by eddy currents in the shaft. The carrier is consequently attenuated by the size of the gap. A demodulator converts the modulated signal into a DC voltage that is proportional to the gap. If the shaft is vibrating, the output voltage is a measure for the displacement of the shaft. The electromagnetic character of the eddy current probes causes the measured displacement to be superimposed with circumferential variations in shaft surface conditions as well as electrical conductivity and permeability variations just below the shaft surface [1]. The noise on the response signal is thus significantly higher than for instance with an accelerometer. The eddy current probe system that is used on the setup is a Monitran MTN/EP200 and is especially chosen for the large operating gap (5 mm).

3.2.4 Minimization of errors

Experimental modal analysis is based upon the measurements of the frequency response functions. For a linear time-invariant system, the frequency response is the ratio between the output and input, both in frequency domain

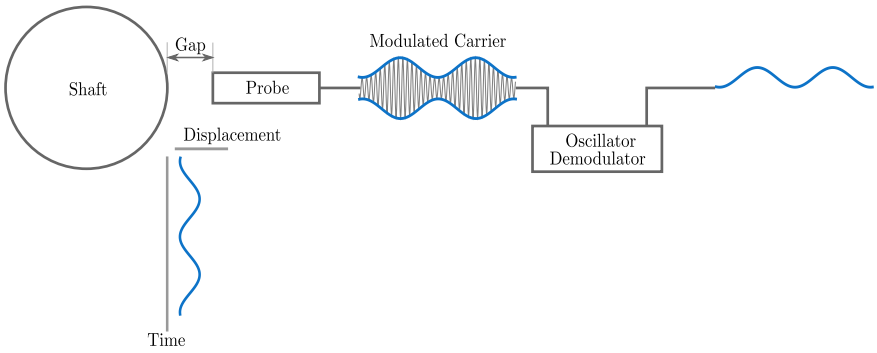

Figure 3.11: Principle of eddy current probes [1]

$$H(f) = \frac{Y(f)}{X(f)} \tag{3.2}$$

where $H(f)$ is the frequency response, $Y(f)$ is het output and $X(f)$ is the input. There are several methods to extract the frequency response function from measured data and the differences between them is beyond the scope of this thesis. Typically, the H_1 *estimator* is used when there is noise on the output.

$$\hat{H}_1(f) = \frac{\hat{G}_{yx}}{\hat{G}_{xx}} \tag{3.3}$$

where $\hat{}$ denotes an estimate, $\hat{G}_{yx}$ the cross-spectral density between out- and input and $\hat{G}_{xx}$ the auto-spectral density of the input. This type of estimator assumes that the noise on the input is negligible. In practise, H_1 always contains errors. Basically, the errors are subdivided into *bias errors* and *random errors*. A detailed description of how to deal with both errors is given in [2]. In short, the bias error is reduced by increasing the measurement time and the random error is reduced by increasing the number of measurements. This both results in a long measurement time. Figure 3.12 is a graph that shows the maximum normalized bias error, ϵ_b as a function of the ratio between *the bandwidth* and the *frequency increment*, $B_r/\Delta f$ [2]. The bandwidth, for a single degree of freedom system is defined as $2\zeta_r f_r$ where ζ_r is the relative damping and f_r the resonance frequency. The bias error is mimized by lowering the ratio $B_r/\Delta f$. At low resonance frequencies and low relative damping, this can only be compensated by a higher frequency increment which is defined by the measurement time.

To perform the experimental modal analysis, five measurement locations are chosen on the shaft (Figure 3.13). This allows to extract the first five modes.

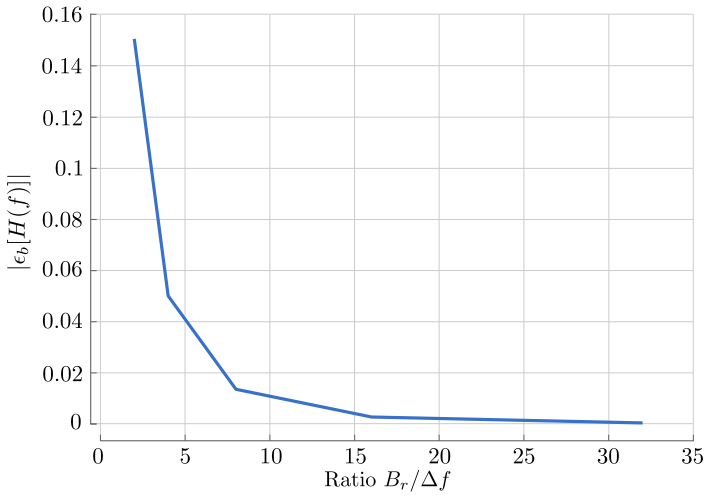

Figure 3.12: Maximum bias error ϵ_b on a frequency response of a single degree of freedom system as a function of the ratio between the bandwidth B_r and the frequency increment Δf [2]

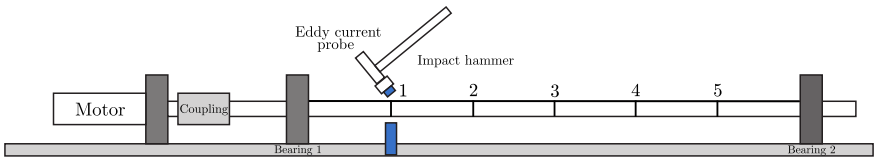

Figure 3.13: Schematic representation of the measurement locations

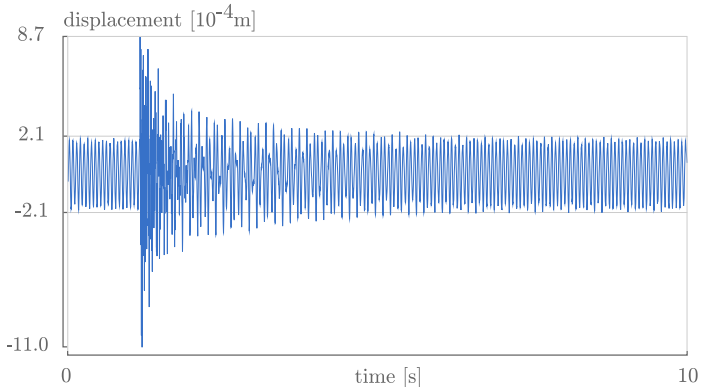

Figure 3.14: The response at rotor location 1 operated at 1000 rpm and excited by the hammer, unbalance and rotor bow

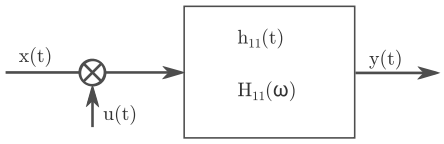

Figure 3.15: The response, x(t), is due to the excitation of the hammer, f(t), and unbalance combined with rotor bow, u(t).

Experimental modal analysis can thus be performed at several speeds. By chosing the right measurement time, the results are optimized.

Figure 3.14 shows a reponse of the shaft to a hammer impact at location 1. The shaft is rotating at 1000 rpm and the sample frequency is 2048 Hz. The response is measured at the *driving point*, location 1, or at the same point that was excited (here at 0.2 m from the left bearing). It is clearly visible that the shaft already has some response before the impact. This is because of the shafts residual unbalance and rotor bow. Apparently, the shaft is excited by both the hammer, and the unbalance and rotor bow (Figure 3.15). At the moment of the impact, several frequencies are excited. After a few seconds, the transient response gets masked by the unbalance response. The presence of this steady state phenomenon on the response is a particular difficulty which has to be accounted for and is discussed later on.

Because the response is the result of both an impact excitation and unbalance/rotor bow, an additional error is made upon the frequency response estimation. The H_1 estimator results in

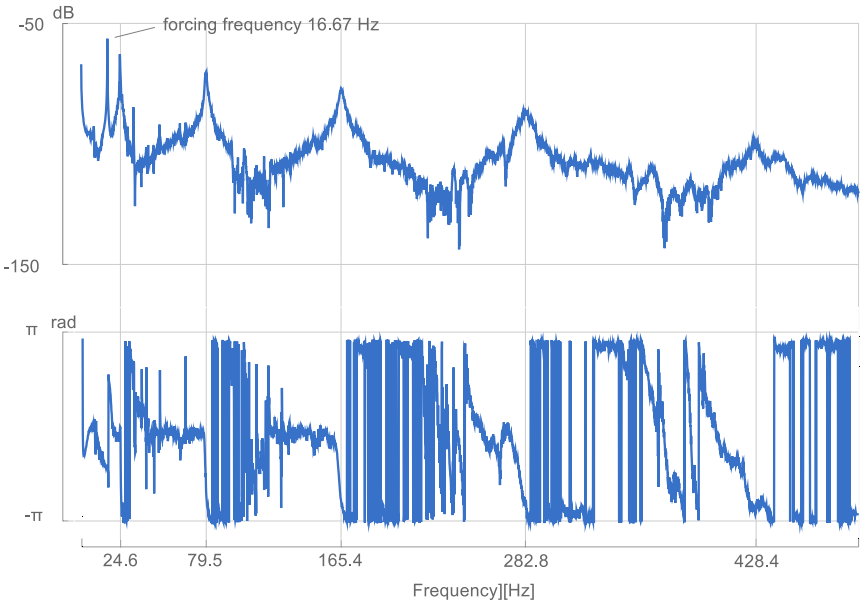

Figure 3.16: Frequency response of a measurement at the driving point of the rotor while rotating at 1000 rpm.

$$\hat{H}_1 = \frac{\hat{G}_{y(x+u)}(f)}{\hat{G}_{xx}(f)} \quad \text{or} \quad \hat{H}_1 = \frac{\hat{G}_{yx}(f)}{\hat{G}_{xx}(f)} + \frac{\hat{G}_{yu}(f)}{\hat{G}_{xx}(f)} \tag{3.4}$$

where $\hat{G}_{xx}$ is the auto-spectrum density of only the hammer, and $\hat{G}_{y(x+u)}(f)$ the cross-spectral density of the input and the output corrupted by the unbalance/rotor bow. If the frequencies of unbalance/rotor bow are far away from the peak of interest, the influence is low. A result of a frequency response at driving point (0.2m from the left bearing) while rotating at 1000 rpm is shown in Figure 3.16.

3.3 The torsional vibration setup

Here, a second setup is introduced, not designed within this research but merely used as a reference for multiple degree of freedom models. The torsional vibration setup is a four degree of freedom torsional system which is especially designed to be modelled and measured easily. It contains a motor, a long, thin shaft and four disks. The mass of the shaft is negligible with respect to the disks and therefore easily represented as a discrete four degree of freedom system. Five sensors

are used to measure the angular displacement of the motor and the disks. The angular motor displacement is measured by a built-in resolver. The angular displacement of each disk is measured by an analog encoder connected by a stiff belt-transmission to the shaft with a ratio of 1/2. The schematic representation of the discrete theoretical model is shown in Figure 3.17(a). The as-built drawing and a picture are shown in Figure 3.17(b) and Figure 3.17(c). More details can be found in [49].

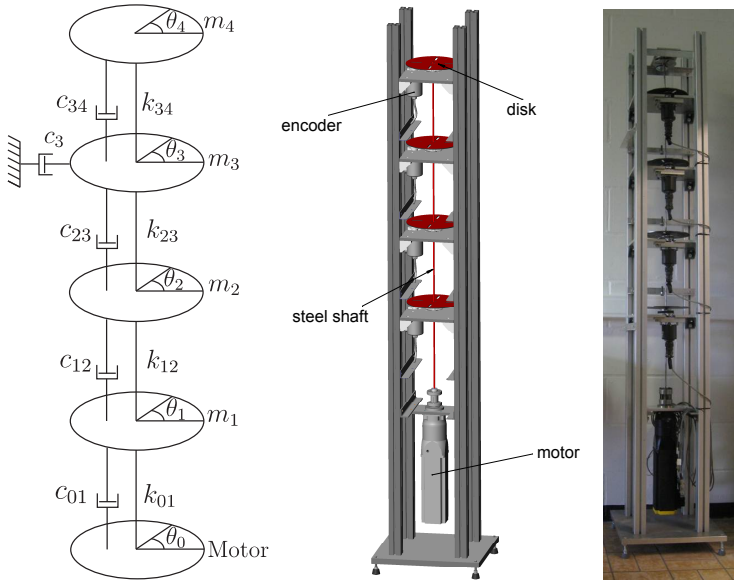

(a) Model (b) Asbuilt drawing (c) Picture

Figure 3.17: The torsional vibration setup

3.3.1 Theoretical model

The system, as presented in [49] has four rotational degrees of freedom. A linear, time invariant model is used to describe its dynamic behaviour.

$$\mathbf{M}\ddot{\boldsymbol{\theta}} + \mathbf{C}\dot{\boldsymbol{\theta}} + \mathbf{K}\boldsymbol{\theta} = \mathbf{T} \tag{3.5}$$

$\boldsymbol{\theta} = [\theta_1\ \theta_2\ \theta_3\ \theta_4]^T$ is the vector of generalized coordinates each denoting the absolute angular displacement. The mass matrix, $\mathbf{M}$, contains the inertia of the disks increased with the remaining inertia added by the belt and pulleys. The stiffness matrix, $\mathbf{K}$, contains the torsional stiffnesses of the steel shaft. Because

the motor is connected to the first disk, there is a so called base excitation. Taking a look at θ_1, the equation of motion is

$$m_1\ddot{\theta}_1 + (c_1 + c_{01})\,\dot{\theta}_1 + (k_{01} + k_{12})\,\theta_1 - c_{12}\dot{\theta}_2 - k_{12}\theta_2 = c_{01}\dot{\theta}_0 + k_{01}\theta_0 \quad (3.6)$$

Leading to a torque $\mathbf{T} = \begin{bmatrix} c_{01}\dot{\theta}_0 + k_{01}\theta_0 & 0 & 0 & 0 \end{bmatrix}^T$. The mass, damping and stiffness matrices **M**, **C** and **K** are

$$\mathbf{M} = \begin{bmatrix} m_1 & 0 & 0 & 0 \\ 0 & m_2 & 0 & 0 \\ 0 & 0 & m_3 & 0 \\ 0 & 0 & 0 & m_4 \end{bmatrix} \quad (3.7)$$

$$\mathbf{C} = \begin{bmatrix} c_1 + c_{01} + c_{12} & -c_{12} & 0 & 0 \\ -c_{12} & c_2 + c_{12} + c_{23} & -c_{23} & 0 \\ 0 & -c_{23} & c_3 + c_{23} + c_{34} & -c_{34} \\ 0 & 0 & -c_{34} & c_4 + c_{34} \end{bmatrix}, \quad (3.8)$$

$$\mathbf{K} = \begin{bmatrix} k_{01} + k_{12} & -k_{12} & 0 & 0 \\ -k_{12} & k_{12} + k_{23} & -k_{23} & 0 \\ 0 & -k_{23} & k_{23} + k_{34} & -k_{34} \\ 0 & 0 & -k_{34} & k_{34} \end{bmatrix} \quad (3.9)$$

The torsional stiffness of the spring steel shaft is given by

$$k_{ij} = \frac{\pi G}{32 L_{ij}} d^4 \quad (3.10)$$

with G the shear modulus, d the diameter of the spring steel shaft and L_{ij} the length of the shaft in between disks i and j. The damping is arbitrary. In this research, the damping matrix is taken proportional to the stiffness matrix with a factor of 5.5×10^{-5}. The damping is chosen with a trial and error procedure to approximate the measurements. In the measurement, the extra damping is added on the third disk by friction. Therefore, the dampers c_1, c_2 and c_4 are taken zero and c_3 is $7 \times 10^{-2} Ns/m$. Because there is no preliminary knowledge on the damping, these damping parameters are the result of a trial and error procedure and are adjusted to fit the measurements. The values of inertia and stiffness are depicted in Table 3.5 and the calculated undamped natural frequencies in Table 3.6.

3.3.2 Excitation and response measurements

As already described, the setup is a four degree of freedom system with base excitation. This means that the motor is easily used as an excitation. The measured angular displacement is linked to the external torque by

Parameter	Value
m_{1-4}	3.5×10^{-3} *kgm*^{2}
k_{01}	35.57 *N/m*
k_{12}	35.09 *N/m*
k_{23}	35.45 *N/m*
k_{34}	34.80 *N/m*

Table 3.5: Values used in experiments

Natural frequency	Value *[Hz]*
f_1	5.56
f_2	15.99
f_3	24.43
f_4	30.03

Table 3.6: Calculated undamped natural frequencies

$$\mathbf{T} = \begin{bmatrix} c_{01}\dot{\theta}_0 + k_{01}\theta_0 & 0 & 0 & 0 \end{bmatrix}^T \tag{3.11}$$

As an excitation signal, a stepped sine is used. This type of excitation is easy to implemented on a motor. An example of an excitation signal of the motor and the response of the first disk is shown in Figure 3.18.

3.4 Conclusion

In this chapter, the rotating damping setup is discussed in detail. The most important contribution is the design of a setup that allows to focus on rotating damping by minimizing all other effects. This is achieved by imitating a clamped rotating beam with accurate alignment and careful component selection such as bearings and coupling. Measuring while rotating entails a lot of difficulties. Excitation and response measurements are different than in a classic experimental modal analysis. Therefore, as an excitation, an automated impact hammer is proposed to enhance the repeatability. The errors in the measurements can be avoided by increasing the measurement time. Small damping results in a high and narrow peak. The measurement time needs to be tuned accordingly. A second setup that is presented is the torsional vibration setup. This setup is used especially for the validation of the damping measurements that are presented in chapter 6 and 7. The setup is easy to model and validate.

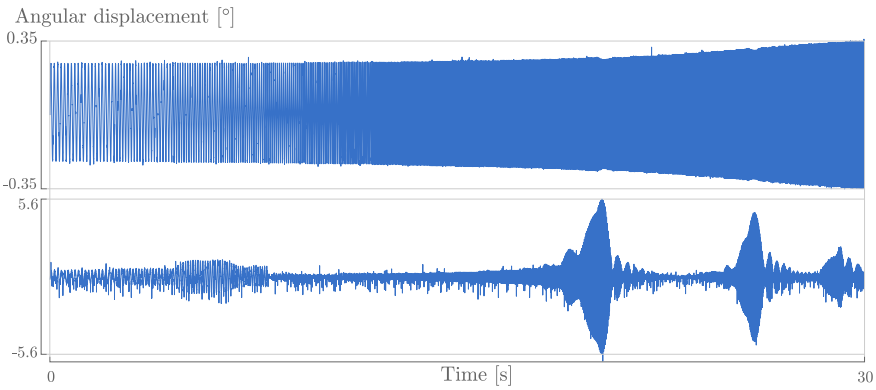

Figure 3.18: Excitation signal of the motor and response of the first disk in the torsional vibration setup

4 The modal model

4.1 Introduction

In chapter 2, the linear speed dependent model and its matrices have been discussed in detail. The speed dependency and the asymmetry of the model need specific attention when dealing with experiments. A detailed model generally implies an advanced measurement procedure which is usually time consuming. From an industrial point of view, measurement procedures have to be simple and transparent. If the model is too complex to be experimentally validated, a simplification is needed. These simplifications are based upon assumptions and observations. Generally, literature uses the Jeffcott rotor to describe the physical behaviour of rotating machinery [50] [1] [30]. The Jeffcott rotor, first introduced by Henry Homan Jeffcott in 1919 [51], describes the rotor in two degrees of freedom, x and y. It does not contain gyroscopic effects, nor rotating damping. Moreover, the direct link between the multiple degree of freedom model and the Jeffcott rotor is not clear. Therefore, in this research, the multiple degree of freedom system is used as a starting point and decoupled into the modal model. The modal model is a more realistic representation than Jeffcott rotor and describes the behaviour of the rotor in one single mode. This unique representation contains both gyroscopic effect and rotating damping. Although the modal mass, stiffness and damping in this model are complex valued, it is shown that, in the case of light damping, this can be highly simplified. This leads to a straightforward expression of the decay rate and the stability threshold speed.

4.2 Decoupling the multiple degree of freedom model

4.2.1 The modal model

The linear speed dependent model, in the case of free vibration, is written as

$$\mathbf{M}\ddot{\mathbf{q}} + (\mathbf{C}_n + \mathbf{C}_{rs} + \Omega\mathbf{G})\,\dot{\mathbf{q}} + (\mathbf{K} + \Omega\mathbf{C}_{rss})\,\mathbf{q} = \mathbf{0} \quad \text{with} \quad \mathbf{q}, \mathbf{0} \in \mathbb{R}^{n\times 1} \tag{4.1}$$

And in state space as

$$\mathbf{A}\dot{\mathbf{z}} + \mathbf{B}\mathbf{z} = \mathbf{0} \quad \text{with} \quad \mathbf{z}, \mathbf{0} \in \mathbb{R}^{2n\times 1} \tag{4.2}$$

compared to chapter 2, **A**, **B** and **z** are chosen differently:

$$\mathbf{A} = \begin{bmatrix} \mathbf{M} & \mathbf{0} \\ \mathbf{0} & \mathbf{K} + \Omega\mathbf{C}_{rss} \end{bmatrix} \quad ; \quad \mathbf{B} = \begin{bmatrix} \mathbf{C}_n + \mathbf{C}_{rs} + \Omega\mathbf{G} & \mathbf{K} + \Omega\mathbf{C}_{rss} \\ -(\mathbf{K} + \Omega\mathbf{C}_{rss}) & \mathbf{0} \end{bmatrix} \quad ; \quad \mathbf{z} = \begin{bmatrix} \dot{\mathbf{q}} \\ \mathbf{q} \end{bmatrix} \tag{4.3}$$

For a single mode, i, the left and right eigenvalue problem is written as

$$\tilde{\boldsymbol{\phi}}_i^T (\mathbf{A}\lambda_i + \mathbf{B}) = 0 \tag{4.4}$$

$$(\mathbf{A}\lambda_i + \mathbf{B})\,\tilde{\boldsymbol{\psi}}_i = 0 \tag{4.5}$$

and

$$\tilde{\boldsymbol{\phi}}_i = \begin{bmatrix} \lambda_i\boldsymbol{\phi}_i \\ \boldsymbol{\phi}_i \end{bmatrix}; \qquad \tilde{\boldsymbol{\psi}}_i = \begin{bmatrix} \lambda_i\boldsymbol{\psi}_i \\ \boldsymbol{\psi}_i \end{bmatrix} \tag{4.6}$$

premultiplying (4.5) this by the transpose of the left eigenvector $\tilde{\boldsymbol{\phi}}_i^T$ results in

$$\begin{bmatrix} \lambda_i\boldsymbol{\phi} \\ \boldsymbol{\phi}_i \end{bmatrix}^T \left(\begin{bmatrix} \mathbf{M} & \mathbf{0} \\ \mathbf{0} & \mathbf{K} + \Omega\mathbf{C}_{rss} \end{bmatrix} \lambda_i + \begin{bmatrix} \mathbf{C}_n + \mathbf{C}_{rs} + \Omega\mathbf{G} & \mathbf{K} + \Omega\mathbf{C}_{rss} \\ -(\mathbf{K} + \Omega\mathbf{C}_{rss}) & \mathbf{0} \end{bmatrix} \right) \begin{bmatrix} \lambda_i\boldsymbol{\psi}_i \\ \boldsymbol{\psi}_i \end{bmatrix} = 0 \tag{4.7}$$

This yields a characteristic equation:

$$\hat{m}_i\lambda_i^2 + (\hat{c}_{ni} + \hat{c}_{rsi} + \Omega\hat{g}_i)\,\lambda_i + \hat{k}_i + \Omega\hat{c}_{rssi} = 0 \tag{4.8}$$

with

$$\hat{m}_i = \boldsymbol{\phi}_i^T \mathbf{M} \boldsymbol{\psi}_i \tag{4.9}$$

$$\hat{c}_{ni} + \hat{c}_{rsi} = \boldsymbol{\phi}_i^T \left(\mathbf{C}_n + \mathbf{C}_r \right) \boldsymbol{\psi}_i \tag{4.10}$$

$$\hat{g}_i = \boldsymbol{\phi}_i^T \mathbf{G} \boldsymbol{\psi}_i \tag{4.11}$$

$$\hat{k}_i = \boldsymbol{\phi}_i^T \mathbf{K} \boldsymbol{\psi}_i \tag{4.12}$$

$$\hat{c}_{rssi} = \boldsymbol{\phi}_i^T \mathbf{C}_r \boldsymbol{\psi}_i \tag{4.13}$$

$\hat{\cdot}$ means that these are modal parameters, and not physical. $\hat{m}_i$ is the modal mass, $\hat{c}_{ni} + \hat{c}_{rsi} + \Omega \hat{g}_i$ is the modal damping and $\hat{k}_i + \Omega \hat{c}_{rssi}$ is the modal stiffness. Equation (4.8) is called *the modal model*. In this general representation of the matrices, there is no obvious relation between the left and right eigenvectors. Moreover, because the eigenvectors are complex valued and scaled arbitrary, the modal parameters are also complex valued and scaled arbitrary. When stability is concerned, the main interest is the real part of the poles. Due to the complex parameters in (4.8), a representation of the real and imaginary parts of the poles is not straightforward. In the following, the eigenvectors are discussed and a perturbation analysis is used to gain insight into the modal parameters.

4.2.2 Relation between left and right eigenvectors

The left and right eigenvectors are related as follows

$$\left(\mathbf{A} \lambda_i + \mathbf{B} \right) \tilde{\boldsymbol{\psi}}_i = \mathbf{0} \tag{4.14}$$

$$\left(\mathbf{A} \lambda_i + \mathbf{B} \right)^T \tilde{\boldsymbol{\phi}}_i = \mathbf{0} \tag{4.15}$$

Due to the choice of the coordinates in (2.5), the eigenvectors can be written in x and y direction

$$\begin{bmatrix} \boldsymbol{\phi}_i \\ \lambda_i \boldsymbol{\phi}_i \end{bmatrix} = \begin{bmatrix} \boldsymbol{\phi}_{ix} \\ \boldsymbol{\phi}_{iy} \\ \lambda_i \boldsymbol{\phi}_{ix} \\ \lambda_i \boldsymbol{\phi}_{iy} \end{bmatrix} \quad \text{and} \quad \begin{bmatrix} \boldsymbol{\psi}_i \\ \lambda_i \boldsymbol{\psi}_i \end{bmatrix} = \begin{bmatrix} \boldsymbol{\psi}_{ix} \\ \boldsymbol{\psi}_{iy} \\ \lambda_i \boldsymbol{\psi}_{ix} \\ \lambda_i \boldsymbol{\psi}_{iy} \end{bmatrix} \tag{4.16}$$

Which is used in (4.14)

$$(\mathbf{A}\lambda_i + \mathbf{B})\,\tilde{\boldsymbol{\psi}}_i = \left(\begin{bmatrix} \mathbf{C}_{nx}+\mathbf{C}_{rx} & \Omega\mathbf{G}_y & \mathbf{M}_x & \mathbf{0} \\ -\Omega\mathbf{G}_x & \mathbf{C}_{ny}+\mathbf{C}_{ry} & \mathbf{0} & \mathbf{M}_y \\ \mathbf{M}_x & \mathbf{0} & \mathbf{0} & \mathbf{0} \\ \mathbf{0} & \mathbf{M}_y & \mathbf{0} & \mathbf{0} \end{bmatrix} \lambda_i + \begin{bmatrix} \mathbf{K}_x & \Omega\mathbf{C}_{ry} & \mathbf{0} & \mathbf{0} \\ -\Omega\mathbf{C}_{rx} & \mathbf{K}_y & \mathbf{0} & \mathbf{0} \\ \mathbf{0} & \mathbf{0} & -\mathbf{M}_x & \mathbf{0} \\ \mathbf{0} & \mathbf{0} & \mathbf{0} & -\mathbf{M}_y \end{bmatrix} \right) \begin{bmatrix} \boldsymbol{\psi}_{ix} \\ \boldsymbol{\psi}_{iy} \\ \lambda_i\boldsymbol{\psi}_{ix} \\ \lambda_i\boldsymbol{\psi}_{iy} \end{bmatrix} = \mathbf{0} \tag{4.17}$$

or

$$\begin{bmatrix} \mathbf{M}_x\boldsymbol{\psi}_{ix}\lambda_i^2 + \left((\mathbf{C}_{nx}+\mathbf{C}_{rx})\,\boldsymbol{\psi}_{ix} + \Omega\mathbf{G}_y\boldsymbol{\psi}_{iy}\right)\lambda_i + \mathbf{K}_x\boldsymbol{\psi}_{ix} + \Omega\mathbf{C}_{ry}\boldsymbol{\psi}_{iy} \\ \mathbf{M}_y\boldsymbol{\psi}_{iy}\lambda^2 + \left((\mathbf{C}_{ny}+\mathbf{C}_{ry})\,\boldsymbol{\psi}_{iy} - \Omega\mathbf{G}_x\boldsymbol{\psi}_x\right)\lambda_i + \mathbf{K}_{iy}\boldsymbol{\psi}_{iy} - \Omega\mathbf{C}_{rx}\boldsymbol{\psi}_{ix} \\ \mathbf{0} \\ \mathbf{0} \end{bmatrix} = \mathbf{0} \tag{4.18}$$

and with (4.15)

$$(\mathbf{A}\lambda_i + \mathbf{B})^T\,\tilde{\boldsymbol{\phi}}_i = \left(\begin{bmatrix} \mathbf{C}_{nx}+\mathbf{C}_{rx} & -\Omega\mathbf{G}_x & \mathbf{M}_x & \mathbf{0} \\ \Omega\mathbf{G}_y & \mathbf{C}_{ny}+\mathbf{C}_{ry} & \mathbf{0} & \mathbf{M}_y \\ \mathbf{M}_x & \mathbf{0} & \mathbf{0} & \mathbf{0} \\ \mathbf{0} & \mathbf{M}_y & \mathbf{0} & \mathbf{0} \end{bmatrix} \lambda_i + \begin{bmatrix} \mathbf{K}_x & -\Omega\mathbf{C}_{rx} & \mathbf{0} & \mathbf{0} \\ \Omega\mathbf{C}_{ry} & \mathbf{K}_y & \mathbf{0} & \mathbf{0} \\ \mathbf{0} & \mathbf{0} & -\mathbf{M}_x & \mathbf{0} \\ \mathbf{0} & \mathbf{0} & \mathbf{0} & -\mathbf{M}_y \end{bmatrix} \right) \begin{bmatrix} \boldsymbol{\phi}_{ix} \\ \boldsymbol{\phi}_{iy} \\ \lambda\boldsymbol{\phi}_{ix} \\ \lambda\boldsymbol{\phi}_{iy} \end{bmatrix} = \mathbf{0} \tag{4.19}$$

or

$$\begin{bmatrix} \mathbf{M}_x\boldsymbol{\phi}_{ix}\lambda_i^2 + \left((\mathbf{C}_{nx}+\mathbf{C}_{rx})\,\boldsymbol{\phi}_{ix} - \Omega\mathbf{G}_x\boldsymbol{\phi}_{iy}\right)\lambda_i + \mathbf{K}_x\boldsymbol{\phi}_{ix} - \Omega\mathbf{C}_{rx}\boldsymbol{\phi}_{iy} \\ \mathbf{M}_y\boldsymbol{\phi}_{ix}\lambda_i^2 + \left((\mathbf{C}_{ny}+\mathbf{C}_{ry})\,\boldsymbol{\phi}_{iy} + \Omega\mathbf{G}_y\boldsymbol{\phi}_{ix}\right)\lambda + \mathbf{K}_y\boldsymbol{\phi}_{iy} + \Omega\mathbf{C}_{ry}\boldsymbol{\phi}_{ix} \\ \mathbf{0} \\ \mathbf{0} \end{bmatrix} = \mathbf{0} \tag{4.20}$$

Under the assumption that

$$\mathbf{G}_x = \mathbf{G}_y \quad \text{and} \quad \mathbf{C}_{rx} = \mathbf{C}_{ry} \tag{4.21}$$

which holds in axisymmetric systems, and by combining (4.18) and (4.20) the following is true

$$\alpha \boldsymbol{\psi}_{ix} = \boldsymbol{\phi}_{ix} \tag{4.22}$$

$$-\alpha \boldsymbol{\psi}_{iy} = \boldsymbol{\phi}_{iy} \tag{4.23}$$

This means that the left eigenvectors can be calculated if the right eigenvectors are known. Because both left and right eigenvectors are arbitrarily scaled, α might be 1 as well. However, any kind of scaling can be chosen. Note that α can also be complex valued. The assumption made in (4.21) still includes the majority of rotors. It does not imply entire axisymmetry, because mass, stiffness and nonrotating damping can still differ in both x and y direction. The gyroscopic effect is generally axisymmetric, because it is caused by an inertia such as disks or blades. The same holds for the rotating damping.

4.2.3 x and y relation in axisymmetric systems

More relations can be defined if the system is entirely axisymmetric. The behaviour of x- and y-direction is the same because of the axisymmetry. The only difference is a phase difference, more specifically a 90° phase difference. Because the eigenvectors are linked to the ratio of motion between the different points, and because of the complex representation the 90° phase difference corresponds to a multiplication with the complex operator $-i$, for a forward mode, or i for a backward mode, it hold for a forward mode that:

$$\boldsymbol{\psi}_{ix} = -i\boldsymbol{\psi}_{iy} \tag{4.24}$$

and for a backward mode

$$\boldsymbol{\psi}_{ix} = i\boldsymbol{\psi}_{iy} \tag{4.25}$$

Both (4.24) and (4.25) have a particular influence on the parameters $\hat{g}_i$, $\hat{c}_{rss}$ and $\hat{c}_{rs}$. For the gyroscopic effect

$$\hat{g}_i = \begin{bmatrix} \boldsymbol{\phi}_{ix} \\ \boldsymbol{\phi}_{iy} \end{bmatrix}^T \begin{bmatrix} \mathbf{0} & \mathbf{G} \\ -\mathbf{G} & \mathbf{0} \end{bmatrix} \begin{bmatrix} \boldsymbol{\psi}_{ix} \\ \boldsymbol{\psi}_{iy} \end{bmatrix} = -\boldsymbol{\phi}_{iy}\mathbf{G}\boldsymbol{\psi}_{ix} + \boldsymbol{\phi}_{ix}\mathbf{G}\boldsymbol{\psi}_{iy} \tag{4.26}$$

which for a forward mode, by using (4.22) and (4.24) is equal to

$$\hat{g}_i = -2i\alpha \boldsymbol{\psi}_{ix}\mathbf{G}\boldsymbol{\psi}_{ix} \tag{4.27}$$

and for a backward mode

$$\hat{g}_i = 2i\alpha\boldsymbol{\psi}_{ix}\mathbf{G}\boldsymbol{\psi}_{ix} \tag{4.28}$$

or

$$\hat{g}_{i(backward)} = -\hat{g}_{i(forward)} \tag{4.29}$$

The same is true for the rotating damping

$$\hat{c}_{rss(backward)} = -\hat{c}_{rss(forward)} \tag{4.30}$$

moreover

$$\hat{c}_{rs(forward)} = -i\hat{c}_{rss(forward)} \tag{4.31}$$

$$\hat{c}_{rs(backward)} = i\hat{c}_{rss(backward)} \tag{4.32}$$

4.2.4 Perturbation analysis

The rotating system as described by the equations of motion in (4.1) is a gyroscopic system, including internal and external damping. It is common practice to study such systems by means of perturbation analysis as done by Meirovitch in [52], Wang and Kirkhope in [53, 54] or Sawicki in [55]. Generally, the purpose of perturbation analysis is to obtain a simplified representation of the response analysis. In this research, perturbation analysis is used to get insight into the modal parameters and especially the influence on the decay rate and provides unique insights into the modal model. The linear speed dependent model can be seen as a perturbation of the undamped gyroscopic system, i.e.

$$\mathbf{A} = \mathbf{A}_0 + \mathbf{A}_1 \quad ; \quad \mathbf{B} = \mathbf{B}_0 + \mathbf{B}_1 \tag{4.33}$$

with

$$\mathbf{A}_0 = \begin{bmatrix} \mathbf{M} & \mathbf{0} \\ \mathbf{0} & \mathbf{K} \end{bmatrix} \quad ; \qquad \mathbf{A}_1 = \begin{bmatrix} \mathbf{0} & \mathbf{0} \\ \mathbf{0} & \Omega\mathbf{C}_{rss} \end{bmatrix} \tag{4.34}$$

$$\mathbf{B}_0 = \begin{bmatrix} \Omega\mathbf{G} & \mathbf{K} \\ -\mathbf{K} & \mathbf{0} \end{bmatrix} \quad ; \qquad \mathbf{B}_1 = \begin{bmatrix} \mathbf{C}_n + \mathbf{C}_{rs} & \Omega\mathbf{C}_{rss} \\ -\Omega\mathbf{C}_{rss} & \mathbf{0} \end{bmatrix} \tag{4.35}$$

A system with n degrees of freedom results in a dimension of $2n \times 2n$ for the matrices **A** and **B**. In a single mode, the unperturbed left and right eigenvalue problems are then written as

$$(\mathbf{A}_0\lambda_{0i} + \mathbf{B}_0)\,\tilde{\boldsymbol{\psi}}_{0i} = 0 \tag{4.36}$$

$$\tilde{\boldsymbol{\phi}}_{0i}^T\,(\mathbf{A}_0\lambda_{0i} + \mathbf{B}_0) = 0 \tag{4.37}$$

There is orthogonality and the eigenvectors are scaled such that

$$\tilde{\boldsymbol{\phi}}_{0i}^T\mathbf{A}_0\tilde{\boldsymbol{\psi}}_{0i} = 1 \tag{4.38}$$

$$\tilde{\boldsymbol{\phi}}_{0i}^T\mathbf{B}_0\tilde{\boldsymbol{\psi}}_{0i} = -\lambda_{0i} \tag{4.39}$$

Due to the scaling, these undamped eigenvectors are complex valued. Meirovitch [52] shows that for gyroscopic systems, λ_{0i} is purely imaginary and left and right eigenvectors are each others conjugate, $\tilde{\boldsymbol{\psi}}_{0i} = \overline{\tilde{\boldsymbol{\phi}}_{0i}}$. The modal parameters of the unperturbed system are

$$\hat{m}_{0i} = \tilde{\boldsymbol{\phi}}_{0i}^T\mathbf{M}\tilde{\boldsymbol{\psi}}_{0i} \tag{4.40}$$

$$\hat{g}_{0i} = \tilde{\boldsymbol{\phi}}_{0i}^T\mathbf{G}\tilde{\boldsymbol{\psi}}_{0i} \tag{4.41}$$

$$\hat{k}_{0i} = \tilde{\boldsymbol{\phi}}_{0i}^T\mathbf{K}\tilde{\boldsymbol{\psi}}_{0i}^T \tag{4.42}$$

Because **M** and **K** are symmetric and $\tilde{\boldsymbol{\psi}}_{0i} = \overline{\tilde{\boldsymbol{\phi}}_{0i}}$, $\hat{m}_{0i}$ and $\hat{k}_{0i}$ are real. **G** is skew-symmetric, so $\hat{g}_{0i}$ is purely imaginary. It is possible to define a relation between the matrix of undamped right eigenvectors, $\tilde{\boldsymbol{\psi}}_0$, and the damped eigenvector of a single mode $\tilde{\boldsymbol{\psi}}_i$

$$\tilde{\boldsymbol{\psi}}_i = \tilde{\boldsymbol{\psi}}_0\mathbf{E}_i = \sum_{k=1}^{2n}\tilde{\boldsymbol{\psi}}_{0k}e_{ik} \tag{4.43}$$

where $\mathbf{E}_i$ is a $2n \times 1$ vector and describes the damped eigenvector as a linear combination of the undamped right eigenvectors. The scalars e_{ik} are entries of the vector $\mathbf{E}_i$ and correspond each to an undamped eigenvector. Now, equation (4.5) is premultiplied by the corresponding undamped left eigenvector

$$\tilde{\boldsymbol{\phi}}_{0i}^T\,(\mathbf{A}\lambda_i + \mathbf{B})\,\tilde{\boldsymbol{\psi}}_i = 0 \tag{4.44}$$

or by using (4.33)

$$\tilde{\boldsymbol{\phi}}_{0i}^T \mathbf{A}_0 \tilde{\boldsymbol{\psi}}_i \lambda_i + \tilde{\boldsymbol{\phi}}_{0i}^T \mathbf{A}_1 \tilde{\boldsymbol{\psi}}_i \lambda_i + \tilde{\boldsymbol{\phi}}_{0i}^T \mathbf{B}_0 \tilde{\boldsymbol{\psi}}_i + \tilde{\boldsymbol{\phi}}_{0i}^T \mathbf{B}_1 \tilde{\boldsymbol{\psi}}_i \tag{4.45}$$

Due to (4.43) and the orthogonality properties of the undamped eigenvectors and the unperturbed system, this is simplified to

$$\hat{m}_{0i} \lambda_i^2 + \Omega \hat{g}_{0i} \lambda_i + \hat{k}_{0i} + \Omega \hat{c}_{rssi} + (\hat{c}_{ni} + \hat{c}_{rsi}) \lambda_i = 0 \tag{4.46}$$

where

$$\hat{c}_{rssi} = \tilde{\boldsymbol{\phi}}_{0i}^T \mathbf{C}_{rss} \tilde{\boldsymbol{\psi}}_i = \tilde{\boldsymbol{\phi}}_{0i}^T \mathbf{C}_{rss} \sum_{k=1}^{2n} \tilde{\boldsymbol{\psi}}_{0k} e_{ik} \tag{4.47}$$

$$\hat{c}_{ni} + \hat{c}_{rsi} = \tilde{\boldsymbol{\phi}}_{0i}^T (\mathbf{C}_n + \mathbf{C}_{rs}) \tilde{\boldsymbol{\psi}}_i = \tilde{\boldsymbol{\phi}}_{0i}^T (\mathbf{C}_n + \mathbf{C}_{rs}) \sum_{k=1}^{2n} \tilde{\boldsymbol{\psi}}_{0k} e_{ik} \tag{4.48}$$

Assume that the system is lightly damped, which theoretically means that the norms of $\mathbf{A}_1$ and $\mathbf{B}_1$ are significantly smaller then the norms of $\mathbf{A}_0$ and $\mathbf{B}_0$ [52]. The assumption of lightly damped systems is widely used in mechanical systems. A practical implication of light damping leads to the observation that the damped eigenvectors are approximately equal to the undamped eigenvectors. This observation is used as a validity check in the chapter 5. In the case of light damping, the scalars e_{ik} in equation (4.43) are close to unity if $i = k$ and nearly zero if $i \neq k$. Under this assumption, $\hat{c}_{rssi}$ is almost purely imaginary and $\hat{c}_{ni} + \hat{c}_{rsi}$ nearly real.

4.3 The decay rate and the stability threshold speed

It is shown by perturbation analysis that the parameters in the modal model

$$\hat{m}_i \lambda^2 + (\hat{c}_{ni} + \hat{c}_{rsi} + \Omega \hat{g}_i) \lambda + \hat{k}_i + \Omega \hat{c}_{rssi} = 0 \tag{4.49}$$

can be approximated by purely real or purely imaginary quantities. Assume a forward mode such that $\hat{c}_{rsi} = \hat{c}_{ri} = -i\hat{c}_{rssi}$. The equation can be rewritten as

$$\hat{m}_i \lambda_i^2 + (\hat{c}_{ni} + \hat{c}_{ri} - \Omega i \hat{g}_i) \lambda_i + \hat{k}_i - \Omega i \hat{c}_{ri} = 0 \tag{4.50}$$

In which all modal parameters are real and positive. This is a consequence of the perturbation analysis. This representation is similar to the widely used concept

of the Jeffcott rotor [50] [15] [30], but with the appearance of the gyroscopic effect and rotating damping. λ_i is complex valued, so λ_i is written as $\sigma_i + i\omega_i$.

$$\begin{aligned}\hat{m}_i\left(\sigma_i^2 - \omega_i^2\right) + 2\hat{m}\sigma_i\omega_i i + \left(\hat{c}_{ni} + \hat{c}_{ri}\right)\sigma_i + \left(\hat{c}_{ni} + \hat{c}_{ri}\right)\omega_i i \\ -\Omega\hat{g}\sigma_i i + \Omega\hat{g}_i\omega_i + \hat{k}_i - \Omega\hat{c}_{ri}i = 0\end{aligned} \tag{4.51}$$

Separating into real and imaginary parts

$$\begin{cases}\hat{m}_i\left(\sigma_i^2 - \omega_i^2\right) + \left(c_{ni} + c_{ri}\right)\sigma_i + \Omega\hat{g}_i\omega_i + \hat{k}_i = 0 \\ 2\hat{m}\sigma_i\omega_i + \left(\hat{c}_{ni} + \hat{c}_{ri}\right)\omega_i - \Omega\hat{g}\sigma_i - \Omega\hat{c}_{ri} = 0\end{cases} \tag{4.52}$$

From the second equation, σ_i is derived

$$\sigma_i = \frac{\Omega\hat{c}_{ri} - \left(\hat{c}_{ni} + \hat{c}_{ri}\right)\omega_i}{2\hat{m}_i\omega_i - \Omega\hat{g}_i} \tag{4.53}$$

The stability threshold speed occurs at $\sigma_i = 0$. This means that it can be found at $\lambda_i = i\omega_i$ or

$$\Omega_{st} = \omega_{st}\left(1 + \frac{c_{ni}}{c_{ri}}\right) \tag{4.54}$$

with Ω_{st} the stability threshold speed. The corresponding whirl speed ω_{st} is derived from the first equation in (4.52)

$$\omega_{st} = \pm\sqrt{\frac{\hat{k}_i}{\hat{m}_i - \hat{g}_i\left(1 + \frac{c_{ni}}{c_{ri}}\right)}} \tag{4.55}$$

Equation (4.54) shows that the stability threshold speed is mainly determined by the ratio between the nonrotating damping and the rotating damping. By increasing the nonrotating damping in the system, the stability threshold speed increases, a conclusion that was already made by Newkirk and Kimball [10] [11]. Increasing the damping in the foundation, increases the stability. The gyroscopic effect, in the denominator of (4.55) has a stabilizing effect because ω_{st} becomes higher.

4.4 Illustration of the modal model concepts

As an illustration of the above described concepts, an example is presented. The example is the rotating damping setup as described in chapter 3 that is discretized

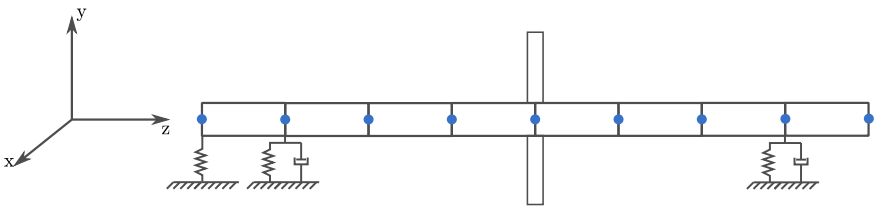

Figure 4.1: Schematic representation of the used finite element model

by means of finite elements as described in chapter 2. All calculations are done in simulation as a proof of concept. The difficulties to translate this to experiments are discussed later on. The shaft, divided in eight elements is shown in Figure 4.1. The used parameters for the shaft are listed in Table 4.1. The bearing parameters are tuned with a trial and error procedure to yield realistic results. The material damping of the shaft is chosen proportional to the stiffness of the shaft. However, because the damping matrix also contains the damping of the bearings, the overall damping is not proportional. Six elements lead to 9 nodes, with each 4 degrees of freedom. The model has thus 36 degrees of freedom. The bearings are located on node 2 and 8 and a coupling is modelled as a stiffness on node 1.

Shaft	
Diameter $[m]$	0.01
Length $[m]$	1.487
Young modulus $[N/m^2]$	2x10^{11}
Density $[kg/m^3]$	7730
Proportional damping factor shaft $[N/m]$	6.5x10^{-5}
Translational stiffness bearings $[N/m]$	5.60x10^{7}
Rotational stiffness bearings $[N/m]$	4.50x10^{2}
Stiffness of coupling $[N/m]$	2.00x10^{6}
Translational damping bearings $[Ns/m]$	0.22
Rotational damping bearings $[Ns/m]$	0.22
Disk	
Diameter disk $[m]$	0.15
Thickness $[m]$	0.015
Density $[kg/m^3]$	2702
Damping $[Ns/m]$	7.5x10^{-1}

Table 4.1: Parameters used in the example

4.4.1 Decay rate plot

The stability of the shaft is analysed theoretically. Table 4.2 lists the first three forward and backward poles, ordered by the imaginary part at 0, 2000 rpm and 4000 rpm. All real parts are negative, except for the one corresponding to the first forward mode at 4000 rpm, meaning this pole is unstable. The evolution of the poles is visualized in the *decay rate plot* for the first two forward and backward modes (Figure 4.2). A decay rate plot plots the real part of the poles as a function of the rotating speed. When one of the real parts becomes positive, the rotor is unstable. For this rotor, the first forward mode becomes unstable at a spin speed of 3768.56 rpm. This is above the first critical speed of 1618 rpm (169.39 rad/s). Because of the negligible gyroscopic effect on the first mode, there is not much difference between the imaginary parts of the forward modes and the backward modes.

	0 rpm		2000 rpm		4000 rpm	
	Real	Imaginary	Real	Imaginary	Real	Imaginary
1 FW	-0.91	169.39	-0.43	169.41	0.056	169.44
1 BW	-0.91	169.39	-1.40	169.38	-1.88	169.36
2 FW	-8.83	461.95	-7.96	449.14	-7.13	435.65
2 BW	-8.83	461.95	-9.72	473.95	-10.61	485.07
3 FW	-17.78	723.88	-16.93	727.57	-16.09	733.21
3 BW	-17.78	723.88	-18.62	716.19	-19.43	710.59

Table 4.2: First three forward and backward poles, ordered by the imaginary part, at 0 and 2000 and 4000 rpm

4.4.2 The modal model

Now, the results are compared to the approximated modal model that has been described in section 4.3. The operating speed is arbitrary and chosen to be 1500 rpm. The general decoupling for the first forward mode leads to the modal parameters in Table 4.3.

As is expected, the parameters are complex valued. However, $\hat{m}_i$, $\hat{c}_{ni} + \hat{c}_{ri}$ and $\hat{k}_i$ have a real part that is significantly larger then the imaginary part. $\hat{g}_i$ and $\hat{c}_{ri}$ have a large imaginary part compared to the real part. This means that the assumptions that are made by the perturbation analysis are valid and that the modal model of (4.49) can be used. Thus, the stability threshold speed is approximated by

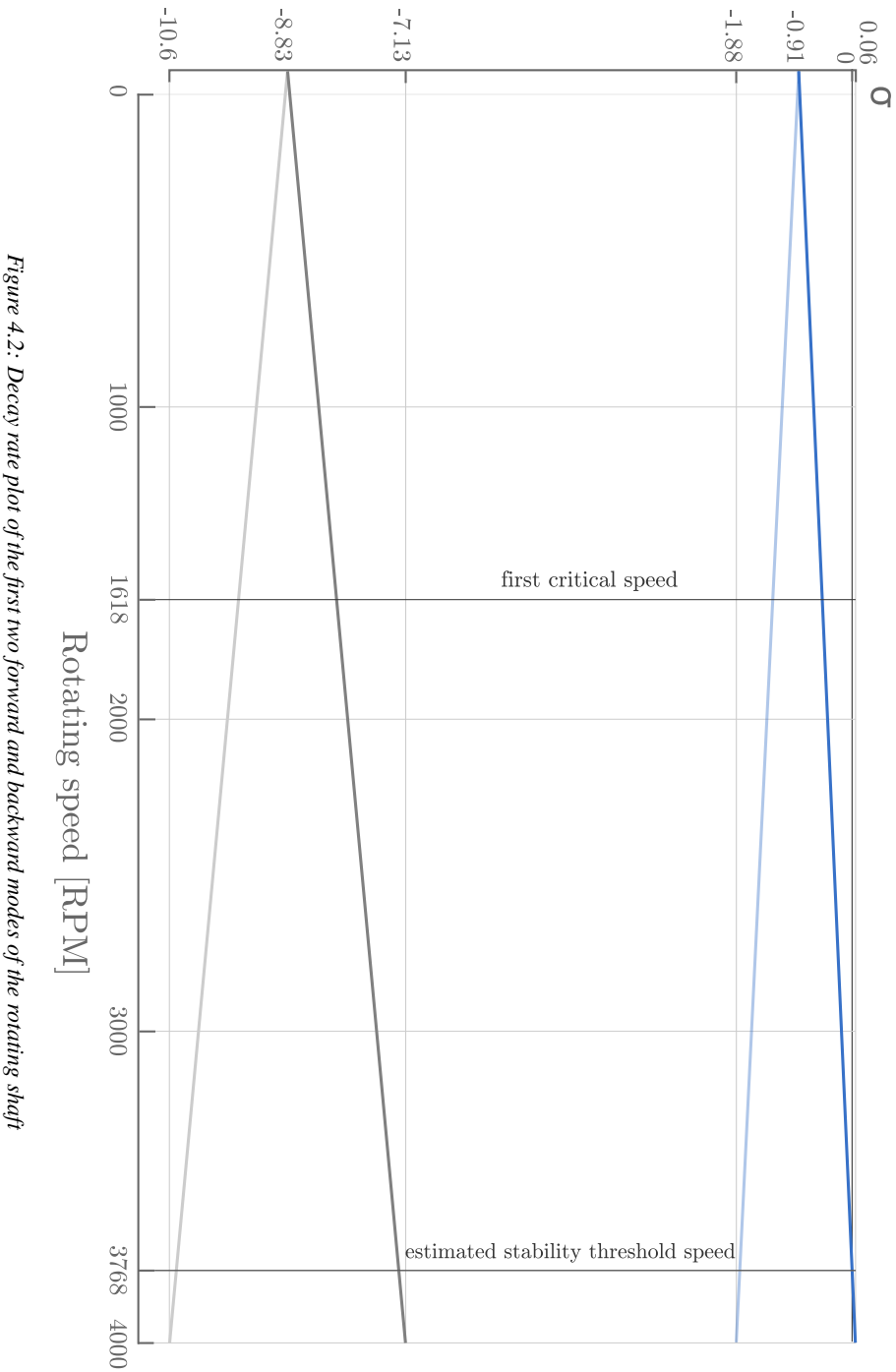

Figure 4.2: Decay rate plot of the first two forward and backward modes of the rotating shaft

	Real	Imaginary
$\hat{m}_i$	1.7×10^{-5}	2.0×10^{-8}
$\hat{c}_{ni}$+$\hat{c}_{ri}$	3.2×10^{-5}	1.2×10^{-6}
$i\hat{g}_i$	2.4×10^{-10}	3.0×10^{-9}
$\hat{k}_i$	5.0×10^{-1}	5.5×10^{-4}
$i\hat{c}_{ri}$	1.0×10^{-8}	1.4×10^{-5}

Table 4.3: Calculated modal parameters

$$\Omega_{st} = \omega_{st}\left(1 + \frac{\Re\left(\hat{c}_{ni}\right)}{\Im\left(\hat{c}_{ri}\right)}\right) \tag{4.56}$$

where $\Re()$ is the real part and $\Im()$ the imaginary part. The corresponding whirl speed is

$$\omega_{st} = \sqrt{\frac{\Re\left(\hat{k}_i\right)}{\Re(\hat{m}_i) - \Im\left(\hat{g}_i\right)\left(1 + \frac{\Re(\hat{c}_{ni})}{\Im(\hat{c}_{ri})}\right)}} \tag{4.57}$$

Which corresponds to 3770.17 rpm, which is only 1.61 rpm, higher then the actual stability threshold speed. This is relatively 0.04%.

4.5 Conclusion

A conventional way of getting insight into a multiple degree of freedom model is decoupling it into a modal model. The modal model described in this chapter is a unique extension to the Jeffcott rotor. A modal model yields the modal parameters: modal mass, stiffness and damping. These parameters, combined in a characteristic equation are useful to describe the system poles and consequently the real part of the poles or the decay rate. Because of the unconventional structure of the linear speed dependent model, more specifically, the appearance of gyroscopic forces and rotating damping, the modal parameters are complex valued. Therefore, a straightforward representation of the decay rate is difficult. However, by assuming that the gyroscopic effect and the rotating damping are axisymmetric, it is shown that there is an obvious relation between left and right eigenvectors. When the entire system is axisymmetric, there is even a relation between the x and the y direction, in the corresponding parts of the eigenvectors. A third assumption is small damping. When there is small damping, the modal parameters can be approximated by perturbation analysis. It is shown that there are modal parameters that are nearly real, and modal parameters that are nearly imaginary. With

this approximation, the modal model is similar to the Jeffcott rotor, a widely used concept. From this concept, the decay rate, and the stability threshold speed are easily expressed as a function of the modal parameters. A realistic example shows that the assumptions hold in simulation. In chapter 5, this theoretical approach is experimentally validated.

5 Experimental prediction of the stability threshold speed

5.1 Introduction

The modal model, which is derived and explained in chapter 4 creates a framework for experimental validation. The simplified representation with real and positive parameters results in a clear expression for the decay rate and the corresponding stability threshold speed. However, there are still some remarks. First, in chapter 4, light damping is assumed as a justification for the perturbation analysis. Light damping is difficult to quantify, especially in an experiment. In this chapter, a procedure is proposed to get a clear indication of light damping. Second, the appearance of gyroscopic effect and rotating damping as an imaginary term in the modal model has some practical consequences. Rotating damping for instance mainly has an impact on the real part of the poles (the decay rate) and the gyroscopic effect mainly affects the imaginary part (the whirl). This effect can be observed in the frequency response functions as well. The part of the rotating damping that is appearing as a stiffness term, physically influences the energy dissipation and is actually a nonconservative force. The gyroscopic effect, on the other hand is a conservative force although it is appearing as a damping term. Therefore, rotating damping is an apparent damping and the gyroscopic effect is an apparant mass. In this chapter, it is explained how this insight can be used to reformulate the modal model to a more suitable structure for experimental verifiation. An equivalent decay rate model is proposed, this model is used in a measurement procedure which

allows to predict the stability threshold speed. Consequently, the proposed equivalent decay rate model and the measurement procedure are used to predict the stability threshold speed on the rotating damping setup, with a disk in the middle. From the measured frequency response functions, the poles are extracted, and the decay rate plot is constructed. It is shown by measurements that the shaft exhibits nonstationary behaviour near the stability threshold speed and becomes unstable above the predicted stability threshold speed. To summarize: first, a validity check of the modal model is proposed. Second, an equivalent decay rate model is derived, which results in a similar decay rate as the modal model and a measurement procedure is proposed. Finally, the measurements and results are discussed.

5.2 Cyclic energy dissipation and stability

The appearance of skew-symmetric matrices in a rotordynamic system has a particular effect on the energy dissipation and stability of the system as explained by Adams in [1] and [56]. Consider the equations of motion for a system with only two degrees of freedom in absence of the gyroscopic effect

$$\begin{bmatrix} m & 0 \\ 0 & m \end{bmatrix} \begin{Bmatrix} \ddot{x} \\ \ddot{y} \end{Bmatrix} + \begin{bmatrix} c_n + c_r & 0 \\ 0 & c_n + c_r \end{bmatrix} \begin{Bmatrix} \dot{x} \\ \dot{y} \end{Bmatrix} + \left(\begin{bmatrix} k & 0 \\ 0 & k \end{bmatrix} + \Omega \begin{bmatrix} 0 & c_r \\ -c_r & 0 \end{bmatrix} \right) \begin{Bmatrix} x \\ y \end{Bmatrix} = \begin{Bmatrix} f_x \\ f_y \end{Bmatrix} \tag{5.1}$$

The work done by the displacement term or apparent stiffness term of the rotating damping can be expressed as

$$dw = -\Omega \begin{bmatrix} 0 & c_r \\ -c_r & 0 \end{bmatrix} \begin{Bmatrix} x \\ y \end{Bmatrix} \{dx \quad dy\} = \Omega \left(-c_r y dx + c_r x dy\right) \equiv f_x dx + f_y dy$$
$$\therefore \frac{\partial f_x}{\partial y} = -\Omega c_r \quad and \quad \frac{\partial f_y}{\partial x} = \Omega c_r \tag{5.2}$$

Because $\partial f_x / \partial y \neq \partial f_y / \partial x$, dw is not an exact differential, leading to a nonconservative force field. This means that the rotating damping appearing as a stiffness term actually dissipates energy. Together with the regular damping, the sum of the nonconservative forces of the rotating system can be written as

$$\begin{Bmatrix} p_x \\ p_y \end{Bmatrix} = - \begin{bmatrix} c_n + c_r & 0 \\ 0 & c_n + c_r \end{bmatrix} \begin{Bmatrix} \dot{x} \\ \dot{y} \end{Bmatrix} - \Omega \begin{bmatrix} 0 & c_r \\ -c_r & 0 \end{bmatrix} \begin{Bmatrix} x \\ y \end{Bmatrix} \tag{5.3}$$

Suppose that the rotor is operated at a given speed Ω and whirling at ω. The whirling can be expressed as a harmonic motion in x and y direction, $x =$

$X\sin(\omega t+\phi_x)$ and $y=Y\sin(\omega t+\phi_y)$. The energy per cycle that is exchanged due to these forces can be expressed as

$$E_{cyc}=\oint p_x dx+p_y dy=\int_0^{2\pi/\omega}\left(p_x\dot{x}dt+p_y\dot{y}dt\right) \tag{5.4}$$

or

$$E_{cyc}=-\pi\left[\underbrace{\omega\left(c_n+c_r\right)\left(X^2+Y^2\right)}_{\text{regular damping effect}}-\underbrace{2\Omega XY\sin\left(\phi_x-\phi_y\right)}_{\text{speed dependent effect}}\right] \tag{5.5}$$

This is an important expression because it shows that the appearance of rotating damping can lead to a positive energy per cycle or instability. The first term is a regular damping effect and causes a cyclic decrease of the energy. The second term is not only speed dependent, but also depends on the phase difference between ϕ_x and ϕ_y. Whenever the whirling ω occurs in the same direction as the rotation Ω, which is called a forward mode, $\sin(\phi_x-\phi_y)>0$. As Ω increases the influence of the second term in (5.5) increases. When the energy per cycle becomes positive, instability occurs. For backward modes, $\sin(\phi_x-\phi_y)<0$, and the effect of the second term in (5.5) is always stabilizing.

5.3 Indication of light damping

5.3.1 The assumption of light damping

A necessary condition to use the perturbation analysis that is described in chapter 4 is the assumption of a light damping. Light damping is commonly assumed in mechanical systems, especially systems where experimental modal analysis is considered [57]. Theoretically, there are some attempts to quantify light damping. A first attempt is the use of *critical damping*. Light damping is typically of the order of 1% critical damping. Critical damping is commonly used in single degree of freedom systems, or in modal coordinates. It is rather difficult to define critical damping on multiple degree of freedom systems. An attempt is made by Beskos and Boley in [58] where it has especially a computational relevance. A second option is to describe light damping is by the *perturbation analysis* itself. When damping is described as a perturbation of the undamped systems, as is done in (4.34) and (4.35), the norms on the matrices can be used as an indication for light damping. If the norms of the unperturbed matrices are significantly higher then the norms of the matrices causing perturbation [52]. A third method is the use of *the*

eigenvectors. If the undamped eigenvectors are close to the damped eigenvectors, then there is light damping.
Experimentally, defining light damping is more challenging. A percentage of the critical damping for instance requires the excitation of a single mode. In order to use perturbation analysis, the system matrices have to be known. The use of eigenvectors is easier to apply experimentally. The main difficulty here is the knowlegde of the undamped eigenvectors, which have to be calculated from an accurate undamped model. This is, however, easier to overcome, because mass and stiffness are generally easier to model then damping. On the other hand, the extraction of eigenvectors from an experimental setup requires multiple measurement points. Because, in this research, industrial applications are of major importance, the measurement points need to be reduced. Therefore, a unique procedure that provides an *indication* for light damping is proposed.

5.3.2 Light damping experimentally

By taking a closer look at equation (4.43)

$$\tilde{\boldsymbol{\psi}}_i = \tilde{\boldsymbol{\psi}}_0 \mathbf{E}_i = \sum_{k=1}^{2n} \tilde{\boldsymbol{\psi}}_{0k} e_{ik} \tag{5.6}$$

it is seen that the damped eigenvectors can be written as a linear combination of the undamped eigenvector. In the case of light damping, the scalars e_{ik} in equation (4.43) are close to unity if $i = k$ and nearly zero if $i \neq k$. This means practically that the undamped eigenvectors are close to the damped eigenvectors. Experimentally, the undamped eigenvectors can not be measured. However, if an accurate model is available, the undamped eigenvectors are easily calculated and compared to the measured damped eigenvectors. On the other hand, as stated above, the extraction of eigenvectors from an experimental setup requires multiple measurement points. In order to reduce this, a basic, indicative method is proposed. The frequency response is measured at two points of the setup (Figure 5.1), while rotating. The FRF of the model and the actual measurement are compared, based upon the value at resonance. If the difference of these ratios are smaller then one order, then there is light damping.

For the rotating damping setup, two frequency response functions are measured at 100 rpm. The excitation is at 0.186m from the left and the response is measured at the driving point and at 0.372m from the left. The results are shown in Table 5.1. In the undamped system, the values are purely real, which is expected. The ratio between point 1 and point 2 in the damped system differs slightly from the undamped. There is an imaginary part that is three orders smaller then the real part and the real part smaller then one order. It is concluded that the system can be characterized as lightly damped.

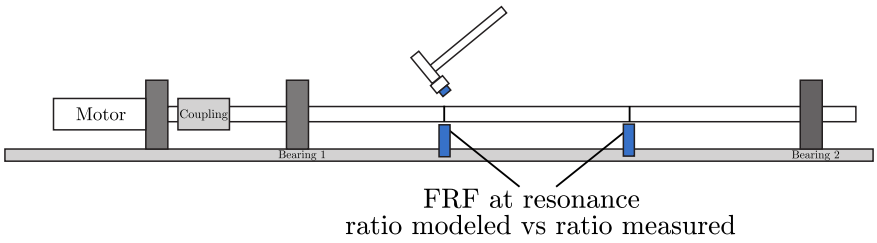

Figure 5.1: Schematic representation of the procedure to verify the light damping

	Undamped from model		Damped from measurements	
	Real	Imaginary	Real	Imaginary
Point 1	6.51×10^{-3}	0	-5.76×10^{-5}	-7.82×10^{-4}
Point 2	1.53×10^{-2}	0	-1.37×10^{-4}	-1.81×10^{-3}
ratio	4.25×10^{-1}	0	4.32×10^{-1}	9.47×10^{-4}

Table 5.1: Ratio between two points of the FRF at resonance for the undamped results from the model and the damped results from the measurements

5.4 Equivalent decay rate model

5.4.1 Frequency response and impulse response

The frequency response for a rotating system is derived in paragraph 2.3.3. The frequency response for a multiple degree of freedom rotating system between the force at location p and the displacement at location q is

$$H_{pq}(\omega) = \sum_{r=1}^{n} \frac{Q_r \psi_{pr} \phi_{qr}}{i\omega - \lambda_r} + \frac{\overline{Q}_r \overline{\psi}_{pr} \overline{\phi}_{qr}}{i\omega - \overline{\lambda}_r} \tag{5.7}$$

with r the mode number, n the number of modes, Q_r the modal scaling constant, ψ_r a right eigenvector and ϕ_r a left eigenvector. $\overline{(\cdot)}$ symbolizes the conjugate. The poles λ_r equal $\sigma_r + i\omega_r$ and are speed dependent. It is convenient to choose the modal scaling constant $Q_r = 1$. The object is to focus on a single mode. However, depending on the gyroscopic effect, there is a chance that a forward and a backward mode are close to each other. The frequency response at a driving point, when only two modes are considered is

$$H_{11}(\omega) = \frac{\psi_{11}\phi_{11}}{i\omega - \lambda_1} + \frac{\overline{\psi}_{11}\overline{\phi}_{11}}{i\omega - \overline{\lambda}_1} + \frac{\psi_{12}\phi_{12}}{i\omega - \lambda_2} + \frac{\overline{\psi}_{12}\overline{\phi}_{12}}{i\omega - \overline{\lambda}_2} \tag{5.8}$$

The corresponding impulse response reads

$$h_{11}(t) = \psi_{11}\phi_{11}\mathrm{e}^{(\sigma_1+i\omega_1)t} + \overline{\psi_{11}\phi_{11}}\mathrm{e}^{(\sigma_1-i\omega_1)t} + \psi_{12}\phi_{12}\mathrm{e}^{(\sigma_2+i\omega_2)t} + \overline{\psi_{12}\phi_{12}}\mathrm{e}^{(\sigma_2-i\omega_2)t} \tag{5.9}$$

This is a combination of two impulse responses. For a forward and a backward mode, when the gyroscopic effect is negligible, ω_1 and ω_2 are equal. Increasing speed causes σ_1 to decrease and σ_2 to increase. This means that the terms in (5.9) corresponding to σ_2 die out faster than the ones corresponding to σ_1. As the speed increases, the effect of the pole λ_2 is reduced. In particular, when the rotating speed is increasing and approaches the stability threshold speed, the effect of the backward mode is negligible meaning that the two degree of freedom modal model can be approximated by a single degree of freedom model.

5.4.2 The single degree of freedom model

The frequency response and impulse response of the modal model show that by increasing the rotating speed, a single degree of freedom approximation becomes valid. Moreover, the rotating damping acts entirely as a nonconservative force leading to energy dissipation, which is shown in paragraph 5.2. This is thus an *apparent damping*. In a similar way, the gyroscopic effect is a conservative force. This is thus an *apparent mass*. Combining these conclusions leads to the formula of an equivalent single degree of freedom model

$$(\hat{m}_i - \Omega\hat{g}_{2i})\,\ddot{x} + (\hat{c}_{1i} - \Omega\hat{c}_{2i})\dot{x} + \hat{k}_i x = 0 \tag{5.10}$$

which is a system where the damping decreases as function of rotating speed, and depending on the gyroscopic effect, the mass changes. In this equation, the gyroscopic effect mainly influence the imaginary part of the poles and the decay rate mainly affects the real part. By proposing a harmonic solution

$$x = r\mathrm{e}^{\sigma_i t}\cos(\omega_i t) \tag{5.11}$$

this leads to

$$\begin{cases} -\hat{c}_{2i}\Omega\sigma_i + \hat{m}_i(\sigma_i^2 - \omega_i^2) - \Omega\hat{g}_{2i}(\sigma_i^2 - \omega_i^2) + \hat{c}_{1i}\sigma_i + \hat{k}_i = 0 \\ (2\hat{m}_i\omega_i - 2\Omega\hat{g}_{2i}\omega_i)\,\sigma_i + \hat{c}_{1i}\omega_i - \Omega\hat{c}_{2i}\omega_i = 0 \end{cases} \tag{5.12}$$

and σ_i

$$\sigma_i = \frac{\Omega\hat{c}_{2i}\omega_i - \hat{c}_{1i}\omega}{2\hat{m}_i\omega_i - 2\Omega\hat{g}_{2i}\omega_i} \tag{5.13}$$

When the gyroscopic effect is low, this is an increasing straight line. By comparing (4.53) and (5.13), $\hat{c}_{1i}$ and $\hat{c}_{2i}$ are

$$\hat{c}_{1i} = \hat{c}_{ni} + \hat{c}_{ri} \tag{5.14}$$

$$\hat{c}_{2i} = \frac{\hat{c}_{ri}}{\omega_i} \tag{5.15}$$

$$\hat{g}_{2i} = \frac{\hat{g}_i}{2\omega_i} \tag{5.16}$$

This equivalent system is convenient for the measurements. Classical techniques allow to estimate the parameters of this single degree of freedom system. The resulting model proofs that a simplified procedure can be used to estimate the stability threshold speed.

5.4.3 Measurement procedure

The purpose of the measurement is to extract the decay rate from a frequency response. Figure 5.2 describes the proposed procedure. First, a measurement is performed at low speed and the frequency response function is extracted. In theory, standstill or 0 rpm is ideal, but in practise a certain low speed is preferred. This is mainly because the motor dynamics have an influence on the behaviour of the whole rotor. For many motors, and also the motor used in this application, the behaviour at standstill differs from rotation. Second, a measurement is performed at a speed below critical and the frequency response function is extracted. A subcritical operating speed ensures stability. For both measurements, the poles for the first peak are extracted. Because the decay rate is an increasing straight line, when the gyroscopic effect is low, an approximation of the decay rate can already be constructed from these two points, and an indication of the stability threshold speed can already be made. Subsequently, increase the operating speed and keep monitoring the decay rate.

Rotating speed [rpm]	Real part of poles [-]	Imaginary part of poles [rad/s]
100	-0.96	165.25
1000	-0.61	164.50
2000	-0.38	163.05
3000	-0.21	162.23

Table 5.2: The poles are extracted at different speeds and splitted into real and imaginary parts

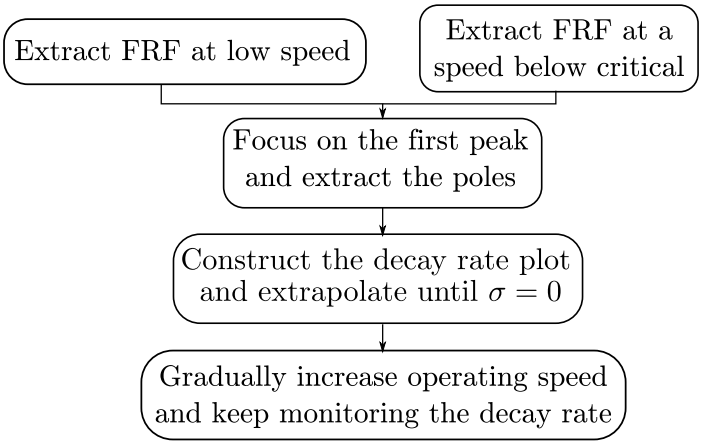

Figure 5.2: Flowchart of the measurement procedure

5.5 Measurements and results

5.5.1 Frequency response functions and extraction of the poles

The results from the H1 estimator on the measurements at 100, 1000, 2000 and 3000 rpm and the single degree of freedom fit are respectively shown in Figure 5.3 to 5.6. It is clear that, at 1000 rpm, the frequency response is contaminated by 16.7 and 33.3 Hz, corresponding to respectively 1000 rpm (fundamental frequency) and 2000 rpm (second harmonic). At 2000 rpm, 33.3 Hz, or the fundamental frequency, is also present. These contaminations do not influence the peak of interest at 26.2 Hz. A half power bandwidth method is used to extract the poles.

The poles are extracted, as described above at different rotating speeds. The results are shown in table 5.2.

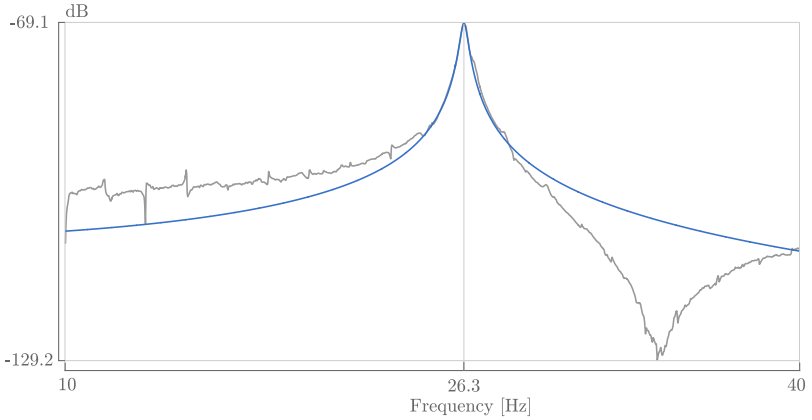

Figure 5.3: Estimated frequency response (gray) and single degree of freedom fit (blue) at 100 rpm

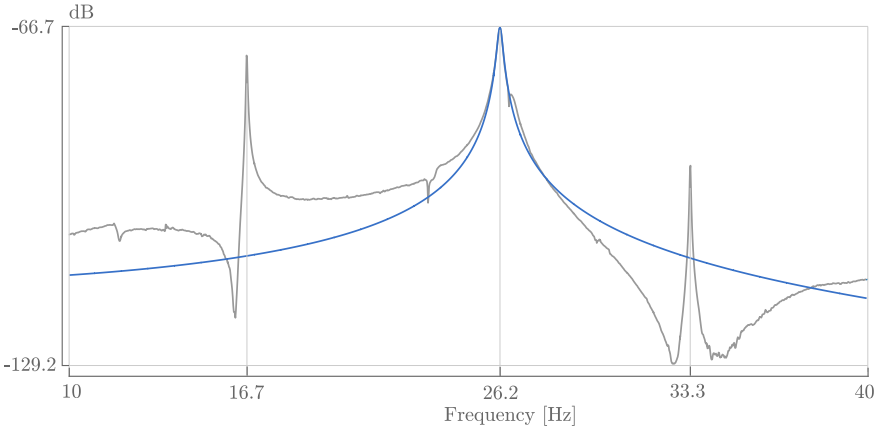

Figure 5.4: Estimated frequency response (gray) and single degree of freedom fit (blue) at 1000 rpm

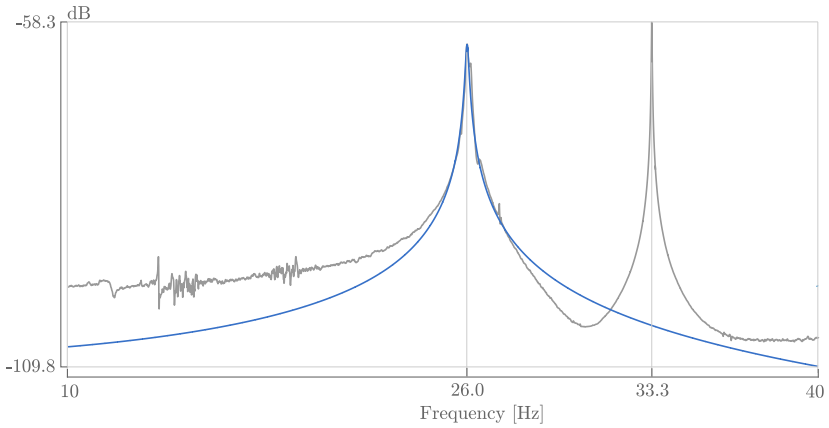

Figure 5.5: Estimated frequency response (gray) and single degree of freedom fit (blue) at 2000 rpm

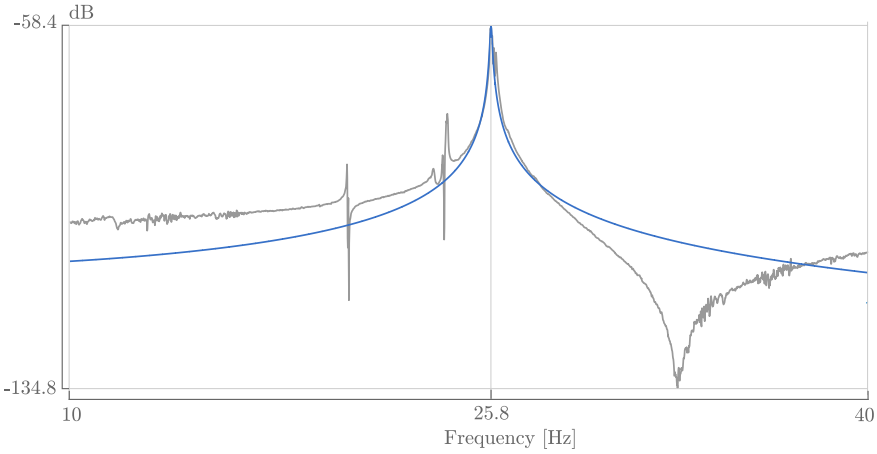

Figure 5.6: Estimated frequency response (gray) and single degree of freedom fit (blue) at 3000 rpm

5.5.2 Decay rate

From the results in Table 5.2, the real part of the poles is plotted in a decay rate plot (Figure 5.7). The critical speed of 1564 rpm is depicted. As expected, the decay rate plot approximates an increasing straight line. This implies, theoretically, that only two points are needed to predict the stability threshold. The measurements at 100 and 1000 rpm yield a linear fit equal to

$$\sigma_{2p}(\Omega) = 3.89 \times 10^{-4}\Omega - 1.00 \tag{5.17}$$

which leads to an estimated stability threshold speed of 2564 rpm. Combining the points of 100, 1000 and 2000 rpm with a linear fit, leads to a

$$\sigma_{3p}(\Omega) = 3.04 \times 10^{-4}\Omega - 0.96 \tag{5.18}$$

and a stability threshold speed of 3158 rpm. An extra point at 3000 rpm gives a decay rate of

$$\sigma_{4p}(\Omega) = 2.48 \times 10^{-4}\Omega - 0.92 \tag{5.19}$$

and a stability threshold speed op 3720 rpm. There are thus, three different slopes from these measurements. Each slope results in a higher stability threshold speed. However, the following measurements show that the prediction is very accurate. Measurements above 3000 rpm are difficult in this setup. The decay rate fitted on 4 points already indicates that the damping is very low. The amplitudes in steady state operation are already high and the measurement of a clear frequency response is not possible. Therefore, a steady state measurement is done at 3500 rpm. The measurement is limited to 50s, for safety reasons. The results are plotted in a waterfall plot (Figure 5.8). In this plot, the frequency spectrum of the displacement is shown for each second. It is clear that the behaviour is not what is expected from steady state. The operating speed of 3500 rpm or 58 Hz is clearly visible, but exhibits a dip at about 5-10 s. The frequency corresponding to the first forward mode is 26 Hz. The component corresponding to 26 Hz is slowly increasing as a function of time. Still, it stays stable. At 3900 rpm, which is slightly above the predicted stability threshold speed of 3720 rpm, the displacement is shown in Figure 5.9. Both the components corresponding to 65 Hz, or 3900 rpm and 26 Hz are fluctuating as a function of time. Moreover, the 26 Hz components are more present. Although the behaviour at 3500 rpm and 3900 rpm is definitly unwanted and the vibration is quite high, stable operation is still possible, as there is no ever increasing amplitude. However, at 4000 rpm, a clear unstable phenomenon is occurring. The result is shown in Figure 5.10. In the short time of 4.15s the

amplitude is going from about 90 μm to 1.3 mm. Because of this short time, it is not possible to put these results in a waterfall plot. This amplification is exponential and is going towards a sinusoidal motion with a period of 0.038s (26.3 Hz). Higher amplitudes are not possible with this setup because the disk hits the edge of the frame. Everything suggests instability. The predicted stability threshold speed was thus 3720 rpm and there is clear instability at 4000 rpm. This means that there is only a small deviation of 7% in the prediction.

5.6 Conclusion

Based upon the energy in the modal model that is derived in section 5.2, the speed dependent part of the rotating damping is, although modelled as a stiffness term, dissipating energy. Therefore, in a measurement, the rotating damping can be seen as an speed dependent damping term. Moreover, the gyroscopic effect can be seen as a speed dependent mass term. As a concequence, an equivalent decay rate model is proposed. This unique model is experimentally friendly and yields the same results as the modal model, when the decay rate is concerned. Also, a procedure that indicates light damping of an experimental setup is presented. It is shown that light damping holds for the rotating damping setup. The measurement procedure which is proposed is based upon a gradual increase of the rotating speed an a monitoring of the decay rate. By doing this, combined with the assumed model, the stability threshold speed can be predicted while still ensuring safe operation. From the measured frequency response functions at different speeds, it is seen that the poles can easily be extracted and an equivalent single degree of freedom system can be fitted. The resulting decay rate plot predicts a stability threshold speed.

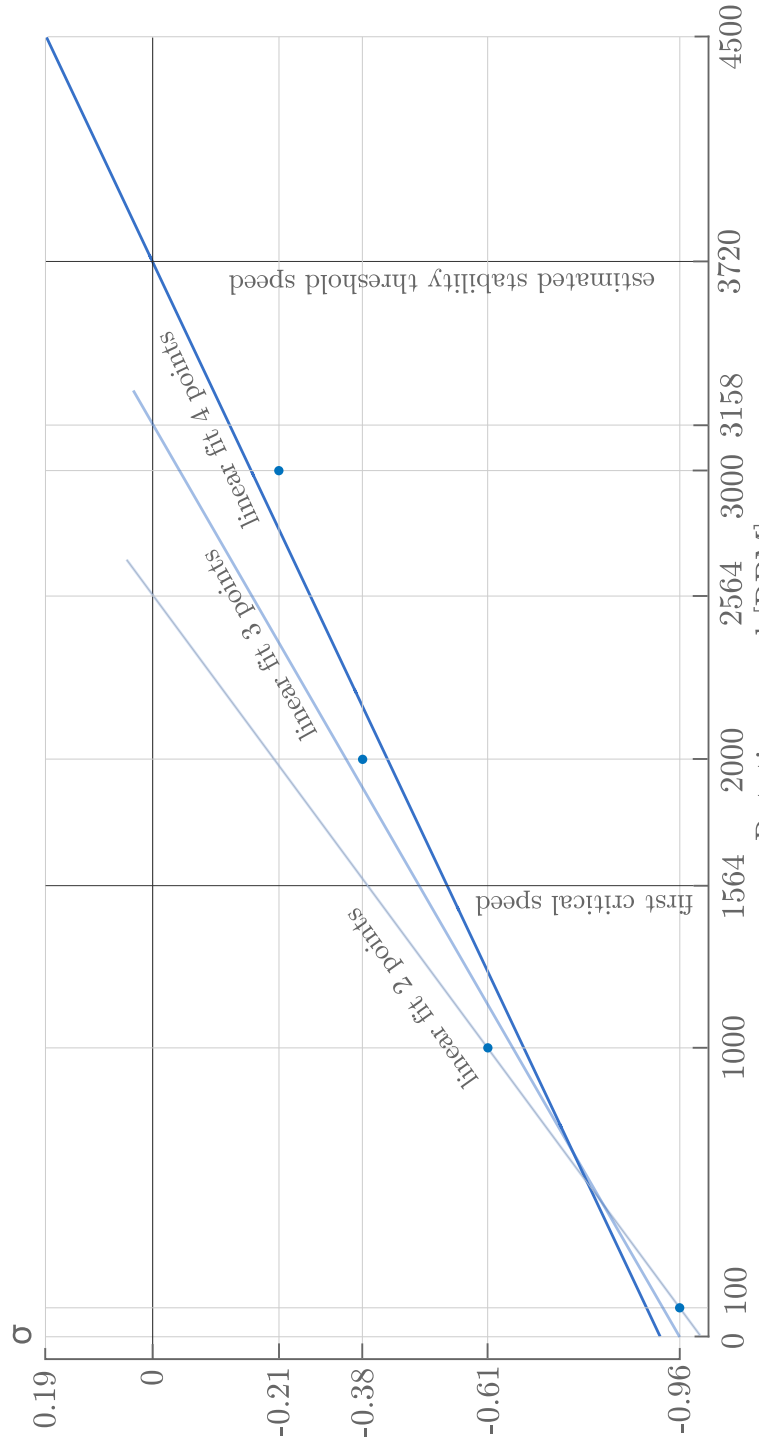

Figure 5.7: Measured, and predicted decay rate plot with a linear fit

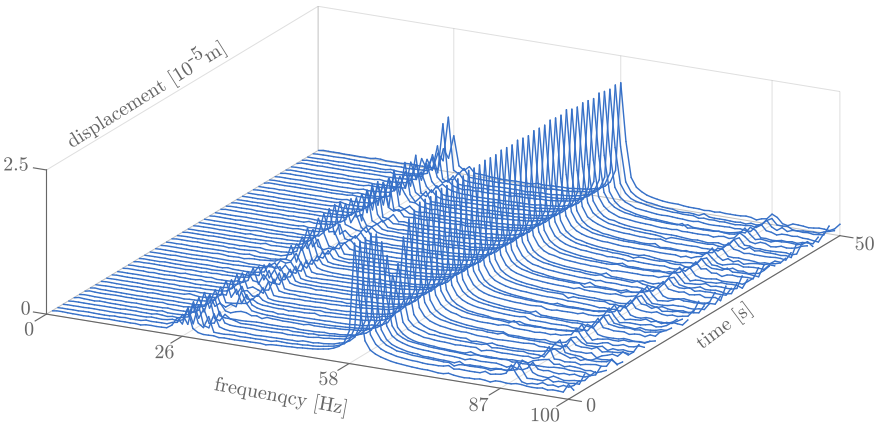

Figure 5.8: Waterfall plot of the steady state behaviour at 3500 rpm (58 Hz)

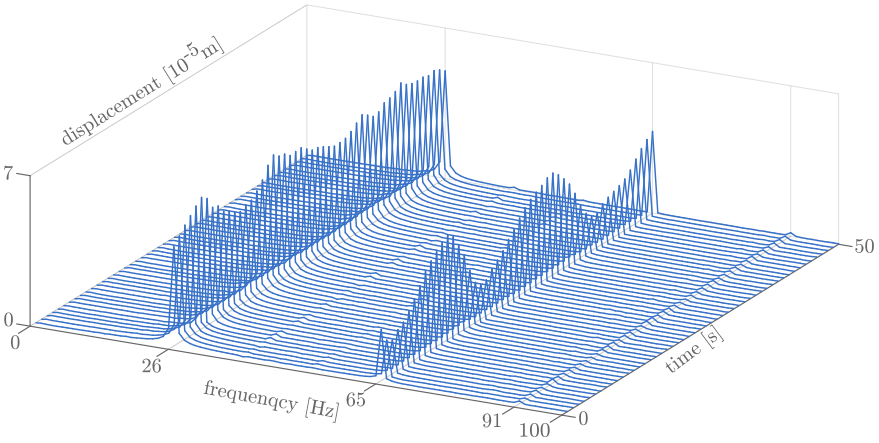

Figure 5.9: Waterfall plot of the steady state behaviour at 3900 rpm (65 Hz)

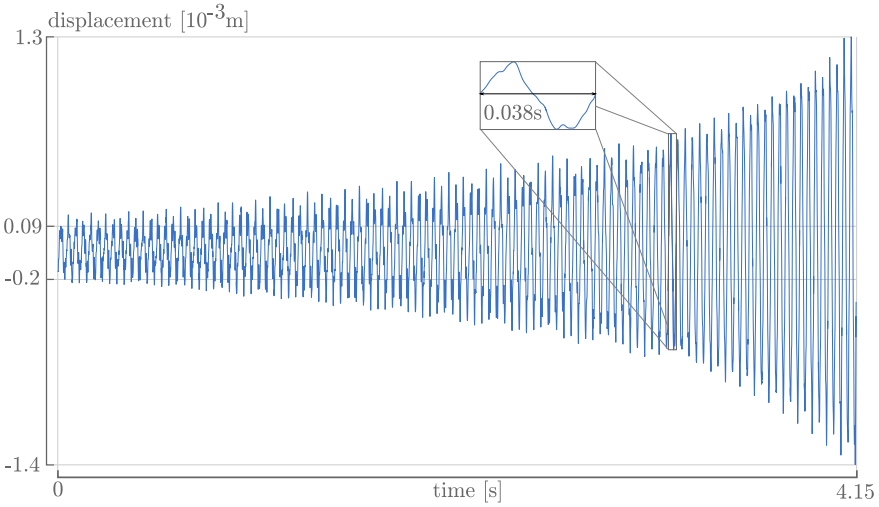

Figure 5.10: Shaft operated at 4000 rpm (67 Hz)

6 Damping matrix identification

6.1 Introduction

Although equally important as mass or stiffness, the experimental identification of damping is still not fully understood in literature. There are several reasons for this. Mass and stiffness are easily linked to materials, dimensions or connections. Damping as a physical phenomenon, however, involves all types of energy dissipation. This means that whenever mechanical energy is converted in another energy form, damping occurs. Damping may be inherent to a structure or material but can also be added deliberately to a mechanism to suppress unwanted vibrations. It can be due to friction with fluids, such as air or oil. Energy conversion through magnetic fields, or even acoustic noise is also accounted for as damping. Although these phenomena are known, in many cases the concept of *viscous damping* is used. Viscous damping describes a linear behaviour between the damping force and the velocity. It is easy to implement in linear models, but the only physical equivalence of viscous damping is the dashpot system. All the other types of damping exhibit different behaviour. Another widely used concept is *proportional damping*, a mathematical convenient way of modelling damping. This type of damping involves a relation between the damping matrix and the mass and stiffness matrix. In practise, however, damping is mostly located in links, joints or specific components. In spite of the lack of physical relevance viscous damping and proportional damping are very easy to use and yield, in many cases, a sufficient approximation of the actual behaviour. Therefore, it is common practise to fit vis-

cous models on measurements or to assume proportional damping. Consequently, these assumptions can be validated. Rotating damping is more difficult. As already described in chapter 2, it appears in both the damping matrix and the stiffness matrix. Moreover, it introduces asymmetry and speed dependency. Ideally, only the identification of the damping matrix, and even the stiffness matrix gives a clear insight in the actual behaviour. In this chapter, two existing straightforward damping matrix identification methods are described and modified towards rotating structures. Therefore, a novel equivalent model is proposed for which a measurement procedure is described. The damping identification methods, that are based upon eigenvalues and vectors are highly sensitive to errors. Additionally, a discussion follows how to deal with this errors, and how to optimize the methods.

6.2 Damping identification

Literature provides several identification techniques to estimate the damping matrix of linear structures. A good summery is made by Phani in [59]. Generally, the methods are divided into two types. *Matrix methods* are directly based on the frequency response function (FRF) matrix and *modal methods* are based on the modal parameters, particularly the poles and modeshapes, deduced from the FRF's. From an experimental point of view, a modal method is more interesting because the number of measurements can be highly reduced. Most experimental modal analysis methods do not need the whole FRF matrix to estimate the modal parameters. Lancaster [60] proposed a reconstruction method for symmetric underdamped systems with viscous damping. With the exact knowledge of the poles and eigenvectors, all the system matrices are reconstructed. Woodhouse and Adhikari [57] [61] suggest a technique that validates the preliminary assumption of viscous light damping, a conclusion based on the symmetry of the identified damping matrix. In a second contribution, Adhikari [62] proposes a method to extract nonviscous damping from measurements based on a general linear damping model. Both Lancaster's and Adhikari's method allow nonproportional damping and can deal with the spatial distribution of the damping matrix. This is highly advantageous in rotating machinery, because it can help to find the exact physical location of damping and gives an answer to the question where to add or even to reduce damping.
The modal methods of Lancaster [60] and Adhikari [61] require a specific scaling of the eigenvectors. Therefore, the eigenvector scaling is described in detail. When a mechanical system is undamped and not rotating, the equations of motion for a free response narrow down to

$$\mathbf{M}\ddot{\mathbf{q}} + \mathbf{K}\mathbf{q} = \mathbf{0} \tag{6.1}$$

with $\mathbf{M}$ symmetric positive definite and $\mathbf{K}$ symmetric, semi-definite. The corresponding, general right eigenvalue problem is

$$\left(\mathbf{M}\lambda_i^2 + \mathbf{K}\right)\boldsymbol{\psi}_i = \mathbf{0} \tag{6.2}$$

with λ_i an eigenvalue and $\boldsymbol{\psi}_i$ a right eigenvector. The right eigenvectors are arbitrarily scaled and combined in a matrix $\boldsymbol{\Psi} = [\boldsymbol{\psi}_1\ \boldsymbol{\psi}_2 \ldots \boldsymbol{\psi}_n]$ such that

$$\boldsymbol{\Psi}^T\mathbf{M}\boldsymbol{\Psi} = \mathbf{I}, \quad \boldsymbol{\Psi}^T\mathbf{K}\boldsymbol{\Psi} = -\boldsymbol{\Lambda} \tag{6.3}$$

$\boldsymbol{\Lambda}$ is a diagonal matrix containing the eigenvalues. This scaling method is referred to as *unity modal mass scaling* [2]. Now, suppose that there is damping present in the system

$$\mathbf{M}\ddot{\mathbf{q}} + \mathbf{C}\dot{\mathbf{q}} + \mathbf{K}\mathbf{q} = \mathbf{0} \tag{6.4}$$

and *modal coordinates* are defined such that $\mathbf{r} = \boldsymbol{\Psi}\mathbf{q}$ and (6.4) is premultiplied by $\boldsymbol{\Psi}^T$. Due to (6.3), this results in

$$\ddot{\mathbf{r}} + \boldsymbol{\Psi}^T\mathbf{C}\boldsymbol{\Psi} - \boldsymbol{\Lambda}\mathbf{r} = \mathbf{0} \tag{6.5}$$

Whenever the result of $\boldsymbol{\Psi}^T\mathbf{C}\boldsymbol{\Psi}$ is a diagonal matrix, equation (6.5) is decoupled into n differential equations, which can be solved separately. This mathematical convenience is called proportional damping and holds in its most general expression when [34]

$$\left(\mathbf{M}^{-1}\mathbf{C}\right)\left(\mathbf{M}^{-1}\mathbf{K}\right) = \left(\mathbf{M}^{-1}\mathbf{K}\right)\left(\mathbf{M}^{-1}\mathbf{C}\right) \tag{6.6}$$

and the most commonly used expression that holds this equation is

$$\mathbf{C} = a\mathbf{M} + b\mathbf{K} \tag{6.7}$$

with a and b arbitrary constants. It is important to notice that, although many types of damping can be approximated by proportional damping, this is does not describe the exact physical behaviour. In fact, both expressions (6.6) and (6.7) demand that there is a relation between the damping matrix and the mass and stiffness matrix. In real constructions, however, mass and stiffness are quite distributed whereas damping is often localized for instance as friction in joints. Although proportional damping is not physical, there is more then a mathematical convenience

to it. Due to the proportional damping, the eigenvectors that are related to the eigenvectors are real valued. This real value is a measure for the amplitude ratio between each generalized coordinate. This means that the eigenvectors are a physical representation of a *standing wave*, as all coordinates are in phase or antiphase. Whenever the damping is not proportional, the eigenvectors become complex valued. This complex value is the result of a phase difference between the generalized coordinates, if the system vibrates according to a single mode. In fact, this is a physical representation of a *travelling wave*. A standing wave is more intelligible and easier to visualize. Unity modal mass scaled real eigenvectors are also the result of a straightforward expression involving mass and stiffness. The eigenvectors are scaled towards a physical mass matrix. Several authors proposed methods to extract real modes from complex valued modes [63] [64] [65]. Still, many significant errors occur when approximating the complex eigenvectors by real modes. For nonproportional damping, a state-space representation is needed and the eigenvectors are more easily scaled towards *unity modal A*. For symmetric matrices this means

$$\tilde{\mathbf{\Psi}}^T \mathbf{A} \tilde{\mathbf{\Psi}} = \mathbf{I} \tag{6.8}$$

with $\mathbf{A}$

$$\mathbf{A} = \begin{bmatrix} \mathbf{C} & \mathbf{M} \\ \mathbf{M} & \mathbf{0} \end{bmatrix} \tag{6.9}$$

6.2.1 Lancaster's reconstruction method extended

One of the most comprehensive methods to reconstruct the damping matrix from the modal parameters is Lancaster's method as first described in [60]. Foltête [66] calls it Danek's reconstruction, referring to a Czech paper [67]. The description of Lancaster is based upon symmetric systems, where left and right eigenvectors are equal. However, here, this line of thought is extended towards rotating systems. By representing the model in state space and chosing the right scaling as is done in equation (2.52) and (2.56). By using

$$\mathbf{A} = \begin{bmatrix} \mathbf{C} & \mathbf{M} \\ \mathbf{M} & \mathbf{0} \end{bmatrix} \quad ; \quad \mathbf{B} = \begin{bmatrix} \mathbf{K} & \mathbf{0} \\ \mathbf{0} & -\mathbf{M} \end{bmatrix} \tag{6.10}$$

and unity model A scaling

$$\tilde{\mathbf{\Phi}}^T \mathbf{A} \tilde{\mathbf{\Psi}} = \mathbf{I} \tag{6.11}$$

thus

$$\tilde{\mathbf{\Phi}}^T \mathbf{B} \tilde{\mathbf{\Psi}} = -\tilde{\mathbf{\Lambda}} \tag{6.12}$$

with the left eigenvectors, $\tilde{\boldsymbol{\phi}}$ and right eigenvectors $\tilde{\boldsymbol{\psi}}$

$$\tilde{\mathbf{\Phi}} = \begin{bmatrix} \tilde{\boldsymbol{\phi}}_1 & \tilde{\boldsymbol{\phi}}_2 & \dots & \tilde{\boldsymbol{\phi}}_n \end{bmatrix} \quad ; \quad \tilde{\mathbf{\Psi}} = \begin{bmatrix} \tilde{\boldsymbol{\psi}}_1 & \tilde{\boldsymbol{\psi}}_2 & \dots & \tilde{\boldsymbol{\psi}}_n \end{bmatrix} \tag{6.13}$$

note that **C** and **K** are speed dependent, but invariable at a constant speed. Now, arrange the eigenvalues and eigenvectors such that

$$\tilde{\mathbf{\Psi}} = \begin{bmatrix} \mathbf{\Psi} & \overline{\mathbf{\Psi}} \\ \mathbf{\Psi\Lambda} & \overline{\mathbf{\Psi\Lambda}} \end{bmatrix} \quad ; \quad \tilde{\mathbf{\Phi}} = \begin{bmatrix} \mathbf{\Phi} & \overline{\mathbf{\Phi}} \\ \mathbf{\Phi\Lambda} & \overline{\mathbf{\Phi\Lambda}} \end{bmatrix} \quad \text{and} \quad \tilde{\mathbf{\Lambda}} = \begin{bmatrix} \mathbf{\Lambda} & \mathbf{0} \\ \mathbf{0} & \overline{\mathbf{\Lambda}} \end{bmatrix} \tag{6.14}$$

where $\bar{\cdot}$ means the complex conjugate. (6.11) and (6.12) are rewritten as

$$\mathbf{A}^{-1} = \tilde{\mathbf{\Psi}} \tilde{\mathbf{\Phi}}^T \tag{6.15}$$

and

$$\mathbf{B}^{-1} = -\tilde{\mathbf{\Psi}} \tilde{\mathbf{\Lambda}}^{-1} \tilde{\mathbf{\Phi}}^T \tag{6.16}$$

$\mathbf{A}^{-1}$ and $\mathbf{B}^{-1}$ are block matrices so block inversion results in

$$\begin{bmatrix} \mathbf{C} & \mathbf{M} \\ \mathbf{M} & \mathbf{0} \end{bmatrix}^{-1} = \begin{bmatrix} \mathbf{0} & \mathbf{M}^{-1} \\ \mathbf{M}^{-1} & -\mathbf{M}^{-1}\mathbf{C}\mathbf{M}^{-1} \end{bmatrix} = \begin{bmatrix} \mathbf{\Psi} & \overline{\mathbf{\Psi}} \\ \mathbf{\Psi\Lambda} & \overline{\mathbf{\Psi\Lambda}} \end{bmatrix} \begin{bmatrix} \mathbf{\Phi} & \overline{\mathbf{\Phi}} \\ \mathbf{\Phi\Lambda} & \overline{\mathbf{\Phi\Lambda}} \end{bmatrix}^T \tag{6.17}$$

$$\begin{bmatrix} \mathbf{K} & \mathbf{0} \\ \mathbf{0} & -\mathbf{M} \end{bmatrix}^{-1} = \begin{bmatrix} \mathbf{K}^{-1} & \mathbf{0} \\ \mathbf{0} & -\mathbf{M}^{-1} \end{bmatrix} = - \begin{bmatrix} \mathbf{\Psi} & \overline{\mathbf{\Psi}} \\ \mathbf{\Psi\Lambda} & \overline{\mathbf{\Psi\Lambda}} \end{bmatrix} \begin{bmatrix} \mathbf{\Lambda}^{-1} & \mathbf{0} \\ \mathbf{0} & \overline{\mathbf{\Lambda}}^{-1} \end{bmatrix} \begin{bmatrix} \mathbf{\Phi} & \overline{\mathbf{\Phi}} \\ \mathbf{\Phi\Lambda} & \overline{\mathbf{\Phi\Lambda}} \end{bmatrix}^T \tag{6.18}$$

from which

$$\mathbf{M}^{-1} = \mathbf{\Psi\Lambda\Phi}^T + \overline{\mathbf{\Psi\Lambda\Phi}^T} = 2Re(\mathbf{\Psi\Lambda\Phi}^T) \tag{6.19}$$

$$-\mathbf{K}^{-1} = 2Re\left(\mathbf{\Psi\Lambda}^{-1}\mathbf{\Phi}^T\right) \tag{6.20}$$

$$\mathbf{C} = -2\mathbf{M}\left(\mathbf{\Psi\Lambda}^2\mathbf{\Phi}^T\right)\mathbf{M} \tag{6.21}$$

$$\mathbf{0} = Re\left(\mathbf{\Psi\Phi}^T\right) \tag{6.22}$$

The four expressions demonstrate that, in theory, it is possible to reconstruct mass, stiffness and damping matrix when the eigenvalues and eigenvectors of the system are known. Moreover, (6.22) defines an extra condition which has to be fulfilled. The latter is known as the *properness condition* and is very useful. It expresses a condition that has to be true for the eigenvectors in order for the assumed model to hold. It can be used to optimize measured eigenvectors [63]. It can easily be seen that for symmetric systems, where left and right eigenvectors are the same, the equations also hold. Although this method is very straightforward, it is not easy to apply in practise. The extraction of left and right eigenvectors from measurements requires at least one row and column of the frequency response function matrix. This implies that all measurement points need to be attainable for both excitation and measurement.

6.2.2 Adhikari's method

Adhikari's method, as described in a series of papers [61] [62] [68] [69] is based upon an approximate solution of the equations of motion of non-rotating system

$$\mathbf{M}\ddot{\mathbf{q}} + \mathbf{C}\dot{\mathbf{q}} + \mathbf{K}\mathbf{q} = \mathbf{0} \tag{6.23}$$

or, described as a quadratic eigenvalue problem

$$\left(-\lambda_j^2\mathbf{M} + i\lambda_j\mathbf{C} + \mathbf{K}\right)\boldsymbol{\psi}_j = \mathbf{0} \tag{6.24}$$

for λ_j an eigenvalue and $\boldsymbol{\psi}_j$ a right eigenvector. Adhikari tries to find an answer on the question whether to use a viscous or non-viscous damping and if it is possible to find the correct spatial distribution of the damping matrix. The latter is interesting in rotating machinery, because it leads to insights into the distribution of non-rotating damping and rotating damping. However, it should be emphasized that the method is designed for non-rotating systems. Although it allows asymmetry of the damping matrix, mass and stiffness are supposed to be symmetric. Nevertheless, it is interesting to take a closer look at the method and to describe the usefulness in rotating machinery. Recall (6.1) and the eigenvalue problem (6.2). The eigenvalues λ are related to the undamped natural frequencies. The unity modal mass scaled eigenvectors are real. Now, for slight damping, the entries of the $\mathbf{C}$ matrix are small. The eigenvectors are complex valued, but they remain close to the real, undamped eigenvectors.

$$\boldsymbol{\psi}_{dj} = \sum_{l=1}^{N} \alpha_l^{(j)} \boldsymbol{\psi}_{ul} \quad \text{where } \alpha_j^{(j)} = 1 \quad \text{and} \quad \left|\alpha_l^{(j)}\right| \ll 1 \; \forall l \neq j \tag{6.25}$$

where $\boldsymbol{\psi}_d$ is an damped eigenvector, written as a linear combination of the undamped eigenvectors $\boldsymbol{\psi}_u$. This actually means that the imaginary part of the eigenvectors is mainly affected by the damping. The procedure to estimate the damping matrix is described as follows in [61], the notations also correspond the the ones described by Adhikari.

1. Measure a set of transfer functions $H_{ij}(\omega)$
2. Choose the number m of modes to be retained in the study. Determine the complex natural frequencies $\hat{\lambda}_j$ and complex eigenvectors $\hat{\boldsymbol{\psi}}_{dj}$ from the transfer functions, for all $j = 1, \ldots, m$. Obtain the complex mode shape matrix $\hat{\boldsymbol{\Psi}} = \left[\hat{\boldsymbol{\psi}}_{d1}, \hat{\boldsymbol{\psi}}_{d2}, \ldots, \hat{\boldsymbol{\psi}}_{dm}\right] \in \mathbb{C}^{N \times m}$
3. Estimate the "undamped natural frequencies "as $\hat{\omega}_j = \Re(\hat{\lambda}_j)$
4. Set $\mathbf{U} = \Re\left[\hat{\boldsymbol{\Psi}}\right]$ and $\hat{\mathbf{V}} = \Im\left[\hat{\boldsymbol{\Psi}}\right]$, and from these obtain $\mathbf{W} = \hat{\mathbf{U}}^T\hat{\mathbf{U}}$ and $\mathbf{S} = \hat{\mathbf{U}}^T\hat{\mathbf{V}}$. Now denote $\mathbf{B} = \mathbf{W}^{-1}\mathbf{S}$.
5. From the **B** matrix get $C'_{kj} = (\hat{\omega}_j^2 - \hat{\omega}_k^2)B_{kj}/\hat{\omega}_j$ for $k \neq j$ and $C'_{jj} = 2\Im(\hat{\lambda}_j)$.
6. Finally, carry out the transformation $\mathbf{C} = \left[\left(\hat{\mathbf{U}}^T\hat{\mathbf{U}}\right)^{-1}\hat{\mathbf{U}}^T\right]^T \mathbf{C}' \left[\left(\hat{\mathbf{U}}^T\hat{\mathbf{U}}\right)^{-1}\hat{\mathbf{U}}^T\right]$ to get the damping matrix in physical coordinates.

6.3 Equivalent decay rate model for multiple degree of freedom rotating systems

One of the main difficulties concerning the experimentation on a rotor is the fact that the system is rotating. It is not the actual rotating motion that is the main difficulty, because this is overcome by choosing the right actuators and sensors. It is the difference between a rotating system and a non-rotating system that has to be dealt with. Within this research this implies mainly the rotating damping, but also the gyroscopic effect. These effects cause anomalies that are generally not present in non-rotating systems. In chapter 5, it is shown that the energy in a rotating system has a specific behaviour. In the modal model, this means that the gyroscopic effect, can be seen as an speed dependent effect on the mass and that the rotating damping, appearing in the stiffness term has a speed dependent effect on the damping. This actually means that the observer is blind for the anomalies that arise from the rotating setup. In other words, the rotor is observed as a non-rotating system. The gyroscopic effect acts as an apparent mass and the rotating

damping acts as an apparent damping. The new representation of the equivalent decay rate model is:

$$(\mathbf{M} - \Omega\mathbf{G}_2)\,\ddot{\mathbf{q}} + (\mathbf{C}_1 - \Omega\mathbf{C}_2)\,\dot{\mathbf{q}} + \mathbf{K}\mathbf{q} = \mathbf{0} \tag{6.26}$$

The modal model corresponding to this is (5.10). This model also yields equivalent decay rates. Remark that also here, only forward modes are concerned, as only these modes are sensitive to instability. By assuming such a model, a regular damping identification method, such as Lancaster or Adhikari, can be applied at a constant speed.

6.4 Example

As an example, a plain rotating shaft is used. A finite element model is constructed as described in chapter 2. Everything is done in simulation as a proof of concept. The experiments are discussed later on. The shaft, divided in six elements is shown in Figure 6.1. The parameters for the shaft are listed in Table 6.1. The shaft parameters resemble the rotating damping setup. The bearing parameters are tuned with a trial and error procedure to yield realistic results. The material damping of the shaft is chosen proportional to the stiffness of the shaft. However, because the damping matrix also contains the damping of the bearings, the damping is eventually not proportional. Six elements lead to 7 nodes, with each 4 degrees of freedom. The model has thus 28 degrees of freedom. In order to get a clear visualization of the system matrices, a 3D representation is used, where the values of the matrix elements are plotted as a function of the rows and columns. The mass matrix, as modeled is shown in Figure 6.2. This matrix is very sparse and the mass is quite distributed upon the diagonal. The modeled damping and stiffness matrix are shown in Figure 6.3 and 6.4. The gyroscopic matrix and rotating damping matrix are skew symmetric and shown in Figure 6.6 and 6.5. The gyroscopic effect is very low and almost negligible, because there are no disks involved. In this example, two procedures for damping matrix identification are described. First, Lancaster's method, with left and right eigenvectors is used. Second, Adhikari's method is used in combination with the equivalent decay rate model for multiple degree of freedom rotating systems.

Diameter $[m]$	0.01
Length $[m]$	1.115
Young modulus $[N/m^2]$	2x10^{11}
Density $[kg/m^3]$	7730
Proportional damping factor shaft $[N/m]$	4.3x10^{-5}
Translational stiffness bearings $[N/m]$	5.60x10^{7}
Rotational stiffness bearings $[N/m]$	4.50x10^{2}
Translational damping bearings $[Ns/m]$	0.041
Rotational damping bearings $[Ns/m]$	0.041

Table 6.1: Parameters used in the example

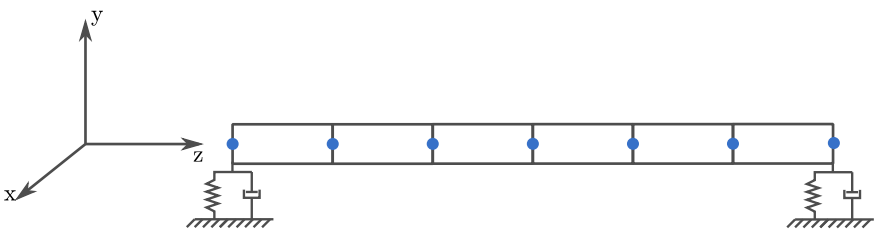

Figure 6.1: Schematic representation of the used finite element model

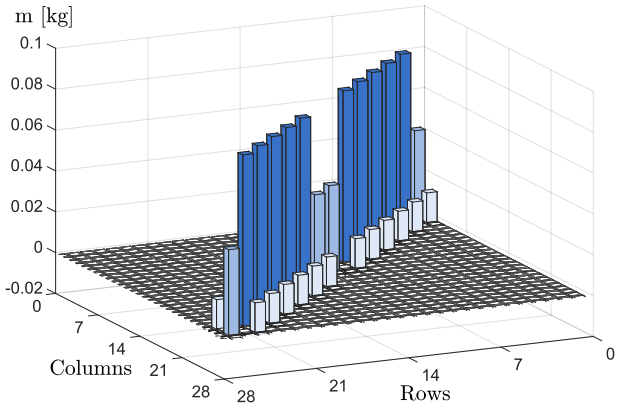

Figure 6.2: 3D representation of the mass matrix as modeled

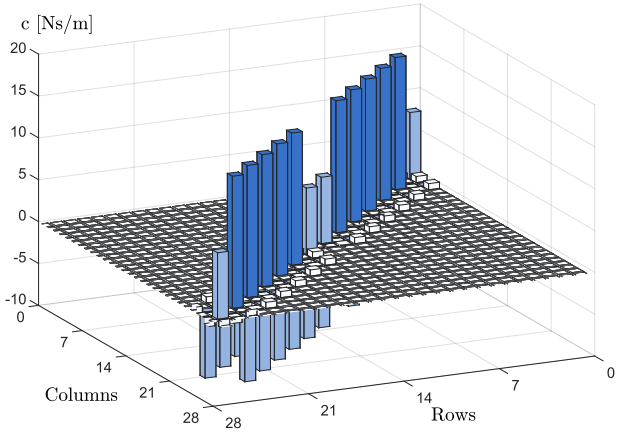

Figure 6.3: 3D representation of the damping matrix as modeled

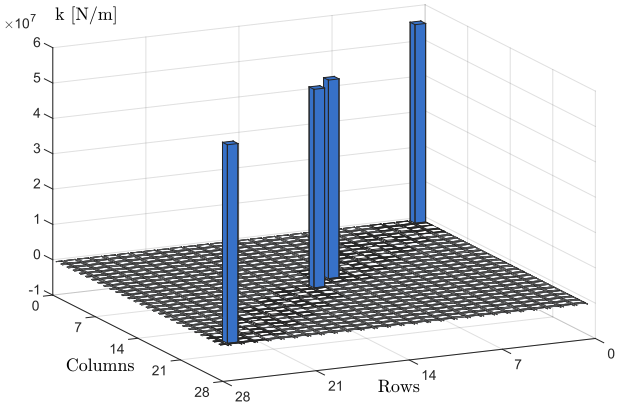

Figure 6.4: 3D representation of the stiffness matrix as modeled

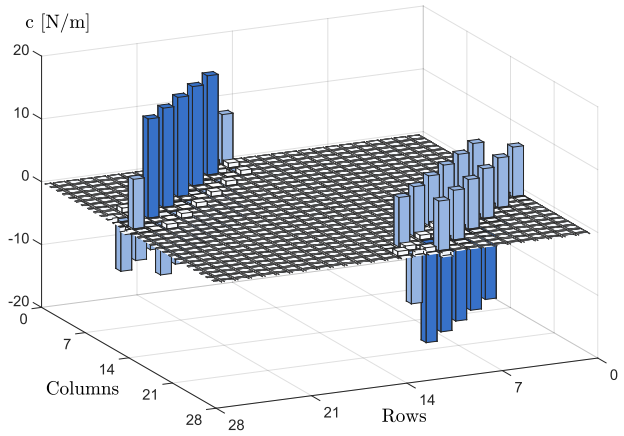

Figure 6.5: 3D representation of the rotating damping matrix as modeled

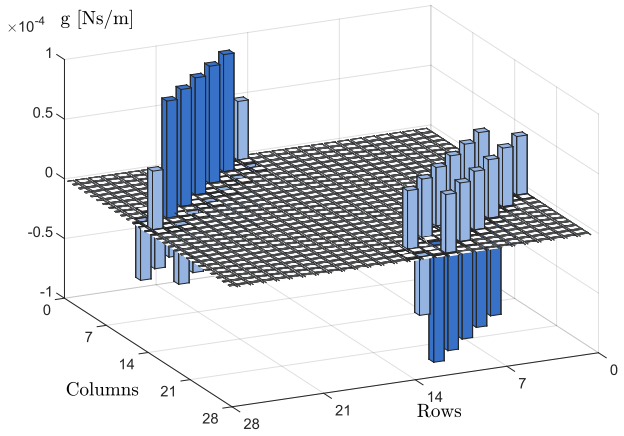

Figure 6.6: 3D representation of the gyroscopic matrix as modeled

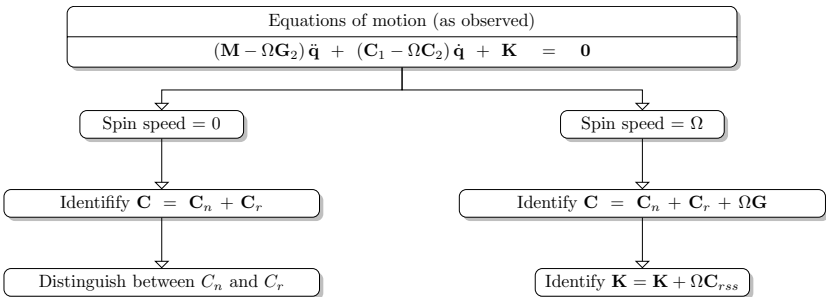

Figure 6.7: Procedure to estimate the rotating damping matrix and the gyroscopic matrix

6.4.1 Lancaster's method extended

Lancaster's method is easily implemented in simulation by calculating eigenvalues and eigenvectors and using the correct scaling (6.11). (6.20-6.21) result in the stiffness and damping matrix, and is applicable on asymmetric systems. It gives the exact solutions, even when rotating. The procedure is visualized in Figure 6.7. Lancaster's method allows an estimation without adjusting the equations of motion. The difference between the damping matrix at 200 rad/s and 0 rad/s is shown in Figure 6.8. By dividing this result by Ω, the exact solution for the gyroscopic matrix is obtained. The same is done for the difference between the stiffness matrix at 200 rad/s and 0 rad/s, shown in Figure 6.9. The resulting matrix is the rotating damping matrix multiplied by the spin speed Ω. Although very promising, these results are simulated results. The eigenvectors, both left- and right, are easily calculated, all degrees of freedom are incorporated and the errors on the results are limited to numerical errors.

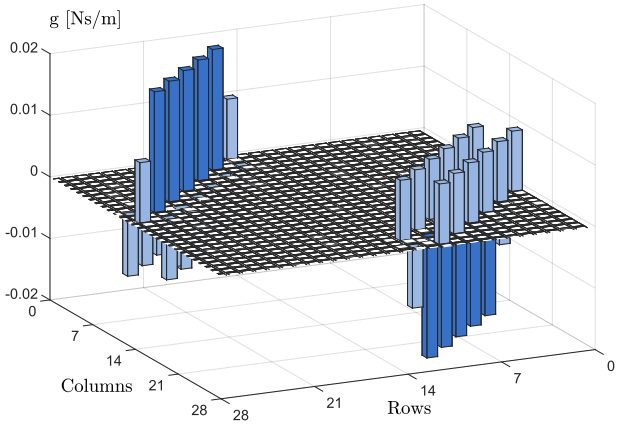

Figure 6.8: 3D representation of the difference between damping matrix at 200 rad/s and 0 rpm with Lancaster's method. This illustrates the gyroscopic effect.

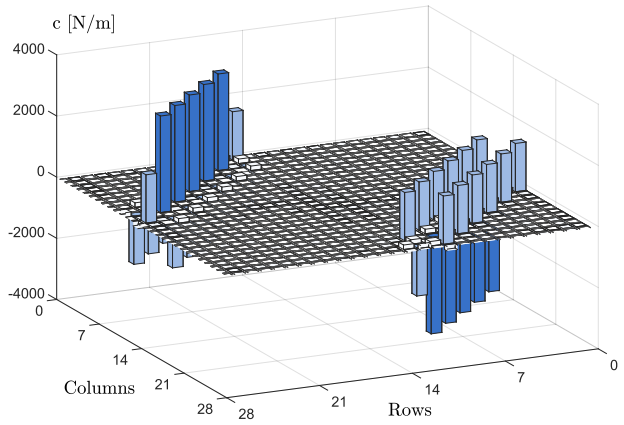

Figure 6.9: 3D representation of the difference between stiffness matrix at 200 rad/s and 0 rad/s with Lancaster's method. This illustrates the rotating damping

6.4.2 Adhikari's method

Adhikari's method is designed for non-rotating systems. Therefore, the method can only be used by observing the system as a non-rotating system. This unique point of view is described in section 6.3 and equation (6.26) this is possible by observing only one direction of the coordinates, in this case the x-direction. From Figure 6.11, the original rotating damping matrix, corresponding to the x-direction is visualized in Figure 6.11. The procedure that is used is shown in Figure 6.10. Using Adhikari's method at both 0 and 200 rad/s, and extracting both leads to the result in Figure 6.12. Although there is a difference in amplitude, which is expected, the spatial distribution is similar. Note that the matrix in Figure 6.11 is a part of the stiffness matrix and 6.12 is a part of the damping matrix. This means that the observation of the rotating system as a non-rotating system indeed yields a similar model as described in section 6.3. In order to exclude that an equal distribution of the damping is causing this effect, a local damping of 60 Ns/m is added in the middle of the shaft. The resulting identified matrix with Adhikari's method is shown in Figure 6.13. It is seen that the local damping in the middle is identified from the spatial distribution.

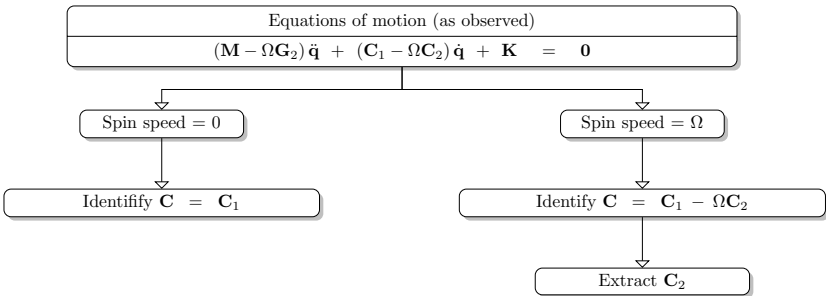

Figure 6.10: Procedure to estimate the rotating damping matrix and the gyroscopic matrix

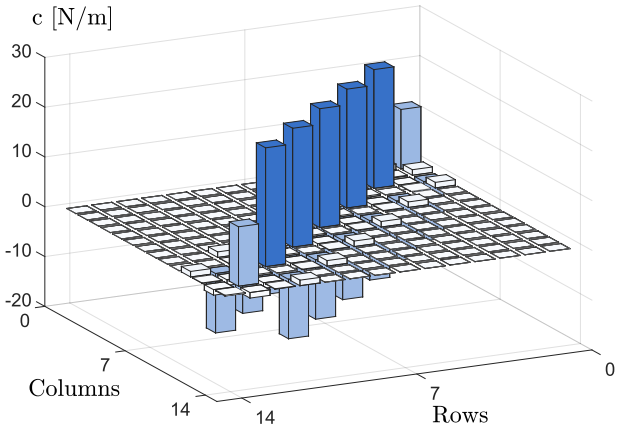

Figure 6.11: 3D representation of the original rotating damping matrix for x-direction

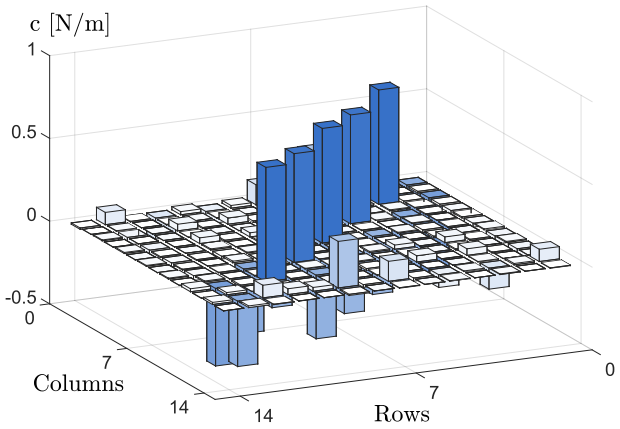

Figure 6.12: 3D representation of the difference between damping matrix at 200 rad/s and 0 rad/s with Adhikari's method

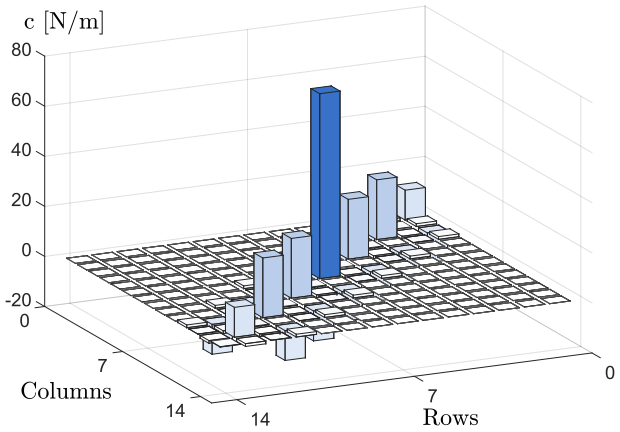

Figure 6.13: 3D representation of the original rotating damping matrix for x-direction with local damping in the middle

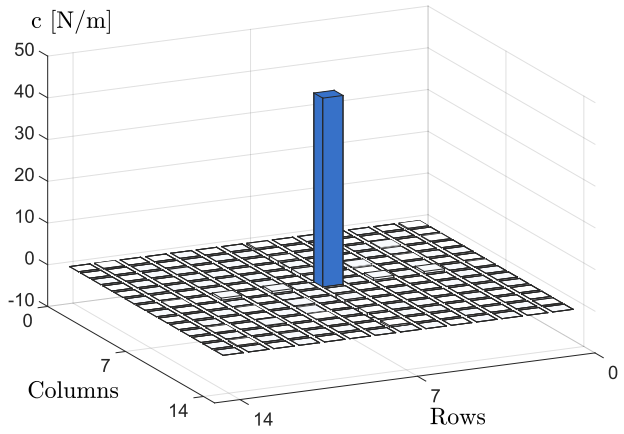

Figure 6.14: 3D representation of the difference between damping matrix at 200 rad/s and 0 rpm

6.5 Errors and optimization of the eigenvectors

In practise, the extracted eigenvectors are erroneous and affect the identified damping matrix. Typically, noise on the measurement leads to errors but also limitations in frequency resolution lead to bias errors on the FRF. Besides these errors that can be dealt with by performing a good experiment, there still exists a major error: the assumed model. The preliminary assumption of a discrete linear time invariant model is a good approximation but is never entirely correct. There are two strategies to deal with this error. Either looking for the exact physical behaviour, which leads to complex mathematical descriptions, or forcing the measurements to fit the assumed model. The latter is useful when trends are more of interest rather than physical behaviour. For instance, if damping location is more important than the actual absolute values of the system parameters. Three of these optimization techniques are described below: Adhikari's symmetry preserving method, optimization with iterative procedure and optimization with properness condition.

6.5.1 Adhikari's symmetry preserving method

With Adhikari's method, an asymmetric matrix indicates that the proposed damping model is incorrect. However, in some cases a numerical and experimental study shows that the identified damping matrix becomes asymmetric although a symmetric damping matrix was expected [70] [71]. Therefore, another method that forces the damping matrix to be symmetric is used. The procedure is described as follows in [69]

1. Measure a set of transfer functions $H_{ij}(\omega)$ at a set of N grid points. Fix

the number of the modes to be retained in the study, say m. Determine the complex natural frequencies $\hat{\lambda}_j$ and the complex eigenvectors $\hat{\mathbf{z}}_j$ from the transfer functions, for all $j = 1, \ldots, m$. Denote by $\hat{\mathbf{Z}} = [\hat{\mathbf{z}}_1, \hat{\mathbf{z}}_2, \ldots, \hat{\mathbf{z}}_m] \in \mathbb{C}^{N \times m}$ the complex mode shape matrix.

2. Set the "undamped natural frequencies"as $\hat{\omega_j} = \Re(\hat{\lambda}_j)$. Denote the diagonal matrix $\hat{\mathbf{\Omega}} = diag\,(\hat{\omega_1}, \hat{\omega_2}, \ldots, \hat{\omega_m}) \in \mathbb{R}^{m \times m}$

3. Separate the real and imaginary parts of $\hat{\mathbf{Z}}$ to obtain $\hat{\mathbf{U}} = \Re\left[\hat{\mathbf{Z}}\right]$ and $\hat{\mathbf{V}} = \Im\left[\hat{\mathbf{Z}}\right]$

4. From these obtain the $m \times m$ matrices $\mathbf{W} = \hat{\mathbf{U}}^T\hat{\mathbf{U}}$, $\mathbf{D} = \hat{\mathbf{U}}^T\hat{\mathbf{V}}$, $\mathbf{Q} = \hat{\mathbf{\Omega}}^{-1}\hat{\mathbf{W}}$ and $\mathbf{P} = \hat{\mathbf{\Omega}}^{-1}\mathbf{D}\hat{\mathbf{\Omega}} - \mathbf{D}^T$

5. Now denote $\mathbf{p} = vec(\mathbf{P}) \in \mathbb{R}^{m^2}$ and calculate $\mathbf{R} = (\mathbf{\Omega} \otimes \mathbf{Q}) + \left(\mathbf{Q} \otimes \hat{\mathbf{\Omega}}\right) \in \mathbb{R}^{m^2 \times m^2}$

6. Evaluate $vec(\mathbf{B}) = [\mathbf{R}]^{-1}\,\mathbf{p}$ and obtain the matrix $\mathbf{B}$.

7. From the $\mathbf{B}$ matrix obtain $\mathbf{C}' = \mathbf{B}\hat{\mathbf{\Omega}} - \hat{\mathbf{\Omega}}\mathbf{B}\mathbf{\Omega}^{-1}$ and $C'_{jj} = 2\Im(\hat{\lambda_j})$.

8. Finally, carry out the transformation $\mathbf{C} = \left[\left(\hat{\mathbf{U}}^T\hat{\mathbf{U}}\right)^{-1}\hat{\mathbf{U}}^T\right]^T \mathbf{C}' \left[\left(\hat{\mathbf{U}}^T\hat{\mathbf{U}}\right)^{-1}\hat{\mathbf{U}}^T\right]$ to get the damping matrix in physical coordinates.

The operation vec is defined as a transformation from a matrix to a vector by stacking the columns in a sequence one below another or $vec : \mathbb{R}^{m \times n} \rightarrow \mathbb{R}^{mn}$ and $\otimes$ is the Kronecker product. This symmetry preserving method has the advantage that the resulting symmetric matrix is easy to interpret. Yet, by forcing the damping matrix to be symmetric, physical phenomena are masked. When the physical damping matrix is asymmetric, a large error is made. Moreover the force of Adhikari's method lies in the ability to decide whether the assumed viscous damping model was correct and this interpretation is lost by forcing symmetry. However, if the errors on the identified eigenvectors are the main reason for the asymmetry, this method is the better alternative. But generally, this information is initially not known.

6.5.2 Optimization with iterative procedure

The unity modal A scaling needed for Lancaster's reconstrution can be used to optimize the eigenvectors such that a better estimation of the damping matrix is obtained. If the mass matrix is known, for instance from a lumped mass or a finite

element model, and an initial guess of the damping matrix is available, an iterative procedure can be used. By normalizing the eigenvectors such that

$$\boldsymbol{\psi}_i^T \left(2\mathbf{M}_0\lambda_i + \mathbf{C}_0\right)\boldsymbol{\psi}_i = 1 \tag{6.27}$$

with $\mathbf{M}_0$ and $\mathbf{C}_0$ the initial mass and damping. With the new scaling of $\boldsymbol{\psi}_i$ a new damping matrix can be reconstructed. By using this damping matrix again to rescale the eigenvectors, an iterative procedure is formed as described in Figure 6.15 [3].

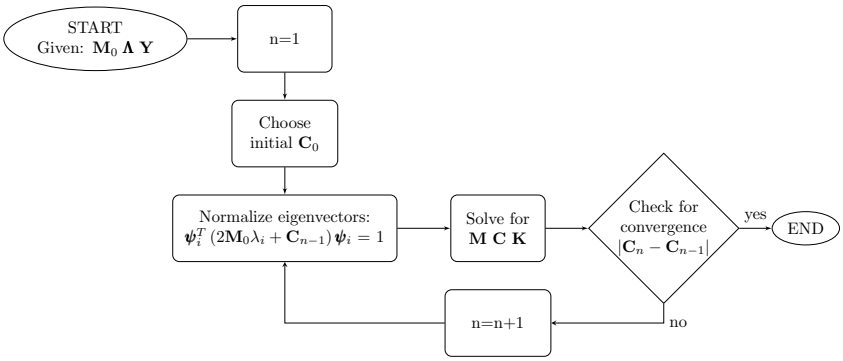

Figure 6.15: Optimization of the eigenvectors with iterative procedure [3]

The main drawback of this method is that a good approximation of the mass matrix is required. Current finite element procedures can provide this mass matrix quite accurately and by using a model reduction technique the numerous degrees of freedom can be reduced to the ones of interest. On the other hand, this scaling does not eliminate the error but rescales the eigenvectors to better fit the model.

6.5.3 Optimization with properness condition

Lancaster's reconstruction results besides the system matrices in what is called a properness condition in [63]. If this orthogonality condition is not fulfilled, it means that the identified eigenvectors are no solution of the assumed model. When left and right eigenvectors are equal, or in other words, in the *case of symmetric systems*, the properness condition can be used to optimize the eigenvectors Suppose a set of complex conjugate eigenvectors $\mathbf{E} = \left[\boldsymbol{\Psi}\overline{\boldsymbol{\Psi}}\right]$. If these eigenvectors do not meet the properness condition, they do not meet the assumed model. It would be better to find an approximation of $\tilde{\mathbf{E}}$ with an enforced properness condition. In order to find these eigenvectors, the quadratic norm J has to be minimized

$$J = \sum_{i,j} \overline{\Delta E_{i,j}} \Delta E_{i,j} \quad \text{with} \quad \Delta \mathbf{E} = \tilde{\mathbf{E}} - \mathbf{E} \tag{6.28}$$

where $\tilde{\mathbf{E}}$ is the closest set of eigenvectors that does fulfill the properness condition. A solution of the problem is

$$\tilde{\mathbf{E}} = \mathbf{E} + \boldsymbol{\delta}\mathbf{E} = \left(\mathbf{I} - \boldsymbol{\delta}\bar{\boldsymbol{\delta}}\right)^{-1} \left(\mathbf{E} - \boldsymbol{\delta}\overline{\mathbf{E}}\right) \tag{6.29}$$

where $\boldsymbol{\delta}$ is the solution of the Riccati equation

$$\mathbf{E}\mathbf{E}^T - \boldsymbol{\delta}\overline{\mathbf{E}}\mathbf{E}^T - \mathbf{E}\overline{\mathbf{E}}^T\boldsymbol{\delta} + \boldsymbol{\delta}\overline{\mathbf{E}\mathbf{E}}^T\boldsymbol{\delta} = 0 \tag{6.30}$$

which can be solved for δ. The resulting eigenvectors are close to the identified eigenvectors but meet the properness condition better. These eigenvectors can be used in Lancaster's reconstruction, or even rescaled to modal mass in Adhikari's method to determine the damping matrix.

6.5.4 Comparison between optimization methods

The three proposed optimization method each have some advantages and disadvantages. The methods are compared in Table 6.2. The masking of the asymmetry is an important drawback. For both the symmetry preserving method and the iterative procedure, this masking is placed high. The symmetry preserving method forces symmetry, and the iterative procedure rescales the eigenvectors to yield a symmetric matrix. The optimization by properness condition does nothing like that, however, the derivation of this condition is also based upon symmetric matrices. That is why the masking is set to medium. For the iterative procedure, there needs to be some preliminary knowledge on the mass matrix and a proposal for the damping matrix. However, if this is known exactly from the model, this could be an advantage. Both symmetry preserving method and optimization by properness condition do not need preliminary knowledge.

6.6 Model incompleteness and truncation

In theory, most damping estimation techniques assume preliminary that all generalized coordinates can be measured. In fact, it is reasonable that in order to get a good spatial distribution of the damping matrix, at least these places have to be measured. However, in practise, measuring all coordinates is unrealistic. A shaft is

	Symmetry preserving method	**Iterative procedure**	**Properness condition**
Principle	Assume symmetry	Rescaling	Condition that results from the Lancaster
Preliminary knowledge	None	Mass and proposal for damping	None
Masking of asymmetry	High	High	Medium

Table 6.2: Comparison between the different optimization methods

for instance a continuum, so the degrees of freedom are theoretically infinite. Besides, dependening on the setup, certain coordinates cannot be reached physically. Moreover, translations are easy to measure, but rotations are very difficult. All these factors result in what is called *model incompleteness*. There is no absolute rule that determines how many degrees of freedom have to be taken into account to get a realistic estimation as it really depends upon the setup and on the desired dimensions of the damping matrix.
Furthermore, measurements also suffer from *model trunctation*. This means that, in practise the frequency band is limited. Continuous systems have an infinite number of resonant frequencies. The sensors, the actuators for excitation and the data-acquisition all have a limited bandwidth. This means that the highest measurable frequency, or corresponding eigenvector is limited by the hardware. The effect of model incompleteness and truncation on the damping identification methods is studied by Phani [59]. According to this research, Adhikari's method seems suitable for model incompleteness and truncation. Lancaster's method suffers from more severe errors.

6.7 Conclusion

Damping matrix identification is a branch of research on its own. This chapter discusses specifically two types of damping matrix identification that are recommended for rotating systems. Lancaster's method is extended with left and right eigenvectors and yields theoretically the best results. By knowing left and right eigenvectors, all matrices are reconstructed. Although very promising, this is not easily implemented in practise, because the extraction of left and right eigenvectors is not straightforward and numerous measurements are needed. Adhikari's method is originally designed for non-rotating systems, but in this research it is proposed to observe the rotating system as non-rotating. This proposal is based upon the

equivalent decay rate model that is derived in chapter 5. An equivalent decay rate model for multiple degre of freedom systems is proposed. The rotating damping phenomenon then yields a regular speed dependent damping and the spatial distribution remains similar. On a simulation level, both methods work. However, the methods are very sensitive to errors on the eigenvectors. That is why, three optimization methods are proposed for the eigenvectors. Each of the methods have advantages and disadvantages and their use depends on preliminary knowledge or what is expected as outcome. The symmetry preserving method and the properness condition do not need any preliminary knowledge. The iterative procedure needs the mass matrix and a proposal for the damping matrix. The masking of the asymmetry is the lowest with the optimization by properness condition. The effectiveness of the optimization methods need experimental validation, which is discussed in the following chapter.

7

Experimental damping matrix identification

7.1 Introduction

Simulation, in chapter 6, shows that the damping matrix identification methods yield realistic damping matrices. Both for a rotor at standstill and during rotation, the methods work well. In simulation, there is preliminary knowledge of the damping and the model. Moreover, there is no noise present and there is neither truncation nor model incompleteness. Furthermore, in a measurement there are always unavoidable measurement errors. In this chapter, the test setups that are described in chapter 3 are used for damping matrix identification and for the discussion of the optimization methods. The torsional vibration setup is presented first. In this setup, the similarity between model and measurements is very high, especially for the mass and stiffness. The damping is controllable, and the noise is low. The measurements are first simulated. This ensures that the identification procedures are applied correctly. Second, the actual measurements are used to identify the damping matrices. Subsequently, the rotating damping setup is tested. The identification is performed at standstill, so there are no effects of rotation and finally the identification is performed while rotating.

7.2 The torsional vibration setup

The torsional vibration setup is used to validate the damping matrix estimation methods. The torsional vibration setup is especially designed such that a lumped parameter model yields accurate results and therefore it is easy to compare simulations with measurements. Moreover the behaviour of the damping in this setup is more easily predictable then in the rotating damping setup. First, the model is used to simulate forced responses. This strategy is used to gain more insight into the damping matrix identification methods.

7.2.1 Simulated results

A forced response is simulated using a method proposed by Ahlin [72]. The excitation signal used is a stepped sine. With the resulting time signal, the FRFs are calculated using the H_1 estimator [2]. Consequently, these FRFs are used to extract the modal parameters. The simulation generates noise-free data. Thus, the only errors on the results are bias errors arising from the frequency resolution and numerical errors made by the forced response algorithm. The effect of both errors on the eigenvectors and the resulting damping matrix is discussed. The simulated and the synthesized FRFs are shown in Figure 7.1. The identification procedure is able to generate almost the exact FRFs. However, the small error, that is hardly visible on the graphs, already has an impact on the identified eigenvectors, especially on the imaginary part, which is important for the damping identification. In Figure 7.2, the real and imaginary parts of the resulting eigenvectors are shown. The theoretical eigenvectors are plotted in gray, the identified eigenvectors in blue and the eigenvector optimized by the properness condition in orange. The eigenvectors are scaled such that the first coordinate is one. The real parts are practically the same and in the imaginary part, the biggest difference appears in the second mode. The properness condition is able to fix this difference.

In Table 7.1 the identified damping matrices are shown, calculated with the poles and eigenvectors extracted from the simulation. As identification methods, Adhikari's and Lancaster's methods are used and as optimization procedures the symmetry preserving method, the iterative procedure and the optimization by properness condition. The advantage of this simulation is that the identified matrices can be compared to the original damping matrix, as it was modeled. The location where the extra damping is added is marked in gray. As in this simulation, the damping matrix is defined symmetric, the identified damping matrix should also be symmetric. Both the symmetry preserving method and iterative force a symmetric damping matrix, but Adhikari's method yields an asymmetric matrix. In order to validate the symmetry, a symmetric norm is defined

$$N_s = \frac{\|C - C^T\|}{\|C\|} \tag{7.1}$$

with $\|\bullet\|$ the norm of a matrix. All the methods allow to identify the physical location where damping is added and the actual value. The methods that assume symmetry obviously lead to symmetric matrices, while with Adhikari's method, the matrix becomes asymmetric with a symmetric norm of 4.5×10^{-2}. This is noteworthy, because the damping was modelled to be symmetric. The only reason why Adhikari's method fails to yield a symmetric matrix is thus because of the slight errors on the eigenvectors. The asymmetry forced to yield a symmetric damping matrix with the symmetry preserving method. The iterative procedure succeeds in finding the best absolute value of the damping, but, the error second diagonal element is the largest. By using the properness condition, both Lancaster's method and Adhikari's method lead to a better result. The methods that yield a symmetric matrix also result in a damping matrix that is almost tridiagonal as is modelled.

A first conclusion of these simulations is that finding the extra added damping can be done with all methods. Although the iterative procedure yields a very good identification, it needs some preliminary knowledge which is a major drawback. Lancasters method with optimized eigenvectors by properness condition avoids this and even allows the extraction of mass and stiffness matrices. Adhikari's method with eigenvectors optimized by properness condition yields the best result.

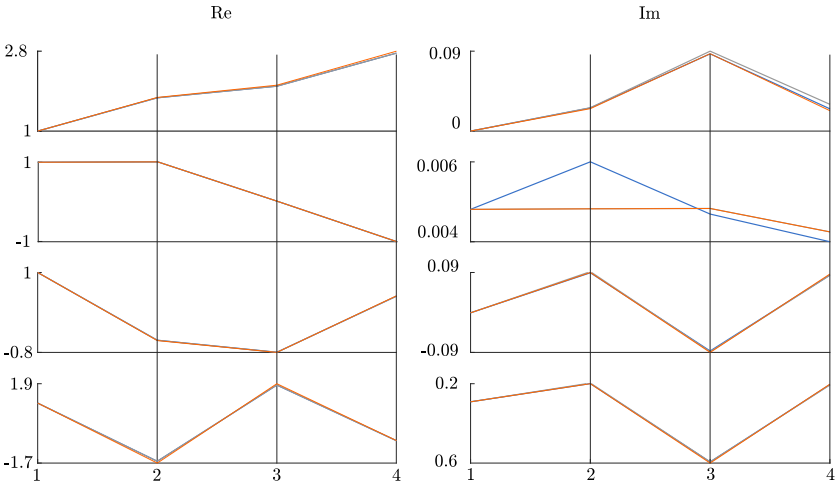

Figure 7.2: Real and imaginary part of the eigenvectors for the simulated torsional setup. Theoretical eigenvectors (gray), identified eigenvectors (blue), eigenvectors optimized by properness condition (orange)

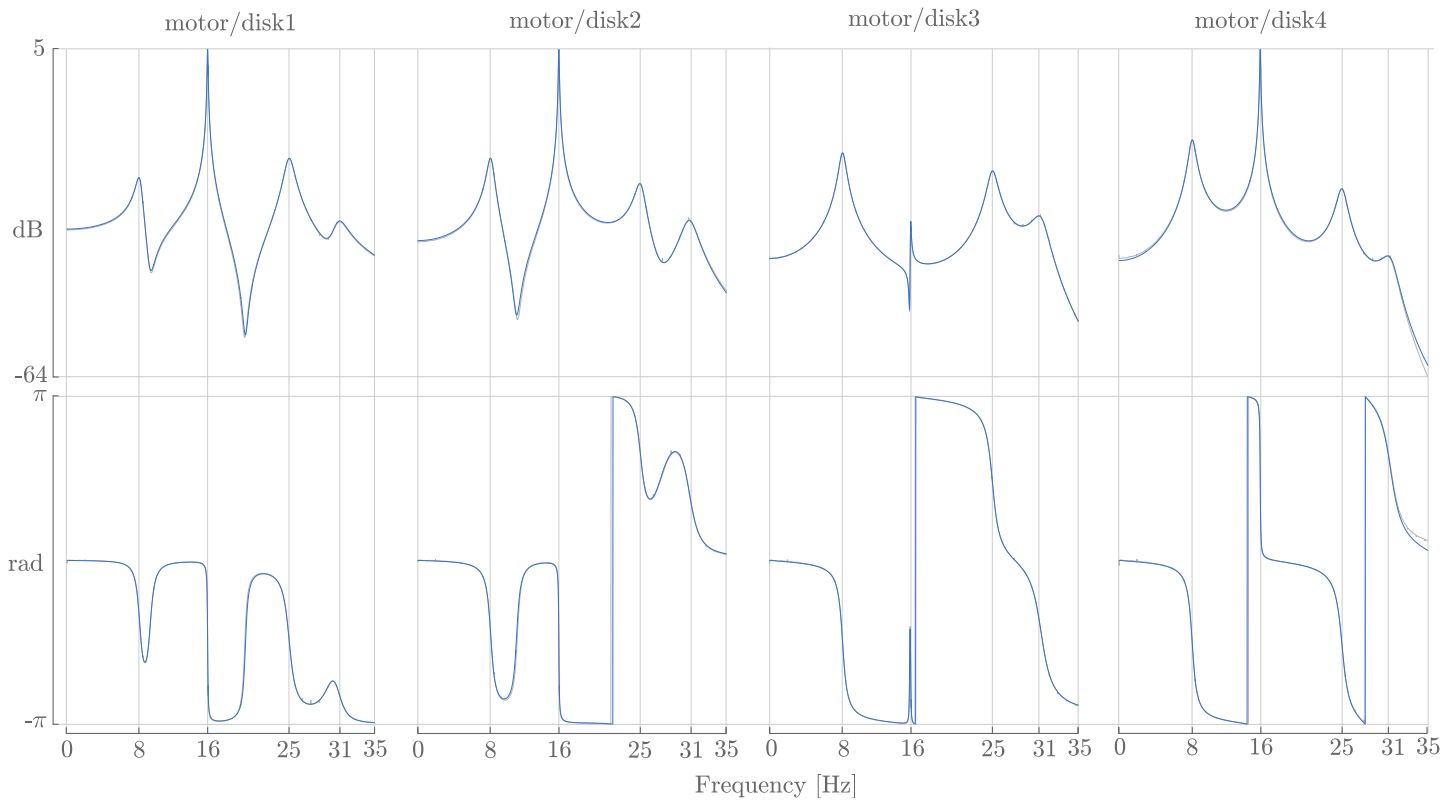

Figure 7.1: Simulated FRFs (gray) and synthesized FRFs (blue) for the torsional setup with extra added damping on the third disk

Damping matrix as modeled N_s=0
$10^{-3}\begin{bmatrix} 4.0 & -2.0 & 0 & 0 \\ -2.0 & 4.0 & -2.0 & 0 \\ 0 & -2.0 & \boxed{74.0} & -2.0 \\ 0 & 0 & -2.0 & 2 \end{bmatrix}$
Adhikari's general method $N_s = 4.5 \times 10^{-2}$
$10^{-3}\begin{bmatrix} 3.4 & -1.8 & -0.3 & -0.2 \\ -3.9 & 5.5 & -4.7 & -0.2 \\ 0.1 & -2.8 & \boxed{74.9} & -2.6 \\ 1.0 & -1.4 & -1.8 & 1.4 \end{bmatrix}$
Adhikari's symmetric method N_s=0
$10^{-3}\begin{bmatrix} 2.9 & -2.7 & -0.4 & 0.7 \\ -2.7 & 6.5 & -4.0 & -0.9 \\ -0.4 & -4.0 & \boxed{74.7} & -2.0 \\ 0.7 & -0.9 & -2.0 & -1.2 \end{bmatrix}$
Iterative procedure N_s=0
$10^{-3}\begin{bmatrix} 1.4 & -2.6 & -0.9 & 1.7 \\ -2.6 & 8.2 & -3.9 & -1.9 \\ -0.9 & -3.9 & \boxed{74.1} & -1.5 \\ 1.7 & -1.9 & -1.5 & 0.5 \end{bmatrix}$
Lancaster with properness N_s=0
$10^{-3}\begin{bmatrix} 3.0 & -2.7 & -5.0 & 0.6 \\ -2.7 & 6.0 & -3.9 & -0.9 \\ -0.5 & -3.9 & \boxed{75.8} & -2.3 \\ 0.6 & -0.9 & -2.3 & 1.2 \end{bmatrix}$
Adhikari with optimization N_s=1.0910 $\times 10^{-4}$
$10^{-3}\begin{bmatrix} 3.1 & -2.8 & -0.3 & 0.6 \\ -2.8 & 6.1 & -3.9 & -0.8 \\ -0.3 & -3.9 & \boxed{74.7} & -2.1 \\ 0.6 & -0.8 & -2.1 & 1.3 \end{bmatrix}$

Table 7.1: Comparison of the identified damping matrices for the torsional setup with the different methods extracted from the simulation with N_s the symmetric norm

7.2.2 Experimental results

The torsional vibration setup is excited by forcing a stepped sine angular displacement to the motor. The responses of each disk are measured by the encoder and the FRFs are calculated with the H_1 estimator. In the measurement, there is no preliminary knowledge of the damping, only, that there is extra added damping to the third disk. It is important to notice that the extra added damping is definitely not viscous of nature and all damping estimation procedures here assume viscous damping. The experimental and the synthesized FRFs after identification are shown in Figure 7.4. The noise on the measurement is reduced because of averaging. The trends of the measurement and simulation correspond quite well. The eigenvectors are depicted in Figure 7.3. In gray the identified eigenvector is shown and the blue line is the result from optimization with properness condition. It is seen that the optimization by properness condition especially affects the imaginary part.
In Table 7.2 the identified damping matrices are shown. The same trends return as in the simulation. All methods are able to identify the location with extra added damping, marked in gray. The triadiagonal form of the damping matrix, as modelled, is not seen in the identified matrices. Adhikari's general method leads to an asymmetric matrix. The reason for this is twofold. First, there are errors on the eigenvectors and second the damping is the setup is not viscous of nature. The optimization methods yield better results, however, they tend to mask this asymmetry. The iterative method leads to the lowest actual value of the damping. Both Lancasters and Adhikari's method optimized by the properness condition result in similar matrices.

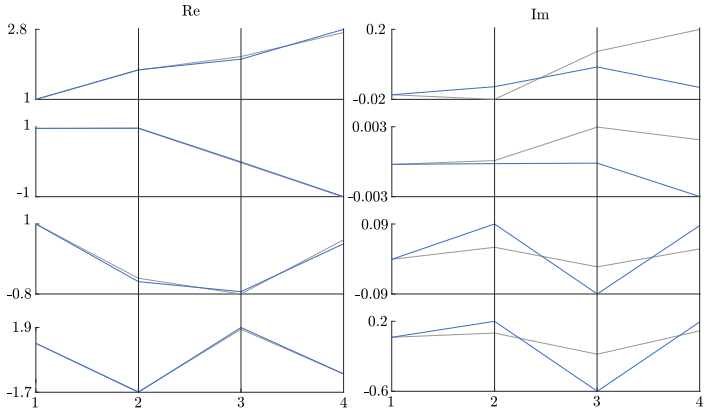

Figure 7.3: Real and imaginary part of the eigenvectors for the torsional setup. Identified eigenvectors (gray), eigenvectors optimized by properness condition (blue)

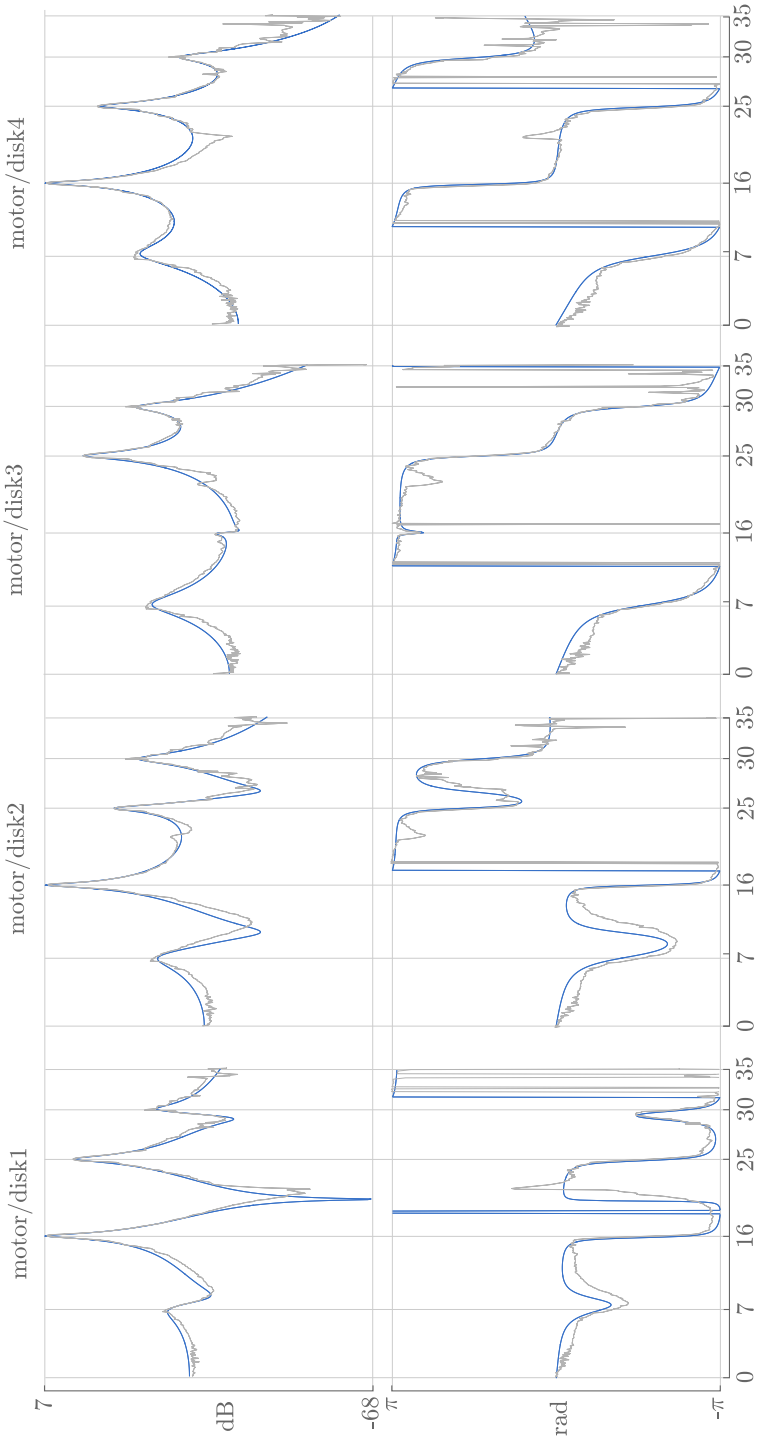

Figure 7.4: Measured FRFs (gray) and synthesized FRFs (blue) for the torsional setup with extra added damping on the third disk.

Adhikari's general method $N_s = 4.3 \times 10^{-1}$
$10^{-3} \begin{bmatrix} 11.2 & 7.0 & 12.0 & 10.4 \\ -3.2 & 2.0 & -3.4 & -7.4 \\ 11.2 & 14.5 & \boxed{54.9} & 24.3 \\ 7.2 & 19.1 & 23.4 & 34.5 \end{bmatrix}$
Adhikari's symmetric method N_s=0
$10^{-3} \begin{bmatrix} 9.1 & 2.5 & 8.3 & 5.0 \\ 2.4 & 11.3 & 10.0 & 12.2 \\ 8.3 & 10.0 & \boxed{50.8} & 19.6 \\ 5.0 & 12.2 & 19.6 & 31.7 \end{bmatrix}$
Iterative procedure N_s=0
$10^{-3} \begin{bmatrix} 7.5 & 7.9 & 3.7 & 4.6 \\ 7.9 & 11.7 & 11.6 & 11.2 \\ 3.7 & 11.6 & \boxed{41.8} & 5.6 \\ 4.6 & 11.2 & 5.6 & 18.1 \end{bmatrix}$
Lancaster with properness N_s=0
$10^{-3} \begin{bmatrix} 9.9 & 2.2 & 9.5 & 6.8 \\ 2.2 & 7.1 & 7.6 & 9.9 \\ 9.5 & 7.6 & \boxed{51.3} & 21.1 \\ 6.8 & 9.9 & 21.1 & 34.3 \end{bmatrix}$
Adhikari with properness N_s=1.3461 $\times 10^{-4}$
$10^{-3} \begin{bmatrix} 9.9 & 2.2 & 9.4 & 6.8 \\ 2.2 & 7.1 & 7.6 & 9.9 \\ 9.5 & 7.6 & \boxed{51.3} & 21.1 \\ 6.8 & 9.9 & 21.1 & 34.3 \end{bmatrix}$

Table 7.2: Comparison of the identified damping matrices for the torsional setup with the different methods from measurements with N_s the symmetric norm

7.2.3 Discussion

The torsional vibration setup allows to gain some particular insights into the damping matrix identification procedures and the optimizations. In simulation, all the methods work effectively. The damping matrices are approximately the same as in the model, and the extra added damping on the third disk is easily found. However, even in simulation, Adhikari's method already leads to some asymmetry. This is important, because the model has symmetric matrices, and there is no noise on the simulations. The small errors that are present are numerical errors due to the simulation. After optimization, the results are better. For the actual measurement, noise is present, and there is no preliminary information on the damping. It is seen that the resulting eigenvectors have a high correspondence to the modelled ones. Both the optimization by iterative procedure and properness condition are able to attenuate the eigenvectors towards a better result. Although the identified damping matrices are not able to reconstruct the tridiagonal form, as in the model, they are all able to find the extra added damping. The properness condition is preferred here as an optimization method, because there is no preliminary knowledge needed.

7.3 The rotating damping setup

In the rotating damping setup, the shaft is excited with the hammer at point 1 in Figure 3.13 and the response is measured at the other five points. The frequency response functions are estimated with a H_1 estimator and 5 averages are used. The measurements are performed both at 0 rpm and at 1000 rpm. The finite element model, described in chapter 2, is used to simulate the theoretical eigenvectors.

7.3.1 Results at standstill

The resulting frequency response functions at standstill are shown in Figure 7.5. It is seen that the FRFs are noisy. This is mainly due to the eddy current probes that generate a high noise level. Especially the phase is noisy, but it is possible to find the correct trends. The resulting eigenvectors have additional errors because of this noise. The eigenvectors are shown in Figure 7.6 where the identified eigenvectors are shown in gray, and the eigenvectors optimized by properness condition in blue, scaled towards unity of the first coordinate. Similar to the torsional test bench, the optimization procedure especially affects the imaginary part.
The resulting identified damping matrices that are shown in Table 7.3. None of the damping matrices have entire positive elements on the diagonal. Adhikari's general method leads to an asymmetric matrix with a high symmetric norm of 1.1. A comparison between the different damping matrices is difficult, because there are many uncertainties. It is however possible to calculate the poles of the system

Adhikari's general method N_s=1.1	
10^2	$\begin{bmatrix} -0.1 & -0.4 & -0.5 & -0.5 & -0.2 \\ 0.4 & 0.5 & 1.0 & 0.7 & 0.5 \\ -0.5 & -0.8 & -1.4 & -1.2 & -0.8 \\ 0.5 & 0.6 & 1.5 & 1.0 & 0.8 \\ -0.3 & -0.6 & -0.8 & -0.8 & -0.4 \end{bmatrix}$
Adhikari's symmetric method N_s=0	
10^2	$\begin{bmatrix} 0.2 & -0.06 & 0.1 & -0.01 & 0.1 \\ -0.06 & -0.08 & -0.05 & -0.01 & -0.1 \\ 0.1 & -0.05 & 0.3 & 0.02 & 0.2 \\ -0.01 & -0.1 & 0.02 & -0.02 & -0.1 \\ 0.1 & -0.1 & 0.2 & -0.1 & 0.1 \end{bmatrix}$
Iterative procedure N_s=0	
10^2	$\begin{bmatrix} 1.5 & -0.8 & 0.7 & -0.4 & 0.6 \\ -0.8 & -0.3 & -0.3 & -0.9 & -0.8 \\ 0.7 & -0.3 & 1.3 & -0.1 & 1.3 \\ -0.4 & -0.9 & -0.1 & -1.2 & -0.7 \\ 0.6 & -0.8 & 1.3 & -0.7 & 0.6 \end{bmatrix}$
Lancaster with properness N_s=0	
10^2	$\begin{bmatrix} 0.3 & -0.08 & 0.4 & 0.08 & 0.3 \\ -0.08 & -0.2 & -0.2 & -0.3 & -0.3 \\ 0.4 & -0.2 & 0.7 & 0.02 & 0.4 \\ 0.08 & -0.3 & 0.02 & -0.3 & -0.2 \\ 0.3 & -0.3 & 0.4 & -0.2 & 0.2 \end{bmatrix}$
Adhikari with properness N_s=$\times 10^{-3}$	
10^2	$\begin{bmatrix} 0.3 & -0.08 & 0.4 & 0.08 & 0.3 \\ -0.08 & -0.02 & -0.2 & -0.3 & -0.3 \\ 0.4 & -0.2 & 0.7 & 0.01 & 0.4 \\ 0.08 & -0.3 & 0.02 & -0.3 & -0.2 \\ 0.3 & -0.3 & 0.4 & -0.2 & 0.2 \end{bmatrix}$

Table 7.3: Comparison of the identified damping matrices for the rotating damping setup at standstill with the different methods from measurements

with these new matrices and compare them with the actual measured poles. The result is seen in Table 7.4. Lancaster's method and Ahdikari's method, optimized with properness condition result in poles with a small error.

7.3.2 Results at 1000 rpm

The resulting frequency response functions at 1000 rpm are shown in Figure 7.7. The noise is very high. This is due to the rotation and the eddy current probes. Still, it is possible to fit the synthesized frequency response functions. The re-

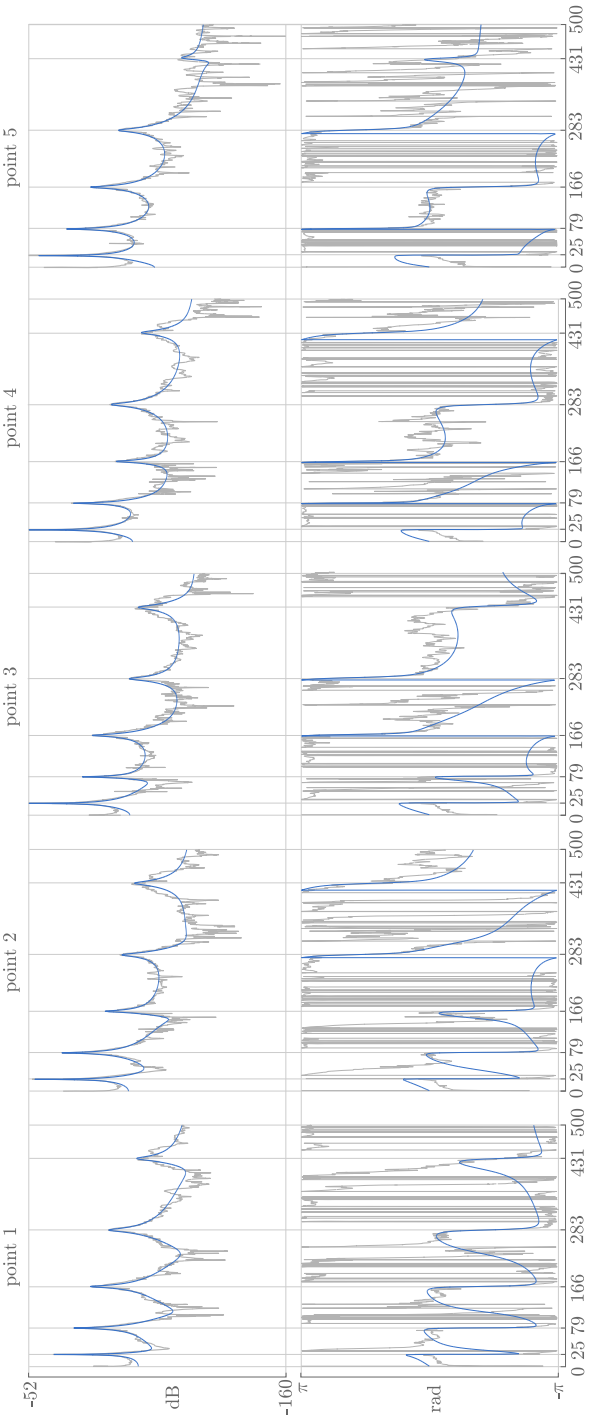

Figure 7.5: Measured FRFs (gray) and synthesized FRFs (blue) for the rotating damping setup at standstill

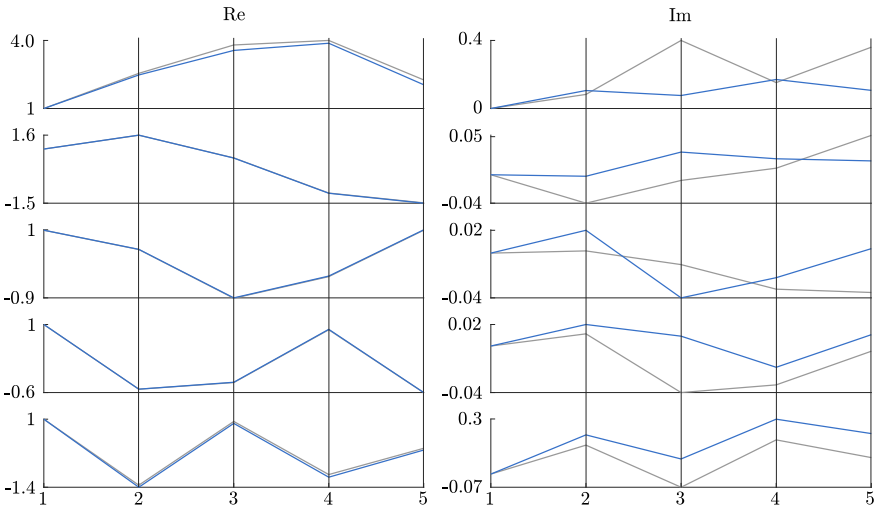

Figure 7.6: Real and imaginary part of the eigenvectors for the rotating damping setup at standstill. Identified eigenvectors (gray), eigenvectors optimized by properness condition (blue)

Measured poles	Lancaster with properness	Adhikari with properness
-0.8+154.4i	-0.8+154.4i	-0.8+156.8i
-3.5+499.4i	-3.5+499.4i	-3.5+499.6i
-8.0+1039.9i	-8.0+1039.9i	-7.9+1040.3i
-15.0+1776.3i	-15.2+1776.3i	-15.0+1776.1i
-18.7+2708.0i	-19.3+2707.2i	-18.9+2664.4i

Table 7.4: Comparison of the measured poles and the calculated poles with Lancaster's and Adhikari's method after identification of the damping matrix

sulting eigenvectors are shown in Figure 7.8. Again here, the optimization by properness condition especially affects the imaginary part with this type of scaling. Only the real part of the first mode is more affected by the optimization. The resulting identified damping matrices are shown in Table 7.5. It can be seen that Adhikari's method yields very large damping matrices. This means that, although expected from simulation, Adhikari's method is not sufficient for this setup. Even after optimization of the eigenvectors, the matrices are even worse. For Lancasters procedure, however, with optimization, the effect is similar as in the measurements at standstill. Table 7.6 shows a comparison of the actual measured poles with the calculated poles from both Lancaster and Adhikari with properness condition. As expected, the damping matrices by Adhikari's method have no relevance as the elements are too large. However, Lancaster's method here yields a very good estimate of the poles.

7.3.3 Discussion

Measurements on the rotating damping setup are more difficult then the measurements on the torsional test bench. The noise is higher, the damping is unknown, there is modal incompleteness and truncation and there are rotating effects to take into account. At standstill, there is no effect of the rotation. The damping matrices identified by both Lancaster's and Adhikari's method yield the best results. Both methods yield a good approximation of the system poles. At 1000 rpm, however, Adhikari's method proofs to be insufficient. Lancaster's method with optimization, on the other hand, results in a relevant damping matrix. This is shown again by the calculated system poles.

7.4 Conclusion

The identification procedures and the optimizations that are discussed in chapter six have been applied in this chapter on the torsional vibration setup and the rotating damping setup. The torsional vibration setup, which is especially designed to have a high correspondence between the measurements and a lumped parameter model, yields the best results. The extra damping that is added to the third disk is found on the same physical location in the damping matrix. In the rotating damping setup, there are more uncertainties. There is high noise due to the eddy current probes and the rotation, and there is modal incompleteness and truncation. At standstill, however, it is still possible to find relevant damping matrices with both Lancaster's and Adhikari's method after optimizing the eigenvectors with properness condition. The relevance is demonstrated through a comparison between the measured poles and the calculated poles with the new damping matrices. At an operation speed of 1000 rpm Adhikari's method is not working anymore. Lancaster's

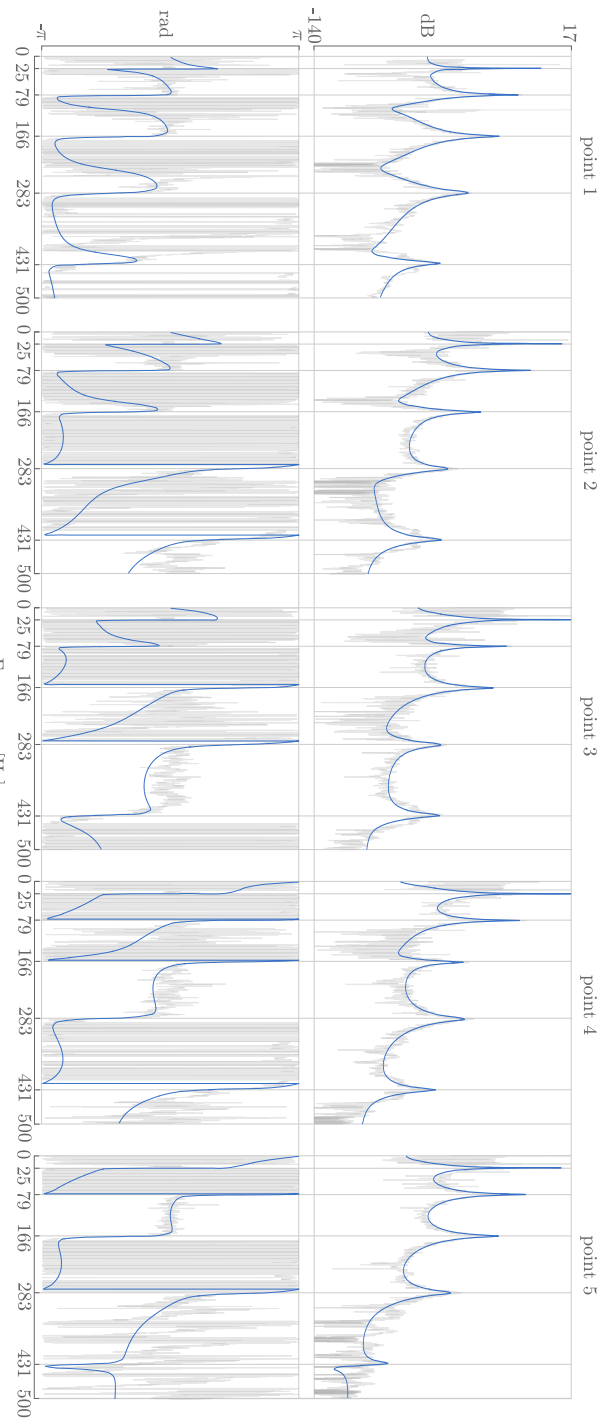

Figure 7.7: Measured FRFs (gray) and synthesized FRFs (blue) for the rotating damping setup at 1000 rpm

Adhikari's general method N_s=1.8	
10^5	$\begin{bmatrix} 0.8 & -16.2 & 6.3 & 1.4 & -0.6 \\ 1.4 & 0.05 & -0.1 & -0.9 & -1.0 \\ -0.4 & -0.1 & 0.09 & 0.4 & 0.3 \\ -1.2 & 0.7 & -0.2 & 0.1 & 1.1 \\ 0.5 & 1.1 & -0.5 & -1.3 & 0.06 \end{bmatrix}$
Adhikari's symmetric method N_s=0	
10^4	$\begin{bmatrix} 2.7 & -3.0 & 1.1 & 1.1 & -3.0 \\ -3.0 & -0.7 & 0.2 & 2.2 & 1.9 \\ 1.1 & 2.1 & -0.07 & -0.8 & -0.7 \\ 1.1 & 2.2 & -0.8 & -2.4 & -0.02 \\ -3.0 & 1.9 & -0.7 & -0.02 & 2.8 \end{bmatrix}$
Iterative procedure N_s=0	
10^2	$\begin{bmatrix} 1.1 & 0.2 & -0.2 & 1.4 & -1.0 \\ 0.2 & -1.1 & 0.5 & 0.9 & 0.2 \\ -0.2 & 0.5 & -0.8 & -0.4 & -1.0 \\ 1.4 & 0.9 & -0.4 & 3.0 & -0.7 \\ -1.0 & 0.2 & -1.0 & -0.7 & -0.1 \end{bmatrix}$
Lancaster with properness N_s=0	
10	$\begin{bmatrix} 0.5 & -0.3 & 1.8 & 0.8 & -1.8 \\ -0.3 & -4.4 & -0.2 & -2.2 & -3.0 \\ 1.8 & -0.2 & 6.5 & -0.2 & -2.2 \\ 0.8 & -2.1 & -0.2 & -0.5 & -1.2 \\ -1.8 & -3.0 & -2.2 & -1.2 & -2.6 \end{bmatrix}$
Adhikari with properness N_s=6.7×10^{-2}	
10^9	$\begin{bmatrix} -15.2 & 3.2 & -1.0 & 5.7 & 12.0 \\ 4.2 & 9.3 & -3.1 & -9.9 & 0.4 \\ -1.4 & -3.1 & 1.0 & 3.3 & -0.1 \\ 4.9 & -9.3 & 3.07 & 4.9 & -6.8 \\ 12.3 & 1.1 & -0.4 & -7.6 & -8.3 \end{bmatrix}$

Table 7.5: Comparison of the identified damping matrices for the rotating damping setup at 1000 rpm with the different methods from measurements

Measured poles	Lancaster with properness	Adhikari with properness
-0.4+153.8i	-0.4+153.7i	1245949.7
-3.3+499.9i	-3.24+499.8i	-794.0
-8.3+1040.7i	-7.6+1041.8i	0.8
-18.2+1777.5i	-18.0+1782.2i	99.9+1050.5i
-14.7+2696.7i	-20.8+2708.0i	320.1+2581.0i

Table 7.6: Comparison of the measured poles and the calculated poles with Lancaster's and Adhikari's method after identification of the damping matrix

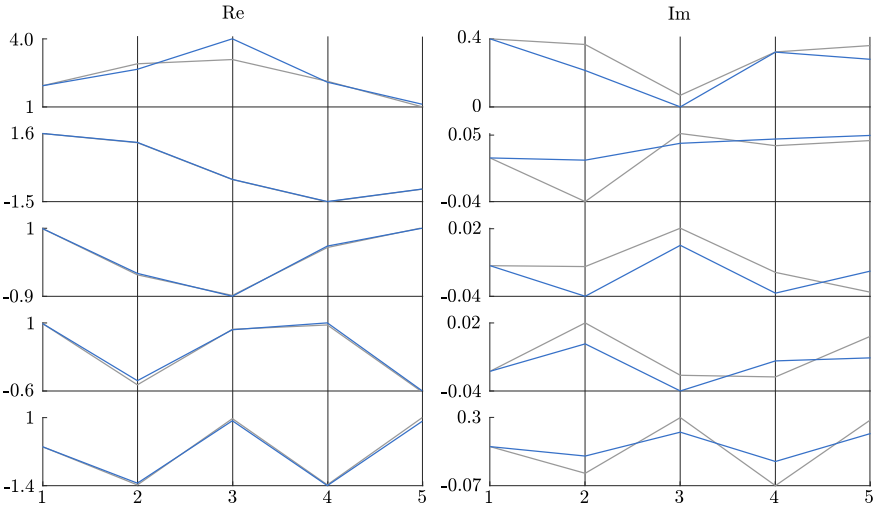

Figure 7.8: Real and imaginary part of the eigenvectors for the rotating damping setup at 1000 rpm. Identified eigenvectors (gray), eigenvectors optimized by properness condition (blue)

method optimized by properness condition, however, succeeds in estimating the correct poles.

8

Conclusions and future work

When the stability of rotating machinery is concerned, rotating damping is definitely a phenomenon which has to be accounted for. High speed machines with vast amounts of rotating energy that become unstable can have disastrous results. But also small machines that become unstable have to be avoided. It can cause premature failure, reduced accuracy and decreased energy efficiency. Rotating damping is already known as a destabilizing effect for over more than a century. Through history, several observations are already made. However, this type of damping is still difficult to model and especially to validate experimentally. Damping involves all physical elements that dissipate energy or all mechanisms that transform vibration energy into any other form of energy. While mass and stiffness are more easy to observe and model, damping is still not fully understood. Moreover, in rotating systems, damping is even dependent on the operating speed and it causes a nonsymmetric effect. All these elements cause difficulties in experimental procedures. Furthermore, the damping in rotating systems is generally low, which makes it particularly difficult to perform accurate measurements. The asymmetry of the effect causes a difficulty to use classical procedures that are generally based upon the assumption of symmetry. On the other hand, more advanced methods result in complex and time consuming procedures that are not easily implemented. In this thesis, important contributions are made towards experimental procedures that are less time consuming and easy to implement. These procedures are promising. In this conclusion, the highlights of the thesis are repeated and possible future work is proposed.

8.1 Important contributions

Towards finite element modelling, this research provides a global overview of rotating damping, the physical behaviour and the modelling. Existing literature is combined into a concise interpretation with a special focus on the experimental validation. Rotating damping is presented as the result of a follower force, which in its turn is the result of a difference between the rotor spin and whirl. The damping in the finite element model is derived from the Rayleigh dissipation function. By doing so the model is kept straightforward and easy for experimental validation. Whereas generally, the physical behaviour of rotors is described through the Jeffcott rotor, a novel insight is created with the *modal model*. The modal model, as is described, has complex parameters. By using perturbation analysis on a lightly damped system, it is shown that these parameters can be purely real or purely imaginary. Under specific conditions, there is a relation between the left and right eigenvectors. This leads to a generalization of the Jeffcott rotor where both gyroscopic effect and rotating damping are included. The expression is particularly useful for an *experimental estimation procedure*.

When rotating damping is concerned, there is a lack of experimental identification procedures. The *rotating damping setup*, that is designed and dimensioned within this thesis is an important contribution towards experimental validation. The simple design allows a thorough understanding of the rotating damping and its effect on the stability threshold speed. The *automated impact hammer* allows a repeatable and controllable excitation force which highly improves the repeatability of the measurements. The setup is *modular* in a way that disks can be added or removed.
The first experimental procedure validates the assumption of light damping by using a basic interpretation of the undamped and damped eigenvectors. The second experimental procedure is designed for *the prediction of the stability threshold speed caused by rotating damping*. It is shown that, by combining the modal model with insights on the energy dissipation in the rotor, the procedure is able to predict the stability threshold speed by exciting and measuring at only one location for different operating speeds. It is proved experimentally that the rotor becomes unstable above the stability threshold speed.
The second experimental procedure focusses on the *damping matrix identification*. Two modal methods are described together with *three optimization procedures*. The existing damping matrix identification methods are extended towards rotating systems. This is first done by using the left and the right eigenvectors and second by proposing an equivalent decay rate model for multiple degree of freedom systems. This method observes the rotating systems as nonrotating. By doing this, a damping matrix estimation procedure designed for nonrotating systems can be

used on rotating systems. The validation of the methods is first performed on a four degree of freedom torsional test bench. For this simple application, the methods prove their effectiveness. On the more challenging rotating damping setup, the methods are also effective. It is possible to find a correct reconstruction of the poles, which is important in stability analysis.

Towards industrial applications special attention has been given to the effectiveness of the proposed procedures by reducing the number of measurements and increasing the physical insight. As already stated, the stability threshold speed can be predicted by using only one measurement location. This not only reduces the time, but also the number of sensors and actuators that are needed.

8.2 Future research

This research provides basic insights that open the way for many new applications. The procedure to estimate the stability threshold speed by using only one location of the rotating shaft can be extended towards actual industrial applications. Therefore, *the robustness of the method* has to be optimized. This can be done by adding extra rotating damping to the shaft by attenuating the energy dissipation in the rotating frame. Possible options are shrink fitting parts, other shaft materials or magnetic fields that cause eddy currents in the rotor. A difference in the rotating damping will affect the stability threshold speed, which has to be predicted by the method.

Towards industrial applications, the use of *operational modal analysis* has to be investigated. Whenever it is possible to exclude the external excitation, it is not only cost effective, but also space-saving. Because the estimation of the stability threshold speed is only based upon the poles, the step toward operational modal analysis should be small. As for the damping matrix estimation techniques, there will be a scaling problem which has to be dealt with.

As the damping matrix identification procedures suffers from errors on the eigenvectors it is an option to discard the modal methods in future. The main reason of the focus on the modal methods was to keep the number of measurements low. There are however, novel methods that are very promising and also provide possibilities to reduce the number of measurements [73] [74]. Although also not designed for rotating systems, these methods can be used in the proposed procedure to estimate the damping matrix.

Although the damping, based upon the Rayleigh dissipation function, in the model yields the best results, it would be interesting to take other damping types

into account and study the influence on the measurement procedures. Genta's equivalent hysteretic damping formulation for instance [75], or the Ahdikari's non-viscous damping [62].

Finally, the research on sensors and actuators is still ongoing. *MEMS, or Microelectromechanical Systems* are gaining accuracy and applicability. There small size, low cost and easy implementation paves the way for multisensor applications with a numerous amount of sensors. Combined with batteries and wireless technology this type of sensors can be placed anywhere. In future, reduction of the number of sensors looses its relevance, and already today the main question is how to handle the *big data* that results from all these sensors.

References

[1] Maurice L. Adams. *Rotating machinery vibration: from analysis to troubleshooting*. CRC Press/Taylor & Francis, 2009.

[2] Anders Brandt. *Noise and Vibration Analysis: Signal Analysis and Experimental Procedures*. Wiley, 2011.

[3] DF Pilkey and DJ Inman. *An iterative approach to viscous damping matrix identification*. In IMAC XV proceedings, pages 1152–1157, 1997.

[4] K Gupta. *Symposium on Emerging Trends in Rotor Dynamics*. Springer, New Delhi, India, 2009.

[5] William E. Forsthoffer. *Forsthoffer's Best Practice Handbook for Rotating Machinery*. Elsevier, 2011.

[6] B. Vervisch, K. Stockman, and M. Loccufier. *Sensititity of the stability threshold in linearized rotordynamic*. In International Conference on Noise and Vibration Engineering 2012, ISMA 2012, including USD 2012: International Conference on Uncertainty in Structure Dynamics, volume 2, pages 1387–1401, 2012.

[7] L. Meirovitch. *Computational Methods in Structural Dynamics*. 1980.

[8] D Inman. *Damping models*. In Encyclopedia of Vibration, pages 335–342. Elsevier, 2001.

[9] W Rankine. *On the centrifugal force of rotating shafts*. Engineer (London), 27(249), 1869.

[10] B.L. Newkirk. *Shaft whipping*. General Electric Review, 27:169–178, 1924.

[11] A.L. Kimball. *Internal friction theory of shaft whirling*. General Electric Review, 27:224–251, 1924.

[12] D. M. Smith. *The Motion of a Rotor Carried by a Flexible Shaft in Flexible Bearings*. Proceedings of the Royal Society A: Mathematical, Physical and Engineering Sciences, 142(846):92–118, oct 1933.

[13] D. Robertson. *The whirling of shafts*. Engineer, (158):216–228, 1934.

[14] B L Newkirk and H D Taylor. *Shaft whipping due to oil action in journal bearings*. General Electric Review, 28(8):559–568, 1925.

[15] Agnieszka Muszynska. *Rotordynamics*. 2005.

[16] F. F. Ehrich. *Shaft Whirl Induced by Rotor Internal Damping*. Journal of Applied Mechanics, 31:279, 1964.

[17] E. J. Gunter and P. R. Trumpler. *The Influence of Internal Friction on the Stability of High Speed Rotors With Anisotropic Supports*. Journal of Engineering for Industry, 91(4):1105, nov 1969.

[18] E. S. Zorzi and H. D. Nelson. *Finite Element Simulation of Rotor-Bearing Systems with Internal Damping*. Journal of Engineering for Power, 99(1):71–76, jan 1977.

[19] D. W. Childs. *The Space Shuttle Main Engine High-Pressure Fuel Turbopump Rotordynamic Instability Problem*. Journal of Engineering for Power, 100(1):48, jan 1978.

[20] J.W. Lund. *Destabilzation of rotors from friction in internal joints with micro slip*. In Proc. The International Conf. On Rotordynamics, pages 487–491, Tokyo, 1986.

[21] J. Walton, A. Artiles, J. Lund, J. Dill, and E. Zorzi. *Internal rotor friction instability*. feb 1990.

[22] L Forrai. *Instability due to internal damping of symmetrical rotor-bearing systems*. Journal of Computational and Applied Mechanics, 1(2):137–147, 2000.

[23] L Forrai. *A finite element model for stability analysis of symmetrical rotor systems with internal damping*. Journal of Computational and Applied Mechanics, 1(1):37–47, 2000.

[24] Mohamed A Kandil. *On Rotor Internal Damping Instability*. PhD thesis, Imperial College London, 2004.

[25] Syed Muhammad Mohsin Jafri. *Shrink fit effects on rotordynamic stability: Experimental and theoretical study*. PhD thesis, Texas A&M University, 2007.

[26] Eric Chatelet, Olivier Montagnier, and Georges Jacquet-richardet. *Dynamic Instability Analysis of Internally Damped Rotors*. In Proceedings of GT2007, number 1, pages 1–10, 2007.

[27] O Montagnier and C Hochard. *Dynamic instability of supercritical driveshafts mounted on dissipative supportsEffects of viscous and hysteretic internal damping*. Journal of Sound and Vibration, 305(3):378–400, aug 2007.

[28] M Chouksey, SV Modak, and JK Dutt. *Influence of rotor-shaft material damping on modal and directional frequency response characteristics*. In Proceedings of ISMA 2010, pages 1543–1558, 2010.

[29] M. Chouksey, J.K. Dutt, and S.V. Modak. *Modal analysis of rotor-shaft system under the influence of rotor-shaft material damping and fluid film forces*. Mechanism and Machine Theory, 48:81–93, feb 2012.

[30] Giancarlo Genta. *Dynamics of rotating systems, Volume 1*. Springer, 2005.

[31] Donald E. Bently and Charles T. Hatch. *Fundamentals of rotating machinery diagnostics*. 2002.

[32] Tomasz Krysinski and François Malburet. *Mechanical Instability*. 2013.

[33] G. Ramanujam and C.W. Bert. *Whirling and stability of flywheel systems, part I: Derivation of combined and lumped parameter models*. Journal of Sound and Vibration, 88(3):369–398, jun 1983.

[34] D. J. Ewins. *Modal Testing: Theory, Practice and Application (Mechanical Engineering Research Studies: Engineering Dynamics Series)*. Wiley, 2001.

[35] Singiresu S Rao. *Mechanical Vibrations*. Pearson, 2004.

[36] Zhi-Fang Fu and Jimin He. *Modal Analysis*. 2001.

[37] Françoise Tisseur and Karl Meerbergen. *The quadratic eigenvalue problem*. Society for Industrial and Applied Mathematics, 43(2):235–286, 2006.

[38] I. Bucher and D. J. Ewins. *Modal analysis and testing of rotating structures*. Philosophical Transactions of the Royal Society A: Mathematical, Physical and Engineering Sciences, 359(1778):61–96, jan 2001.

[39] Igor Alekseevich Karnovski and Olga I. Lebed. *Free Vibrations of Beams and Frames: Eigenvalues and Eigenfunctions*. 2004.

[40] Allan Piersol and Thomas Paez. *Harris' Shock and Vibration Handbook*. 2009.

[41] Tejas H. Patel and Ashish K. Darpe. *Experimental investigations on vibration response of misaligned rotors*. Mechanical Systems and Signal Processing, 23(7):2236–2252, oct 2009.

[42] Mohsen Nakhaeinejad and Suri Ganeriwala. *Observations on dynamic responses of misalignments*. Technical report, 2009.

[43] MA Peres, RW Bono, and DL Brown. *Practical Aspects of Shaker Measurements for Modal Testing*. processvibration.com, pages 2539–2550.

[44] P Castellini. *Measurement of vibrational modal parameters using laser pulse excitation techniques*. Measurement, 35(2):163–179, mar 2004.

[45] R. Farshidi, D. Trieu, S.S. Park, and T. Freiheit. *Non-contact experimental modal analysis using air excitation and a microphone array*. Measurement, 43(6):755–765, jul 2010.

[46] S. Vanlanduit, F. Daerden, and P. Guillaume. *Experimental modal testing using pressurized air excitation*. Journal of Sound and Vibration, 299(1-2):83–98, jan 2007.

[47] Bram Vervisch, Michael Monte, Kurt Stockman, and Mia Loccufier. *Acoustical excitation for damping estimation in rotating machinery*. In Conference Proceedings of the Society for Experimental Mechanics Series, volume 6, pages 473–480, 2013.

[48] Eric H. Schweitzer, Gerhard, Maslen. *Magnetic Bearings: Theory, Design, and Application to Rotating Machinery*. Springer Science & Business Media, 2009.

[49] Frits Petit. *Exploring the limitations of linear and nonlinear vibration absorbers*. PhD thesis, Ghent University, 2012.

[50] John M. Vance, Fouad Y. Zeidan, and Brian Murphy. *Machinery Vibration and Rotordynamics*. John Wiley & Sons, 2010.

[51] Henry Homan Jeffcott. *The lateral vibration of loaded shafts in the neighbourhood of a whirling speedthe effect of want of balance*. Philosophical Magazine, 37(6):304, 1919.

[52] L. Meirovitch and G. Ryland. *A perturbation technique for gyroscopic systems with small internal and external damping*. Journal of Sound and Vibration, 100(3):393–408, 1985.

[53] W. Wang and J. Kirkhope. *New eigensolutions and modal analysis for gyroscopic/rotor systems, Part I: Undamped systems*. Journal of Sound and Vibration, 2(175):159–170, 1994.

[54] W. Wang and J. Kirkhope. *New eigensolutions andmodal analysis for gyroscopic/rotor systems, Part 2: Perturbation analysis for damped system*. Journal of Sound and Vibration, 175(2):171–183, 1994.

[55] J.T. Sawicki and G. Genta. *Modal Uncoupling of Damped Gyroscopic Systems*. Journal of Sound and Vibration, 244(3):431–451, 2001.

[56] ML Adams and J. Padovan. *Insights into linearized rotor dynamics*. Journal of Sound and Vibration, 76(1):129–142, 1981.

[57] J Woodhouse. *Linear damping models for structural vibration*. Journal of Sound and Vibration, 215:547–569, 1998.

[58] D. E. Beskos and B. A. Boley. *Critical Damping in Linear Discrete Dynamic Systems*. Journal of Applied Mechanics, 47(3):627, sep 1980.

[59] A. Srikantha Phani and J. Woodhouse. *Viscous damping identification in linear vibration*. Journal of Sound and Vibration, 303(3-5):475–500, jun 2007.

[60] P Lancaster. *Expressions for damping matrices in linear vibration problems*. Journal of the Aerospace Sciences, 28(3):256–256, 1961.

[61] S. Adhikari and J. Woodhouse. *Identification of Damping: Part 1, Viscous Damping*. Journal of Sound and Vibration, 243(1):43–61, may 2001.

[62] S. Adhikari and J. Woodhouse. *Identification of Damping: Part 2, Non-Viscous Damping*. Journal of Sound and Vibration, 243(1):63–88, may 2001.

[63] E Balmes. *New results on the identification of normal modes from experimental complex modes*. Mechanical Systems and Signal Processing, 1997.

[64] H Ahmadian and G M L Gladwell. *Extracting Real Modes from Complex Measured Modes*. (1983):507–510, 1984.

[65] S. R. Ibrahim. *Computation of Normal Modes from Identified Complex Modes*. AIAA Journal, 21(3):446–451, mar 1983.

[66] E. Foltête, G.M.L. Gladwell, and G. Lallement. *on the Reconstruction of a Damped Vibrating System From Two Complex Spectra, Part 2: Experiment*. Journal of Sound and Vibration, 240(2):219–240, feb 2001.

[67] Otakar Danek. *Inversion formulas for non-conservative systems (in Czech)*. Strojnicky Casopis, 30(6):650–657, 1979.

[68] S. Adhikari and J. Woodhouse. *Identification of Damping: Part 4, Error Analysis*. Journal of Sound and Vibration, 251(3):491–504, mar 2002.

[69] S. Adhikari and J. Woodhouse. *Identification of Damping: Part 3, Symmetry-Preserving Methods*. Journal of Sound and Vibration, 251(3):477–490, mar 2002.

[70] A. Srikantha Phani and J. Woodhouse. *Experimental identification of viscous damping in linear vibration*. Journal of Sound and Vibration, 319(3-5):832–849, jan 2009.

[71] Bram Vervisch, Kurt Stockman, and Mia Loccufier. *Torsional Damping Identification in Rotating Machinery*. In IMAC XXXII conference, 2014.

[72] Kjell Ahlin, Martin Magnevall, and Andreas Josefsson. *Simulation of forced response in linear and nonlinear mechanical systems using digital filters*. Proceedings of ISMA 2006, (1):3817–3832, 2006.

[73] V. Arora. *Structural damping identification method using normal FRFs*. International Journal of Solids and Structures, 51(1):133–143, jan 2014.

[74] Anna Reggio, Maurizio De Angelis, and Raimondo Betti. *A state-space methodology to identify modal and physical parameters of non-viscously damped systems*. Mechanical Systems and Signal Processing, pages 1–16, aug 2013.

[75] Giancarlo Genta and Nicola Amati. *Hysteretic damping in rotordynamics: An equivalent formulation*. Journal of Sound and Vibration, 329(22):4772–4784, oct 2010.